Study of Nano-structures with Applications on Single-mode Lasers

STUDY OF NANO-STRUCTURES WITH APPLICATIONS ON SINGLE-MODE LASERS

By

Lanxin Deng, B.Sc., M.Sc.

A Thesis

Submitted to the School of Graduate Studies

in Partial Fulfilment of the Requirements

for the Degree

Doctor of Philosophy

McMaster University

DOCTOR OF PHILOSOPHY (2012) McMaster University

(Electrical and Computer Engineering) Hamilton, Ontario

TITLE:	Study of Nano-structures with Applications on Single-mode Lasers
AUTHOR:	Lanxin Deng
	B.Sc., M.Sc. (University of Science and Technology of China)
SUPERVISOR:	Dr. Wei-Ping Huang
	Professor, Department of Electrical and Computer Engineering
NUMBER OF PAGES:	xiii, 154

Abstract

Semiconductor laser diode has been a popular research topic for longer than half a century and plays a crucial role in optical communication systems. The work in this thesis focuses on the development of the semiconductor laser diode with rapid-evolving nanotechnologies: by incorporating specific semiconductor or metal structures in the nanometer scale into the laser cavity, several key advantages are achieved.

One category of the nano-materials is semiconductor quantum dots (QD). QD laser is a promising product by providing three-dimensional confinement to the injected electrons and holes. However, in order to realize the single-longitudinal-mode operation, which is critical to optical communications in purpose of reducing the dispersion and partition noise, the Fabry-Perot (FP) QD laser still needs further development to suppress the gain-broadening effects; otherwise the mode-selective structure must be adopted, such as the distributed feedback (DFB) cavity. In this thesis, the QD FP laser and QD DFB laser are both researched by advanced modelling techniques and the work is summarized as follows.

1) For the QD FP laser, a comprehensive rate-equation model has been applied for simulation, with the emphasis on describing the interplay of inhomogeneous and homogeneous gain-broadening effects. According to the laser-behaviour simulations, it is found that for each given inhomogeneous broadening, the optimum homogeneous broadening can be obtained for the single longitudinal-mode selectivity. Based on the optimal gain-broadening parameters, the single-mode QD FP laser is designed and

analysed. The quantitative conditions for the performance feasibility are examined with respect to the gain-broadening parameters.

2) A one-dimensional (1D) standing wave model is developed for the QD DFB laser. This model can provide more information for the laser operation and better describe the dynamic behaviour compared with the rate-equation model. Based on it, the statistic operation and output spectrum of a typical QD DFB laser are simulated; and then the dynamic properties of the laser are analysed.

The other category is the metal nano-structure, including the metal nano-particle and the metal nano-strip Bragg grating. The related work is summarized as follows.

1) The optical properties of a single metal nano-particle with different size, composition and shape are researched by Mie theory, with respect to the localized surface plasmon polariton (LSPP) effect. It shows that both the resonance wavelength and Q-factor can be tuned in a large scale by proper methods.

2) A novel metal nano-strip distributed Bragg grating (DBR) laser is proposed and investigated theoretically. Firstly the metal nano-strip Bragg grating is simulated by the couple-mode theory and the mode-matching method. It shows that the coupling constant and reflection spectrum can be tuned to meet different requirements when varying the grating parameters. Then for the designed metal-grating DBR laser, the rate-equation simulation results show that it works under the single-mode operation for a broad range of the design parameters.

Acknowledgements

First and foremost, I would like to express my sincere gratitude to my supervisor Dr. Wei-Ping Huang, for his knowledge, guidance, inspiration and enormous support, which are invaluable to the success of my research projects. It is really one of the luckiest things in my life to study under his supervision and expose to his great scope and precious experiences.

I would like to especially thank Dr. Xun Li for his continuous understanding and encouragement, and always being passionate to answer my questions and share his knowledge of many aspects from laser physics, modeling techniques to semiconductor fabrication.

I am also very grateful to Dr. Chang-Qing Xu and Dr. Shiva Kumar, who provide me with a wide knowledge reference of optoelectronic devices and optic communications.

Deep appreciation also goes to Dr. Seyed M. Sadeghi, who guides me with my first exploration to the area of nano-material physics; Dr. Yanping Xi, Dr. Jianwei Mu and Lin Han, for their valuable discussions and cooperation on various research projects; Qingyi Guo, Yu Li, and other friends, for their help during my study in McMaster.

I acknowledge the ECE administrative and technical support, Ms. Cheryl Gies, Ms. Alexa Huang, Ms. Helen Jachna, Mr. Terry Greenlay and Mr. Cosmin Coroiu.

Lastly, my special thanks go to my husband Shijian Xu for accompany with heart; my son Austin Xu for his angelic smile; my parent for their love and sacrifice. My family is the source power for everything I accomplished.

Contents

Abstract .... **iii**

Acknowledgements .... **v**

Contents .... **vi**

List of Figures .... **x**

List of Tables .... **xiii**

Chapter 1 Introduction **1**

1.1 Background of the research 1

1.1.1 Semiconductor laser diodes 2

1.1.2 Semiconductor quantum dots 2

1.1.3 Metal nano-particles and structures 3

1.2 Motivation of the research 4

1.3 Numerical methods used in the research 4

1.4 Outline of the thesis 5

Chapter 2 Semiconductor Nano-structure: Quantum-dot (QD) Fabry-Perot (FP) Laser **8**

2.1 Introduction 8

2.2 The rate-equation model for QD FP laser 11

2.2.1 The homogeneous and inhomogeneous broadening 12

2.2.2 The gain model 14

2.2.3 Rate Equations 16

2.2.4 Parameters 18

2.3 Optimization of the two broadenings 20

2.3.1 Effect of homogeneous broadening 20

2.3.2 Effect of inhomogeneous broadening 22

2.3.3 Dependence of the gain spectra on the two broadenings 24

2.3.4 Optimum values 26
2.4 Single-mode laser design 27
2.4.1 Turn-on effects 28
2.4.2 Gain spectrum and output power spectrum 30
2.4.3 Modulation response 32
2.5 SMSR when varying the broadening parameters 35
2.6 Summary 37
Chapter 3 Semiconductor Nano-structure: Quantum-dot Distributed Feedback (DFB) laser 39
3.1 Introduction 39
3.2 Time-domain standing wave model for the QD DFB laser 42
3.2.1 The gain grating 42
3.2.2 Coupled-wave equations 44
3.2.3 Cavity modes 46
3.2.4 The standing wave model 48
3.2.5 Carrier rate-equations 49
3.2.6 Iteration process for obtaining the coupling constant 52
3.2.7 Summary of the algorithm implementation 54
3.3 Simulation results 55
3.3.1 Parameters 55
3.3.2 Cavity modes 57
3.3.3 The laser operation 59
3.4 Summary 67
Chapter 4 Metal Nano-particle: Mie Theory Calculation for Optical Properties of a Single Particle 69
4.1 Introduction 69
4.2 Mie theory for the metal nano-particle 71
4.2.1 The classical Mie theory 71

4.2.2 Efficiency factors and cross sections for extinction, scattering and absorption....74
4.2.3 Small-particle limit ($a << \lambda$) and the dipole approximation....76
4.2.4 Ellipsoidal particle or nano-rod....77
4.2.5 Dielectric function of the metal particle....78
4.3 Optical properties of the metal nano-sphere....80
4.3.1 Localized surface plasmon resonance: the multi-poles....80
4.3.2 Size effects....83
4.4 Move to longer wavelength....87
4.4.1 Change the surrounding material....89
4.4.2 Tungsten nano-spheres....90
4.4.3 Change the shape to the ellipsoid or nano-rod....91
4.5 Artificial imaginary part for a narrow resonance peak....92
4.6 Summary....94
Chapter 5 Metal Nano-structure: Distributed Bragg Reflector (DBR) Laser Design with Metal Nano-strip Grating....95
5.1 Introduction....95
5.2 DBR section based on the metal nano-strip grating....97
5.2.1 Coupled-wave theory (CWT)....97
5.2.2 Mode matching method (MMM)....101
5.2.3 Comparison of the results from the two methods....102
5.2.4 Design of the DBR region....104
5.3 Design of the DBR laser....109
5.3.1 Multi-mode rate equation model....111
5.3.2 Simulation results....113
5.4 Summary....116
Chapter 6 Conclusions and Future Topics....119
6.1 Summary of Contributions....119
6.2 Suggestions for Future Research Topics....120

Appendix A High-order Finite-Difference mode solver 122
Appendix B Deduction of the coupled-wave theory...126
Appendix C Deduction of the mode matching method...130
Bibiography 134

List of Figures

Figure 2-1. Schematic structure of the QD FP laser 12

Figure 2-2. Spectra of (a) the modal gain and (b) the output power when varying the FWHM of homogeneous broadening from 0.1meV to 10meV; the FWHM of inhomogeneous broadening is fixed as 20meV; the driving current is 10mA. 21

Figure 2-3. Spectra of (a) the modal gain and (b) the output power when varying the FWHM of inhomogeneous broadening width from 5meV to 20meV; the FWHM of homogeneous broadening is fixed as 10meV; the driving current is 10mA. 23

Figure 2-4. Dependence of the 90% bandwidth of the gain spectra on the homogeneous broadening and inhomogeneous broadening, (a) I = 10mA; (b) I = 40mA 25

Figure 2-5. Turn-on effects: ground state carrier number in different dot groups vs. time (a); and modal/total output power vs. time (b); I=10mA 29

Figure 2-6. (a) Gain spectrum; and (b) ground state carrier distribution; I=10mA 30

Figure 2-7. Output power spectrum; (a)I=10mA; (b)I=5mA.. 32

Figure 2-8. Small signal modulation response of QD laser 33

Figure 2-9. Large signal modulation response of QD laser 34

Figure 2-10. SMSR vs. driving current with different settings of inhomogeneous and homogeneous broadening.. 36

Figure 3-1. Schematic structure of the QD DFB laser.. 41

Figure 3-2. Illustration of the gain grating along *z*-direction 44

Figure 3-3. Iteration process for the threshold gain 53

Figure 3-4. Spectrum for cavity modes of the quantum-dot DFB laser............................ 57

Figure 3-5. Intensity distribution of the cavity modes along the cavity 59

Figure 3-6. Comparison of the results using 5 modes, 3 modes and 1 mode: L-I curve of the quantum-dot DFB laser; the inset enlarges the curve around the threshold current....60
Figure 3-7. Laser output power spectrum (a); enlargement around the peak (b); I=10mA....62
Figure 3-8. Carrier density distribution for the main mode along the cavity; I=10mA....63
Figure 3-9. Photon density distribution for the main mode along the cavity; I=10mA....63
Figure 3-10. The gain distribution and the coupling coefficient for the main mode along the cavity; I=10mA....64
Figure 3-11. Small signal modulation response of the QD DFB laser....65
Figure 3-12. Output power vs. time with square wave modulation; current from 0.6mA to 0.7mA; (a) f=0.2GHz; (b) f=1GHz....66
Figure 4-1. Extinction efficiency spectra of silver nano-sphere with different radius in the air; the multi-poles arise in order....81
Figure 4-2. Extinction efficiency spectra of (a) silver; (b) gold; (c) copper nano-sphere with different radius in the air....84
Figure 4-3. Extinction efficiency spectra of silver nano-sphere with different radius in the aluminia ($\varepsilon = 3.2$)....89
Figure 4-4. Extinction efficiency spectra of Tungsten nano-sphere with different radius in the air....90
Figure 4-5. Normalized absorption spectra of silver prolate spheroid in the air; a is the long axis, b and c are the two short axis....91
Figure 4-6. The extinction, absorption and scattering spectra of a silver nano-sphere in the air; the imaginary part of the metal's dielectric function is multiplied by a factor of (a) 1; (b) 0.5; (c) 0.25; (d) 0.1; (e) 0.01....93
Figure 5-1. Schematic structure of the DBR laser....95
Figure 5-2. Sectional view of the DBR region....97
Figure 5-3. Field pattern of the main mode, red line: with metal;....98
Figure 5-4. Perturbation of the dielectric constant along *z*-direction....99

Figure 5-5. Comparison of the power reflectivity spectrum calculated by coupled-wave theory (CWT) and mode-matching method (MMM); D=0.6µm; L=200µm 103
Figure 5-6. Comparison of the peak reflectivity calculated by coupled-wave theory (CWT) and mode-matching method (MMM); D=0.6µm 104
Figure 5-7. Coupling constant when varying the spacing of the grating and core region 106
Figure 5-8. Dependence of peak reflectivity on grating length and spacing 106
Figure 5-9. Dependence of FWHM of reflection spectrum on grating length and spacing 107
Figure 5-10. Power reflection spectrum when varying the duty cycle 108
Figure 5-11. Dependence of the peak reflectivity and FWHM on the duty cycle 109
Figure 5-12. Output power and SMSR of the DBR laser when $D=0.6\mu m$ and the grating length is $150\mu m$ 114
Figure 5-13. Output power of the DBR laser when varying the spacing and the grating length; I=40mA 115
Figure 5-14. SMSR of the DBR laser when varying the spacing and the grating length; I=40mA 115
Figure A-1. Three sampled points and the interfaces [126] 123

List of Tables

Table 2-1. QD laser parameters[53] 19
Table 2-2. Estimated best values for FWHM of homogeneous broadening 27
Table 3-1. QD DFB laser parameters [53] 56
Table 5-1. Modal index and coupling constant when varying the spacing between the grating and the core region 105
Table 5-2. The effective penetration length of the grating 110
Table 5-3. DBR laser parameters [130] 113

Chapter 1
Introduction

In this chapter, firstly I discuss the background and motivation of the research topic in this thesis. Then I give an outline for the thesis.

1.1 Background of the research

The semiconductor diode laser (SLD) has become one of the key components in the optical communication systems since its invention dating back to the year 1962 [1]. Due to its rapid development in the latest dozens of years, the fabrication techniques and design structures of SLD both become much more mature nowadays compare to those of the early age. As one of the results, the quantum-well structure for the gain medium becomes dominant among the products on the market.

The next developments of the SLD are quite possibly on the material side due to the recent advances on nano-scale material fabrication techniques, such as the various lithography methods (electron-beam lithography, imprinting lithography, scanning probe lithography, etc.) and the wet-etching technique with precision in the nanometer scale. These techniques create new possibility to introduce novel nano-materials into the semiconductor laser cavity and further improve the performance or reduce the cost of such device.

In the following sub-sections, the SLD and the novel nano-materials including the semiconductor quantum dot and metal nano-particles and structures are briefly introduced.

1.1.1 Semiconductor laser diodes

The semiconductor laser diodes have several considerable advantages, for instance, the compact size, fast modulation response, the integration compatibility and relatively high conversion efficiency. Because of these features, it is hard to be replaced by other candidates such as the optical fiber laser or the solid state laser.

For the edge-emitting SLD, based on the cavity structure, it can be classified into the Fabry-Perot (FP) laser, the distributed feedback (DFB) laser and the distributed Bragg reflector (DBR) laser.

Each of these three laser structures has its advantages and disadvantages. The FP laser has the simplest structure thus the fabrication cost is generally lowest, but the characteristic multiple-longitudinal-mode operation restricts its applications. The DFB laser with more complexity of the structure can guarantee the single-mode operation; however, the yield is low and then the cost rises. The DBR laser also has a relatively higher cost, especially due to the re-growth fabrication process; on the other hand, it is convenient for the modulation control.

1.1.2 Semiconductor quantum dots

Semiconductor quantum dots (SQD) assemble [2] is a new-emerging material which is a promising candidate to replace the conventional quantum-well gain medium in the laser cavity. By shrinking the size of the gain medium to several nanometers, the injection electrons and holes have more confinement and the recombination efficiency is enhanced. And because of the atom-like gain spectrum of the quantum dot, the differential gain also becomes higher. Besides, the temperature stability of the quantum dot laser is improved comparing to the quantum-well laser [3].

The semiconductor quantum dot laser is still under fast-developing in all aspects from the fabrication to the theoretical research and the design innovation.

1.1.3 Metal nano-particles and structures

Metal nano-particles and structures are important components in the nano-optics, mainly attribute to the interesting characteristic so-called surface plasmon polariton (SPP) effect [4], which describes the interaction of the electrons in metal and the light wave.

For metal nano-particles, the localized SPP effect can highly enhance the near field and produce a strong resonance. Both of these two features can find applications in optical devices; for instance, the enhanced near field can be used to provide assistance for pumping the quantum dot; and the strong resonance can be applied as a wavelength-selective scheme.

And further, the nano-scale metal structures with various design and functions are also widely researched in recent years [5]. The examples include the two-dimensional array formed by the metal particles [6-8] or the metal holes [9-12]; the metal grating [13-15] used as the external reflection for laser [16]; the slit metal grating [17-20] and a hybrid metal grating [21]; the metal slit waveguide [22-25] and so on.

1.2 Motivation of the research

While the long-haul and metropolitan-area communication networks have been dominated by the optical communication systems built with the optical fiber and other optical components including the semiconductor laser diode as the light source, nowadays the all-optical access network which is connected to the end users is also under fast developing and implementation. However, an independent optical transceiver will be required for each user in the access network, and this leads to new demand on the very low-cost semiconductor laser diodes with the single-mode operation [26].

From this consideration, the FP laser with better performance, especially the single longitudinal-mode output, will be a competitive candidate. To modify the conventional FP laser, the new materials are researched in my work, including the quantum-dot material and the metal nano-particles. Firstly the QD FP laser is simulated and researched with the emphasis on the output spectrum width and conditions of the single-mode operation. The next, potential applications of the metal nano-particles are also discussed with the research on the SPP resonance.

On the other hand, the DFB and DBR laser can guarantee the single-mode operation and the performance can also be improved based on the new materials. To aim at that, the numerical model for the QD DFB laser is developed in this thesis; moreover, a novel metal-grating DBR laser is proposed.

1.3 Numerical methods used in the research

Various numerical methods are applied as simulation tools in this work. For the optical waveguide, the finite difference method with high-order formulas is used to carry out the optical modal analysis in the transverse direction; the propagation and reflection in longitudinal direction is described by the coupled-mode theory and the mode-matching method.

For the laser behaviour, the rate equations are derived and applied to the QD FP laser; and the QD DFB laser is simulated using a one-dimensional standing wave model which is based on the coupled-wave equations, while the carrier behaviour is described by the one-dimensional rate equations.

1.4 Outline of the thesis

This thesis is started with the introduction as Chapter 1, after that the major part contains four chapters presenting the research work in four subjects, respectively, and followed by the last chapter with the conclusion and discussion for the future work.

Chapter 2 is on the QD FP laser simulation and design, with emphasis on the interplay of the inhomogeneous and homogeneous gain-broadening of the quantum-dot assemble and the effects on the gain and output spectrum. Details of the rate-equation model are given in this chapter. Using this model, a typical self-assembled InGaAs/GaAs quantum dot laser is studied as an example. For this laser, the influence of the two broadenings on the gain spectrum is discussed; based on that, the optimized values of the broadenings are obtained. In the next place, further investigation on the conditions of single-mode operation is carried on. It is predicted that with suitable control of the two broadenings, the single-mode QD FP laser can be realized.

Chapter 3 is on the QD DFB laser modelling and simulation, for which the one-dimensional standing wave model is derived for the typical gain-grating QD DFB laser. In the first section, the details of this model are described, from the gain grating, the governing coupled-wave equations, expansion of cavity modes, carrier rate-equations of the QDs to the algorithm implementation. Then in the second section, a typical QD DFB laser with InGaAs/GaAs material is simulated using this model and the results are presented and analyzed.

Chapter 4 is on the optical properties of a single metal nano-particle which shows the localized SPP effect. Firstly the Mie theory as the calculation method is reviewed, and then the absorption and scattering of the noble metal nano-particles are researched and the plasmon resonance is investigated. For potential application in optical devices, several methods are discussed to move the resonance peak to longer wavelengths which are used in optical communication systems. In the last part, the mechanism that the resonance peak can be narrowed by reducing the absorption is testified.

Chapter 5 is on the design of a novel metal-grating DBR laser. In the first part the grating based on the metal nano-strips is theoretically simulated using numerical methods, by which the influence of several critical design parameters on the reflection spectrum is investigated. Then in second part the DBR laser with the designed metal grating is simulated by the rate-equation model, and the output power and SMSR under different parameters of the metal grating are studied.

Finally the research work is summarized in the last chapter, and the suggestions for the future work are listed.

Chapter 2

Semiconductor Nano-structure: Quantum-dot (QD) Fabry-Perot (FP) Laser

2.1 Introduction

The semiconductor laser development has been a popular topic for longer than half a century. Numerous designs have been researched; most of them were just dying out, only a few remain as successful products. Among them an obvious trend is to provide more stringent carrier confinement through various designs. We can see this from homo-junction to hetero-junction and from bulk active region to quantum-well active region. For the same reason the semiconductor quantum-dot laser is highly expected [27-35], in which the carriers are spatially restricted to the smallest possible dimension.

Increasing the carrier confinement to all three directions can provide several key advantages to the laser: high material and differential gain which leads to lower threshold current [36]; better temperature stability [37]; and narrower gain spectrum [2]. As for quantum dot lasers, the first two advantages have been experimentally verified with comparison to quantum well lasers [3, 38-41].

For one single quantum dot, if the size is small enough (i.e. comparable to de Broglie wavelength in all three directions), the energy levels are discrete. And the intra-band energy levels are further separated when the size becomes even smaller. The energy difference between the ground state and the excited state can then be larger than several times of the thermal energy, thus all of the carriers remain in the ground state if not saturated and the gain spectrum is a delta function. In this case the quantum dot shows similar energy band structure to a single atom. Experiments showing ultra-narrow luminescence lines from a single quantum dot have proved this fact [42-43].

However, for real quantum-dot assembles, the gain spectrum is not a delta function but a much wider peak. The reasons are manifold; such spectrum broadening effects can be classified into two categories: homogeneous broadening and inhomogeneous broadening.

Homogeneous broadening is intrinsic to each quantum dot, results in a Lorenzian shape in the photoluminescence spectrum. Generally, two quantum effects cause this broadening. One is the relaxation or carrier decaying process, characterized by the carrier lifetime (T_1); the other is the dephasing process, similarly described by the dephasing time (T_2). The spectrum linewidth is inversely proportional to the lifetime and the dephasing time. At the ground state in quantum dots at room temperature, the carrier lifetime broadening, the carrier-phonon scattering and the carrier-carrier interactions are all considered to contribute to the homogeneous broadening [44-46].

Inhomogeneous broadening is extrinsic, caused by the non-uniformity of size, shape and composition from dot to dot in the quantum dot assembles. This non-uniformity is apparently dependents on the fabrication methods. Till now the self-assembling Stranski-Krastanov (SK) growth technique is most successful, by which the defects of each dot can be well controlled compared with the earlier top-to-bottom fabrication methods, but the size distribution is still in a relatively wide range. Some efforts are made on improving the uniformity of dots [47-48] and hopefully the quality will be further elevated.

Because of these broadening effects, the gain spectrum of quantum dot assembles currently reported is not narrow enough to select a single lasing mode. This restricts the application of Fabry-Perot quantum-dot laser because the single longitudinal-mode operation is one of the key requirements for reducing the dispersion and partition noise in high-speed optical communications applications.

In order to select a single mode, additional structural mode-selective schemes are used, for instance, the gain grating by periodically etching away some of the QDs in so-called QD distributed feedback (DFB) lasers [49]; or laterally loss-coupled QD DFB lasers using the absorptive metal grating[50-51]; or QD Fabry-Perot lasers together with the external-cavity feedback which is wavelength-selective [52]. Such designs notably increased the complexity.

The purpose of this work is to study the interplay of the homogeneous and inhomogeneous broadenings and quantitatively discuss the relationship between the spectral widths and broadening parameters, and then investigate on the condition of single-mode operation for QD lasers without any additional mode-selective scheme. The work is based on a comprehensive rate-equation model which is extracted to represent the two broadening effects and to provide theoretical prediction of the output power spectra.

This chapter is organized into four parts. In section 2.2 the rate-equation model for the typical self-assembled InGaAs/GaAs quantum-dot Fabry-Perot laser is introduced. This model is a following of Sugawara's model [53-55] and describes the interplay of the homogeneous and inhomogeneous broadening of the quantum dots. Then in section 2.3 we show the simulation results in the aspect of the effects of the two broadenings on the laser gain spectrum. The laser output power and gain spectrum are changed with different setting of the homogenous and inhomogeneous broadening, and the relationship between them is clearly explained. Some of the result is also compared with Sugawara's numerical and experimental results as the validation of the calculation. Based on the analysis, the values of the broadenings are optimized. In section 2.4 the single-mode Fabry-Perot QD laser is designed using the optimum values. The SMSR (side mode suppression ratio) and modulation response are presented. Then in section 2.5 the design requirements to achieve the single-mode operation are discussed. The conclusions are summarized in the section 2.6.

2.2 The rate-equation model for QD FP laser

The rate-equation model is used to simulate a typical self-assembled InGaAs/GaAs quantum dot laser [29]. The schematic structure of this quantum-dot Fabry-Perot laser is shown in Figure 2-1. It is made with a ridge waveguide structure and the active region consists of several self-assembled InGaAs quantum dot layers, which are separated and sandwiched by thin GaAs layers. The heterostucture is formed together with AlGaAs cladding layers. The substrate and the upper cladding is made of GaAs. Details about this laser can be found in [29]. Although designed for this specified laser, the rate-equation model is generalized and can be used for other quantum dot lasers with slight modifications.

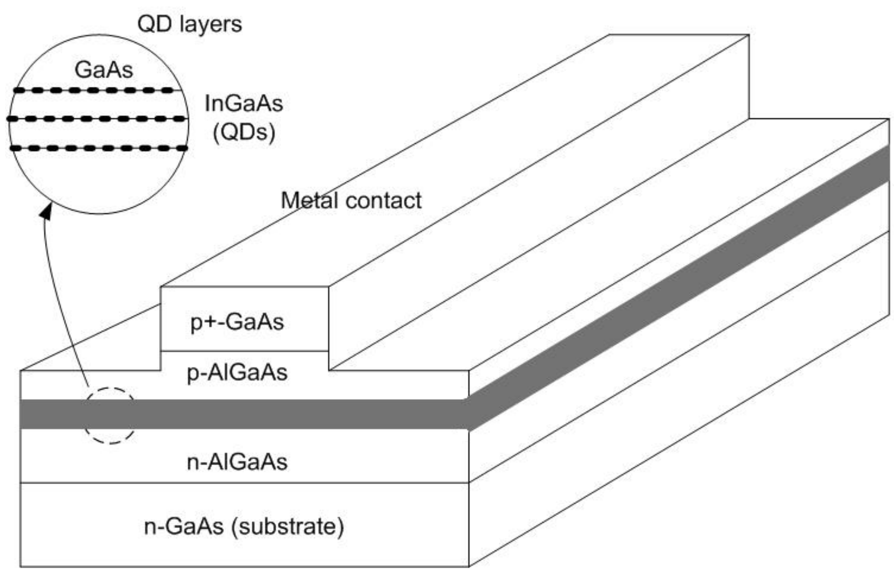

Figure 2-1. Schematic structure of the QD FP laser

2.2.1 The homogeneous and inhomogeneous broadening

The numerous quantum dots in the active region can have different transition energies as the reason for the inhomogeneous broadening. The probability density of dots per unit energy with regard to the transition energy takes Gaussian distribution, whose center locates at E_0 as the average transition energy and the distribution variance is ξ_0. With discretization on energy scale, all of the quantum dots are categorized into multiple groups with different transition energies E_n and n denotes the group number. The normalized probability density of dots in group n is,

$$G\left(E_n - E_0\right) = \frac{1}{\sqrt{2\pi}\xi_0} \exp\left(-\frac{\left(E_n - E_0\right)^2}{2\xi_0^2}\right) \tag{2.1}$$

For each of the quantum dots, the homogeneous broadening is described by a Lorentz expression with its FWHM (full width at half maximum) represented by Γ_{ho}, which is assumed to be the same for all of the dots. For a quantum dot with the transition energy E_n, the probability density of the dot per unit energy with its emission contribution to energy E is then described by,

$$L\left(E - E_n\right) = \frac{1}{2\pi} \frac{\Gamma_{ho}}{\left(E - E_n\right)^2 + \Gamma_{ho}^2 / 4} \tag{2.2}$$

To conveniently describe the interaction between photons and carrier groups, in this model the transition energies for all of the carrier groups are assumed to coincide with the photon energies of longitudinal modes [53]. This is an appropriate discretization on energy scale because that the energy interval between laser longitudinal modes is generally much smaller than the FWHM of inhomogeneous broadening. Then the energy interval in unit of eV is,

$$\Delta E = hc / \left(2en_r L_A\right) \tag{2.3}$$

where h indicates the Planck's constant, c the speed of light in vacuum, e the elementary charge, L_A the laser cavity length, n_r the group index in the laser cavity.

With the average transition energy E_0 and the energy interval ΔE, the spectrum is discretized for both carriers and photons. We assume that there are total *(2M+1)* sampling points within the energy range involved, which means the quantum dots are divided into *(2M+1)* groups and the same number of longitudinal modes is considered. For the *n*-th group, the transition energy (or photon energy) is therefore,

$$E_n = E_0 + (n - M)\Delta E, \quad n = 0,1,2,...,2M \tag{2.4}$$

With this grid the proportion of the dots in the *n*-th group is,

$$G(n) = \Delta E \cdot G(E_n - E_0) \tag{2.5}$$

Similarly, the probability of the *n*-th group dots with their contribution to energy E_m is,

$$L(m,n) = \Delta E \cdot L(E_m - E_n), \quad m,n = 0,1,2,...,2M \tag{2.6}$$

In simulation *M* should be large enough to make sure that the summation of $G(n)$ over the *(2M+1)* groups is close to 1.

2.2.2 The gain model

From the density matrix calculation, the linear optical gain provided by the *n*-th group of quantum dots to the *m*-th lasing mode is then expressed by [35, 53],

$$g_{mn}^{(1)} = \frac{e^2 h N_D}{c n_r \varepsilon_0 m_0^2} \frac{\left|P_{cv}^{\sigma}\right|^2}{E_n} \left[f_c(n) - f_v(n) \right] G(n) L(m,n) \tag{2.7}$$

where m_0 represents the electron mass, ε_0 the vacuum permittivity, N_D the volume density of quantum dots, f_c and f_v the distribution function of the conduction band and the valence band for the ground state, respectively. The superscript *(1)* denotes that this term is derived from the first-order $k \cdot p$ perturbation theory. From this theory, the transition matrix element P_{cv}^{σ} is then given as [35, 53],

$$\left|P_{cv}^{\sigma}\right|^2 = M^2 \left|I_{cv}\right|^2 = \frac{m_0^2}{12m_e} \frac{E_g\left(E_g + \Delta\right)}{E_g + 2\Delta/3} \left|I_{cv}\right|^2 \tag{2.8}$$

where m_e represents the electron effective mass, E_g the band gap energy, Δ the spin-orbit interaction energy, and I_{cv} the overlap integral between the envelope functions of the electron and the hole. P_{cv}^{σ} can be regarded as the same for all of the quantum dots.

If $P(n)$ is the occupation probability in ground state for the *n*-th group dots, which is assumed to be the same for electrons and holes, in Sugawara's model, it is assumed to be equal to $f_c(n)$. Further assume the two carriers mirror each other, we have,

$$f_c(n) - f_v(n) = P(n) - \left[1 - P(n)\right] = 2P(n) - 1 \tag{2.9}$$

$P(n)$ is directly got from the carrier number in each group. If $N_g(n)$ represents the carrier number in the *n*-th group dots and V_A the active region volume, the relationship between $P(n)$ and $N_g(n)$ is therefore given as,

$$P(n) = \frac{N_g(n)}{2N_D V_A G(n)} \tag{2.10}$$

In this equation, since $N_g(n)$ has both electrons and holes counted, but electrons and holes contribute to $P(n)$ in pairs, 2 must be divided.

2.2.3 Rate Equations

When discussing the lasing process of the quantum dots, the energy bands involved includes the wetting layer, the excited state and the ground state. From the experiment, only the ground state is lasing under room temperature. And since our main purpose is to discuss the bandwidth of the output power spectra, the carrier transport is simplified in this model. Firstly, we assume all of the carriers are injected into the wetting layer. Secondly, the excited state is not included in the equations while the carrier relaxation and escape are equivalently considered between the wetting layer and the ground state. Thirdly, the thermal escape from the ground state is ignored. Fourthly, the dynamics of electrons and holes simply mirror each other, thus we do not need to separate carrier equations for the two categories of carriers.

Given all that, carrier equations are extracted for the wetting layer and the ground state, respectively, with τ_d as the carrier relaxation time from the wetting layer to the ground state, τ_{wr} as the carrier recombination lifetime in the wetting layer, and τ_r as the carrier recombination lifetime in the ground state.

We use N_w to represent the carrier number in the wetting layer, N_g as the carrier number in the ground state, S as the photon number. For carrier equations in the ground state we have *(2M+1)* equations, each for one group of dots. The same number of photon equations is introduced. In photon equations, β indicates the spontaneous emission coefficient, Γ the optical confinement factor, and τ_p the photon lifetime.

Therefore, the rate equations are given as,

$$\begin{aligned}
\frac{dN_w}{dt} &= \frac{I}{e} - \frac{N_w}{\tau_{wr}} - \frac{N_w}{\overline{\tau}_d} \\
\frac{dN_g(n)}{dt} &= \frac{N_w G(n)}{\tau_d(n)} - \frac{N_g(n)}{\tau_r} - \frac{c\Gamma}{n_r}\sum_m \left[g_{mn}^{(1)} S(m) \right] \\
\frac{dS(m)}{dt} &= \frac{\beta N_g(m)}{\tau_r} + \frac{c\Gamma}{n_r}\left[\sum_n g_{mn}^{(1)} \right] S(m) - \frac{S(m)}{\tau_p}
\end{aligned} \tag{2.11}$$

The carrier relaxation from the wetting layer to the ground state follows the Gaussian distribution caused by the inhomogeneous broadening. And the relaxation time depends on the ground-state occupation probability of each dots group. If τ_{d0} represents the relaxation time for zero-occupation of the ground state, then the relaxation time for the *n*-th group is given as[25],

$$\tau_d^{-1}(n) = \tau_{d0}^{-1}\left[1 - P(n)\right] \tag{2.12}$$

And the relaxation time in the wetting layer carrier equation $\overline{\tau}_d$ takes average of all of the $\tau_d(n)$,

$$\overline{\tau}_d^{-1} = \sum_n \tau_d^{-1}(n) G(n) \tag{2.13}$$

The photon lifetime is then given as,

$$\tau_p^{-1} = \frac{c}{n_r}\left[\alpha_i + \frac{1}{2L_A}\ln\left(\frac{1}{R_1R_2}\right)\right] \tag{2.14}$$

And the output power from one end of the laser for the *m*-th mode is,

$$I(m) = \frac{ceE_m S(m)\ln(1/R)}{2n_r L_A} \tag{2.15}$$

where α_i indicates the internal loss of the laser cavity, R_1 and R_2 represent the power reflectivities of the cavity facets and R can be either of them. E_m is in unit of *eV* and *I* is in unit of *Watt*. The total output power is the summation of $I(m)$ over $m \in [0,\ 2M]$.

From the rate equations, the modal gain for the *m*-th mode is,

$$\Gamma g_m = \Gamma \sum_n g_{mn}^{(1)} = \frac{\Gamma e^2 h N_D}{c n_r \varepsilon_0 m_0^2} \sum_n \frac{\left|P_{cv}^{\sigma}\right|^2}{E_n}\left(2P(n)-1\right)G(n)L(m,n) \tag{2.16}$$

2.2.4 Parameters

The parameters used in the simulation [53] are listed in Table 2-1. Among them, the active region volume V_A refers to the volume of all of the very thin quantum-dot layers and the volume density of quantum dots N_D is defined as the ratio of the total number of dots to V_A. The carrier recombination lifetime of the ground state in quantum dots and that of the wetting layer are assumed to be the same.

Table 2-1. QD laser parameters[53]

Parameters	**Values**
cavity length L_A	900 μm
internal loss α_i	6 cm^{-1}
facet reflectivity R_1	0.3
facet reflectivity R_2	0.9
confinement factor Γ	0.06
effective index n_r	3.5
central lasing energy E_0	1 eV
band gap energy E_g	0.8 eV
spin-orbit interaction energy Δ	0.35 eV
electron effective mass m_e	$0.04 * m_0$
spontaneous emission coefficient β	10^{-4}
carrier lifetime in ground state τ_r	2.8 ns
carrier lifetime in wetting layer τ_{wr}	2.8 ns
relaxation lifetime τ_{d0}	10 ps
volume density of quantum dots N_D	6.3×10^{22} m^{-3}
active region volume V_A	2.2×10^{-16} m^{3}

To investigate the effect of homogeneous and inhomogeneous broadening on the laser gain and output power spectra, FWHMs of the two broadenings represented by Γ_{ho}

and Γ_{in} vary from 0.1 *meV* to 20 *meV*, and from 5 *meV* to 20 *meV*, respectively. The value will be specified with the simulation results.

2.3 Optimization of the two broadenings

Given that the cavity length L_A = 900μm and cavity effective refractive index n_r = 3.5, the modal energy interval ΔE is around 0.197meV. Choose M = 175, which means totally 351 longitudinal modes are simulated and they cover a wavelength range from around 1198nm to around 1284nm. This range is wide enough to cover the inhomogeneous broadening of the quantum dots thus to clearly shows their contribution to all of the optical modes.

2.3.1 Effect of homogeneous broadening

Firstly we fix the inhomogeneous broadening Γ_{in} = 20meV and vary the homogeneous broadening width Γ_{ho} from 0.1meV to 10meV. The driving current is set to be I = 10mA. Figure 2-2 show the spectra of the modal gain and the output power. Figure 2-2(b) is also consistent with the calculation and experimental results of Sugawara [53] as a validation of our simulation.

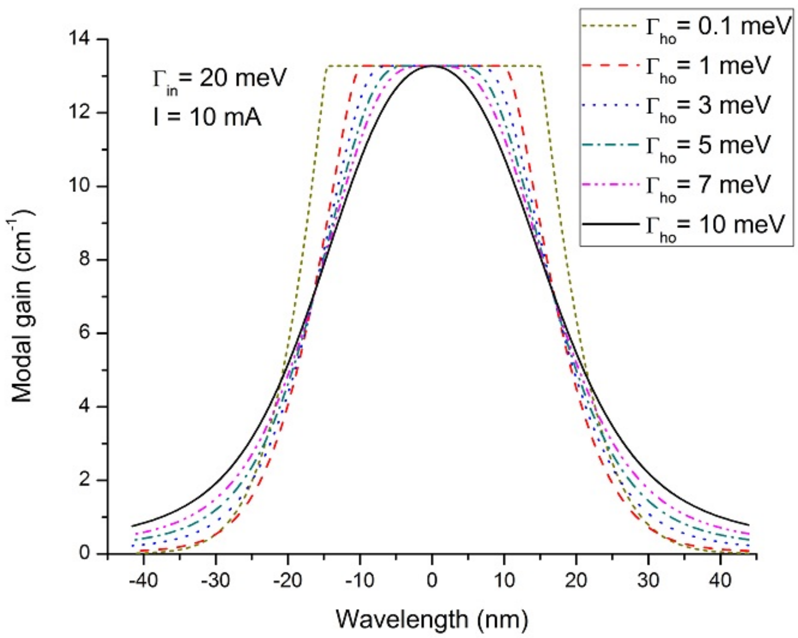

(a)

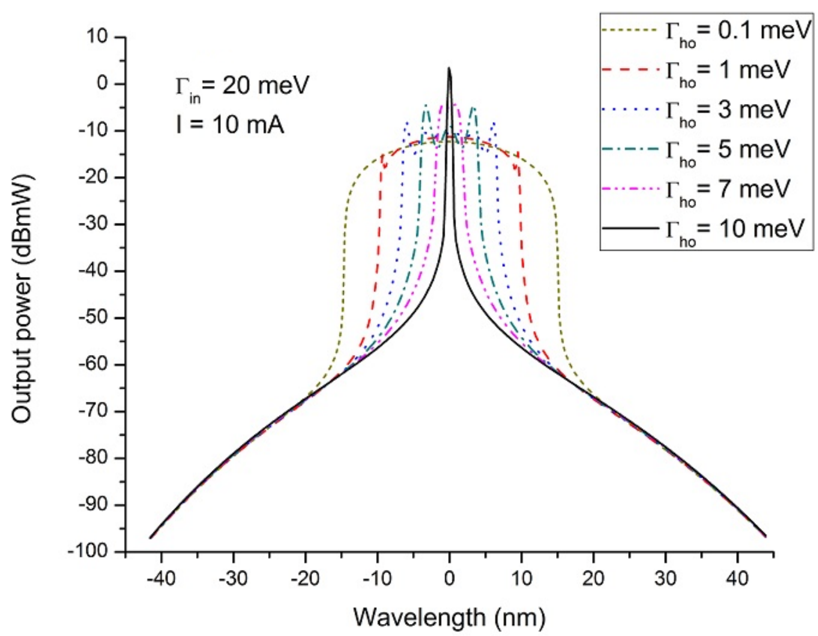

(b)

Figure 2-2. Spectra of (a) the modal gain and (b) the output power when varying the FWHM of homogeneous broadening from 0.1meV to 10meV; the FWHM of inhomogeneous broadening is fixed as 20meV; the driving current is 10mA.

The inhomogeneous broadening decides the spontaneous emission which always happens no matter if the lasing condition is reached or not. The arc-shaped bottom of curves in Figure 2-2(b) shows the spontaneous emission spectrum. We can see that it always remains the same when the inhomogeneous broadening is fixed.

The homogeneous broadening of each quantum dot gives the possibility for them to have collective lasing while they are spatially separated. As we can see from Figure 2-2, at the central wavelengths, when the collective modal gain reaches the value which equals to the cavity loss, the lasing happens and then the modal gain is clamped at that value.

And also from Figure 2-2, in this chosen range of homogeneous broadening, as Γ_{ho} increases, the collective lasing becomes stronger and the output power spectra narrows.

2.3.2 Effect of inhomogeneous broadening

Then we fix the homogeneous broadening Γ_{ho} = $10meV$ and vary the inhomogeneous broadening Γ_{in} from $5meV$ to $20meV$ while the driving current keeps $10mA$. Figure 2-2 shows the laser modal-gain spectrum and the output-power spectrum.

From Figure 2-3(b) we can see the spontaneous emission spectrum has wider peak when the inhomogeneous-broadening width is larger. And similarly, from Figure 2-3(a), the modal gain spectrum peak also becomes wider with the raise of inhomogeneous broadening. Accordingly, the number of lasing modes increases.

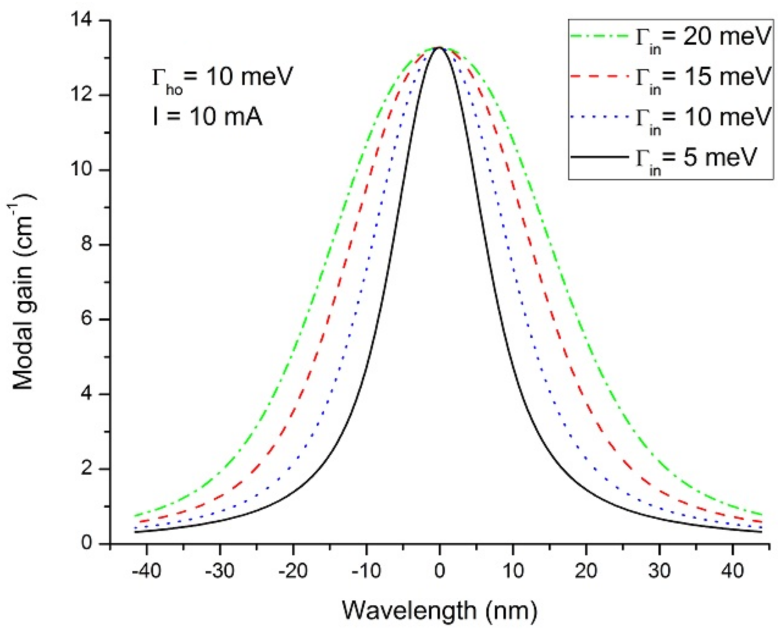

(a)

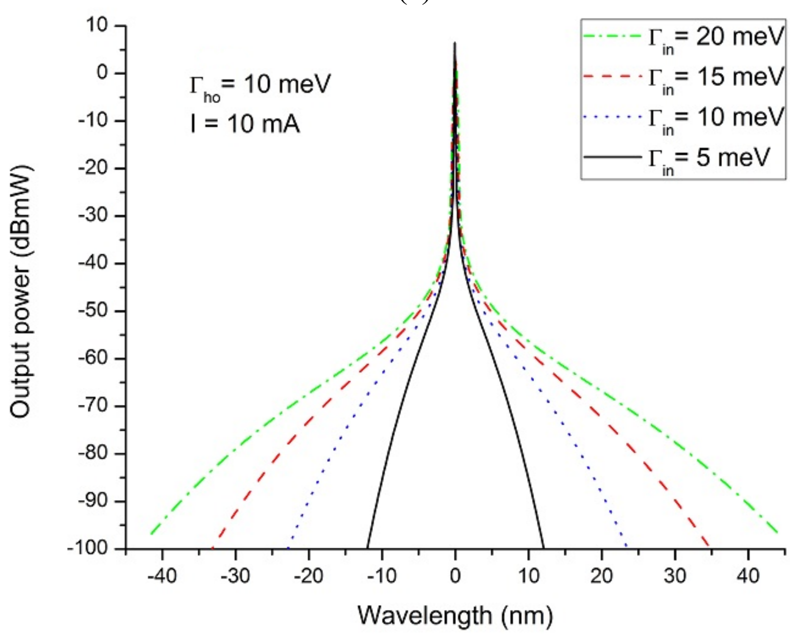

(b)

Figure 2-3. Spectra of (a) the modal gain and (b) the output power when varying the FWHM of inhomogeneous broadening width from 5meV to 20meV; the FWHM of homogeneous broadening is fixed as 10meV; the driving current is 10mA.

Therefore, to sum up the effects of the two broadening on the output and gain spectra, we conclude as follows: 1) the inhomogeneous broadening decides the spontaneous emission spectrum, 2) the homogeneous broadening narrows the modal gain spectrum by collective lasing; 3) the modal gain and output power spectra depend on both broadenings: the bandwidths of the gain and output power spectra are narrower if the inhomogeneous broadening is narrower, but in certain range, the bandwidth goes narrower if the homogeneous broadening is wider.

2.3.3 Dependence of the gain spectra on the two broadenings

We run simulation on different settings of the inhomogeneous and homogeneous broadening and get Figure 2-4, which shows the 90% bandwidth of the gain spectra. 90% bandwidth is defined as the bandwidth that at the band edge the gain drops to 90% of its value at central wavelength.

Figure 2-4(a) and 2-4(b) show the dependence of the 90% bandwidth of gain spectra on the homogeneous broadening and inhomogeneous broadening, in conditions that the driving current equals to 10mA and 40mA, respectively. As concluded above, the gain spectrum gets wider if the inhomogeneous broadening is larger; but when the homogeneous broadening is increased, the gain spectrum firstly gets narrower and then gets wider, as we can see that all of the curves show a V-shape. Besides, the curves are similar in the two figures that are under different driving currents, which means the gain shape does not change much when the current changes. This characteristic is a merit for laser design.

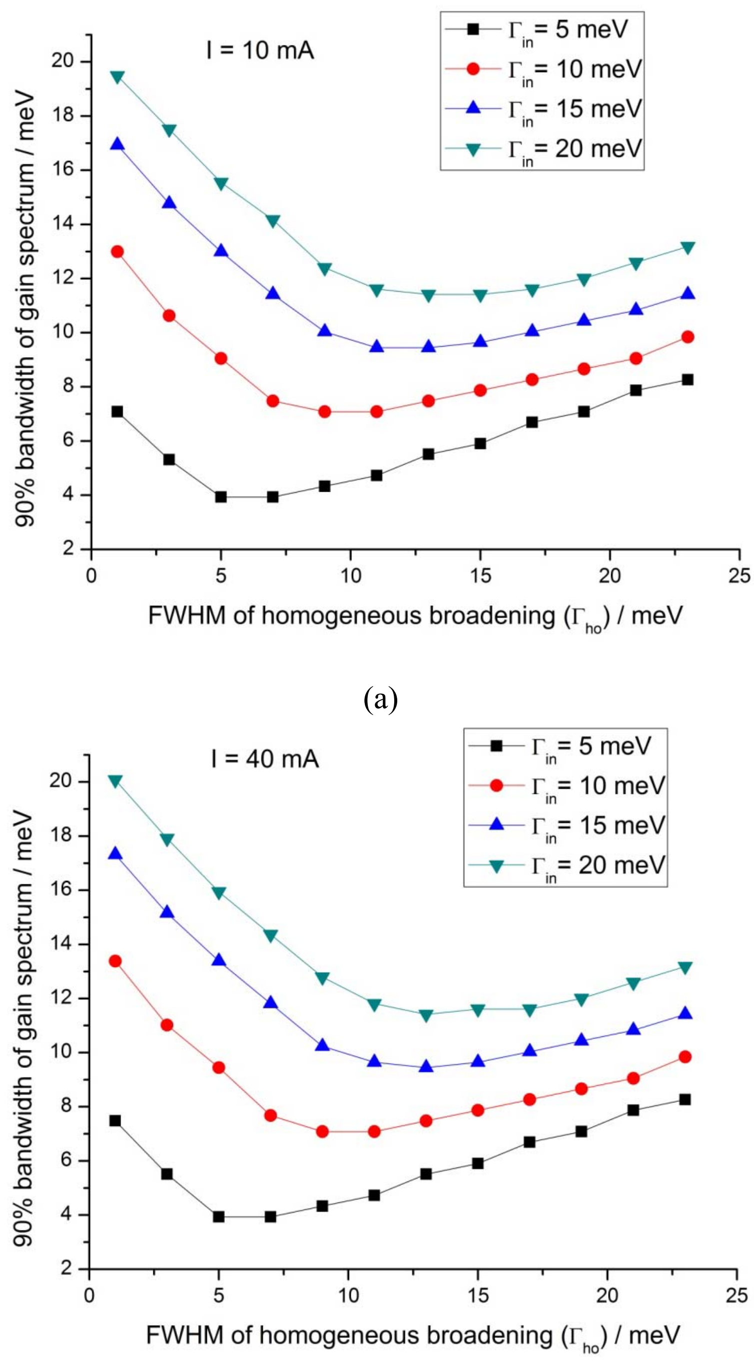

Figure 2-4. Dependence of the 90% bandwidth of the gain spectra on the homogeneous broadening and inhomogeneous broadening, (a) I = 10mA; (b) I = 40mA

The reason that the curves in Figure 2-4 show the V-shape is explained as follows. At first, the inhomogeneous broadening causes the quantum dots to have emission at different energies. Because they are spatially detached, spontaneous emission comes from each of them separately, thus the spontaneous emission spectrum follows exactly the same Gaussian distribution as the inhomogeneous broadening within the energy scope. Then after the photons are generated, they can travel from dot to dot as the seeds of the stimulated emission. And because of the homogeneous broadening, each of the quantum dots is not only allowed to have emission at its original transition energy, but also have possibility to have emission in the vicinity of that energy. With that possibilities and the travelling photons, the gain competition for stimulated emission can happen on all of the wavelengths, and then the collective lasing takes place on the central wavelengths of the energy band. In this way the homogeneous broadening causes a narrow gain peak, and when the homogeneous broadening increases, this collective effect is stronger and the gain peak gets narrower. When the homogeneous broadening is large enough, i.e. larger than the peak location of the V-shape, it also becomes another reason for the broadening of the gain spectrum. This is similar to the effect of inhomogeneous broadening and not difficult to understand.

2.3.4 Optimum values

Therefore, we can find the best value for FWHM of the homogeneous broadening, and this value is related to the chosen width of inhomogeneous broadening. From Figure 2-4, we can extract these best values, which are shown in Table 2-2.

Table 2-2. Estimated best values for FWHM of homogeneous broadening

FWHM of inhomogeneous broadening Γ_{in} (meV)	Estimated best value for FWHM of homogeneous broadening Γ_{ho} (meV)	
	I = 10mA	I = 40mA
5	6	6
7.5	8	8
10	10	10
12.5	12	11
15	12	13
17.5	13	14
20	14	13
22.5	13	14

From these best value combinations of the two broadenings, we can start to design for narrow-band, and even further, the single longitudinal-mode laser.

2.4 Single-mode laser design

Reducing the cavity length can increase the energy interval of longitudinal modes. So we set the cavity length as L_A = 200μm instead of 900μm (which we used in the first paper to provide a delicate scale in favour of finding the spectrum width), and the active region volume V_A is reduced with the same ratio. Now the energy interval ΔE = 0.887eV. In the simulation totally 81 modes are considered. Numerical experiments have been carried out to confirm that this energy/wavelength range is large enough to describe the two broadenings.

2.4.1 Turn-on effects

If the FWHM of the inhomogeneous broadening and the homogeneous broadening sit on good combinations like those listed in Table 2-2, the simulation results show that the single-mode operation is possible to take place. For instance, in case that the FWHMs of the two broadenings both equal to 10meV, i.e., $\Gamma_{in} = \Gamma_{ho} = 10meV$, the simulation results are shown in Figure 2-5, 2-6 and 2-7.

Figure 2-5 shows the turn-on effects of this laser. (a) gives the carrier numbers of several quantum-dot groups with transition energies locating around the average transition energy, which means they have the most carrier numbers. (b) shows the generated photons of the corresponding modes, which also indicates as the modal output power. As we can see from Figure 2-5, the carrier relaxation is relatively fast, which is in less than 0.2ns. All of the 7 modes shown in the figure are stimulated in this time period, but after that, due to the modal competition, finally the central mode remains with the highest power and the other modes are suppressed. This modal competition takes a much longer time (around 2.5ns) than the carrier relaxation.

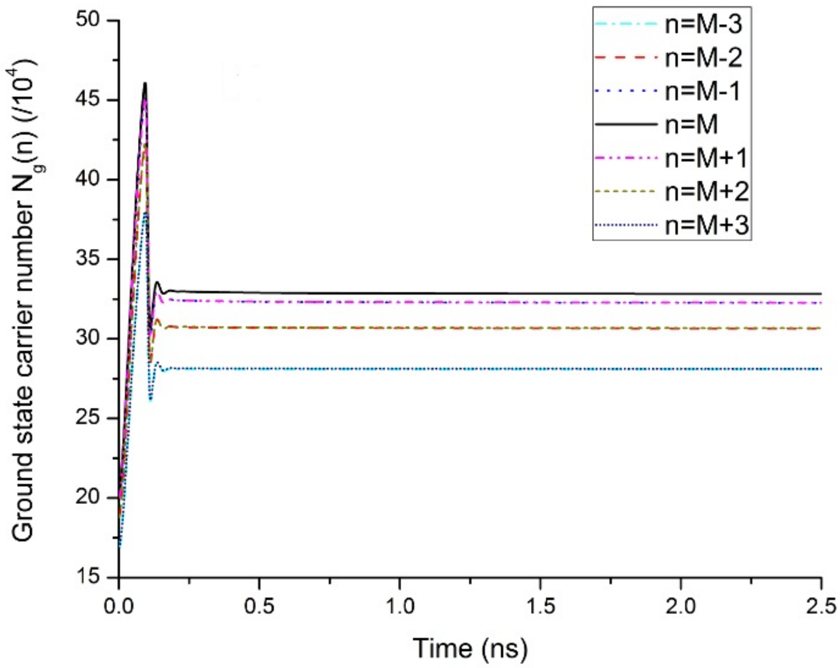

(a)

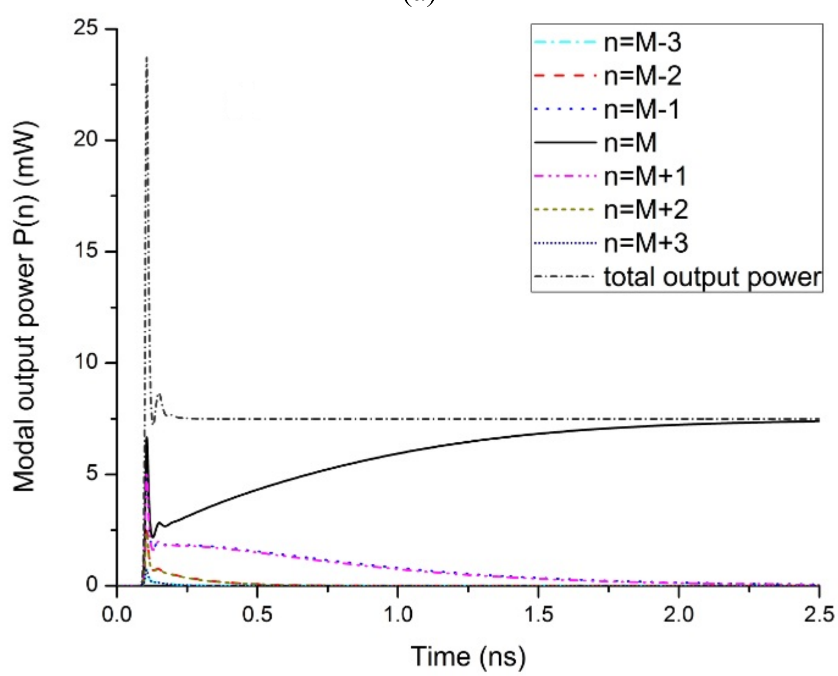

(b)

Figure 2-5. Turn-on effects: ground state carrier number in different dot groups vs. time (a); and modal/total output power vs. time (b); I=10mA

2.4.2 Gain spectrum and output power spectrum

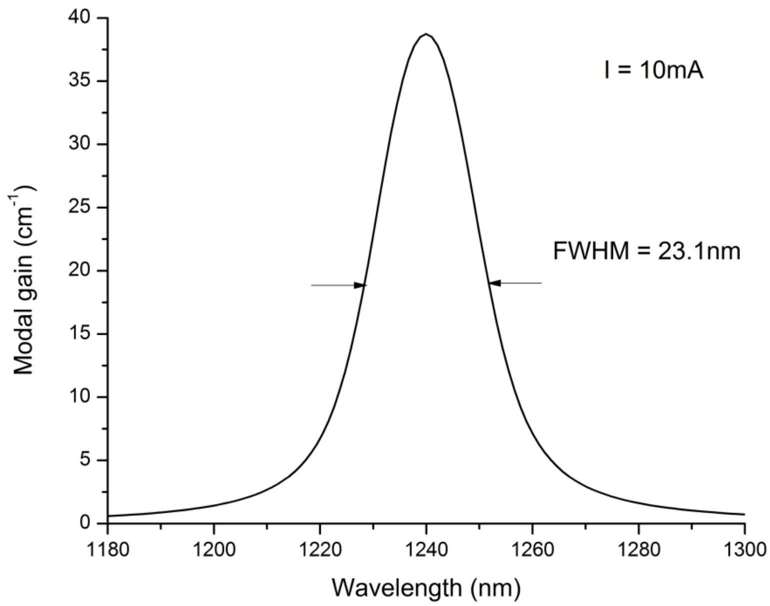

(a)

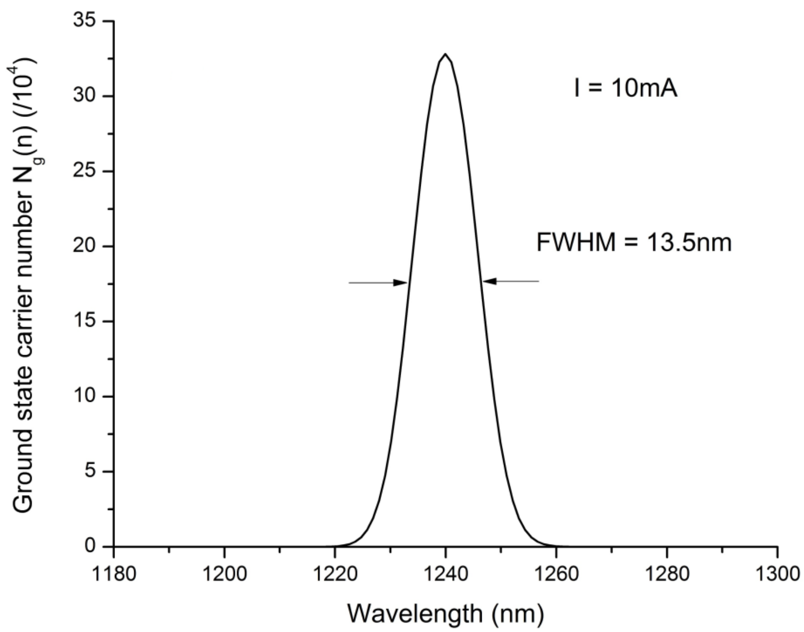

(b)

Figure 2-6. (a) Gain spectrum; and (b) ground state carrier distribution; I=10mA

When the driving current is 10mA, the Figure 2-6 records the gain spectrum and the carrier distribution. The FWHMs of them are 23.1nm and 13.5nm, respectively. The gain spectrum peak is wider than the carrier distribution peak because those carriers will contribute to the adjacent wavelengths due to the homogeneous broadening.

The output power spectrum shown in Figure 2-7 indicates that the side-mode suppression ratio (SMSR) reaches 43.7dB under 10mA driving current and 40.6dB under 5mA driving current.

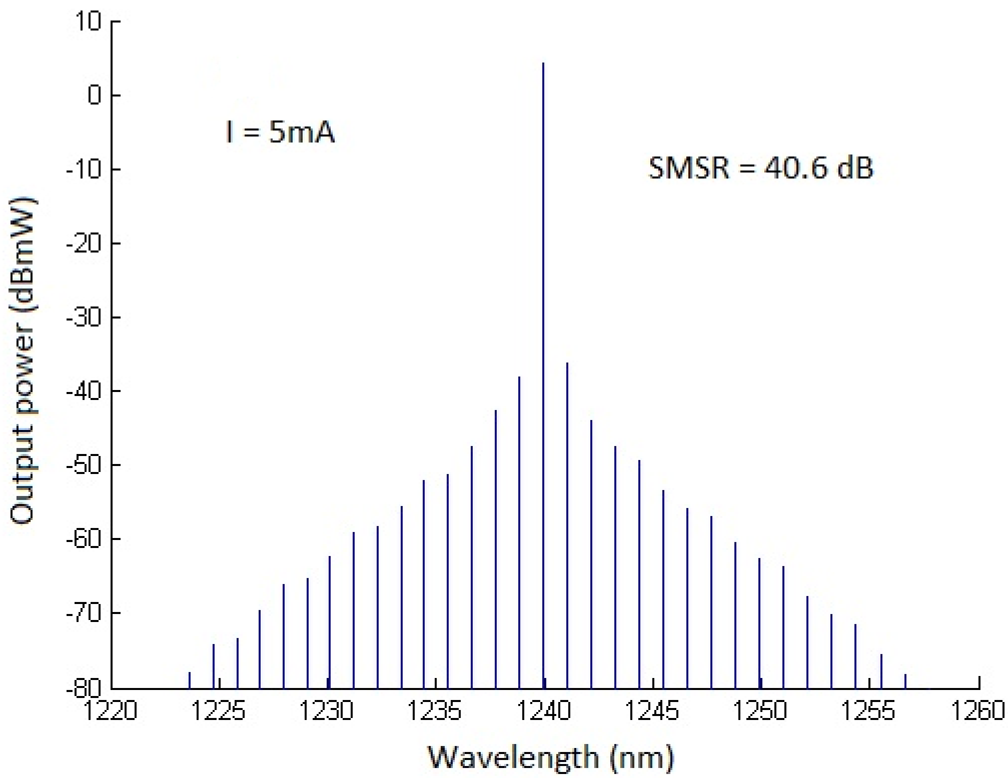

(a)

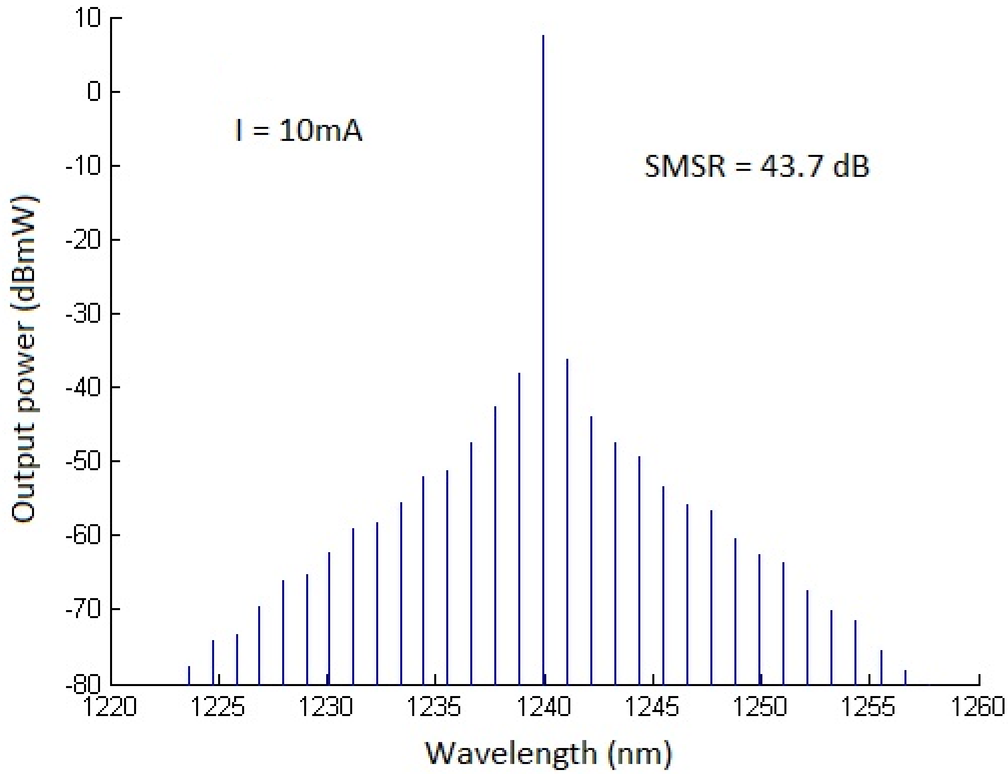

(b)

Figure 2-7. Output power spectrum; (a)I=10mA; (b)I=5mA

2.4.3 Modulation response

The direct-modulation response of the designed laser with $\Gamma_{in} = \Gamma_{ho} = 10meV$ is then simulated. The small-signal amplitude-modulation response is shown in Figure 2-8. The multiple curves are under different bias currents, which are from 2mA to 5mA, respectively.

Figure 2-8 indicates that the 3dB bandwidth is between 12GHz and 17GHz for different bias currents from 2mA to 5mA.

Generally, the relaxation frequency of a laser is proportional to, 1) the differential gain; 2) the subtraction of the driving current and the threshold current. Compared with conventional quantum-well (QW) lasers, due to the higher differential gain and lower threshold current of the QD laser, generally its relaxation frequency is easier to reach a high value even at low driving currents.

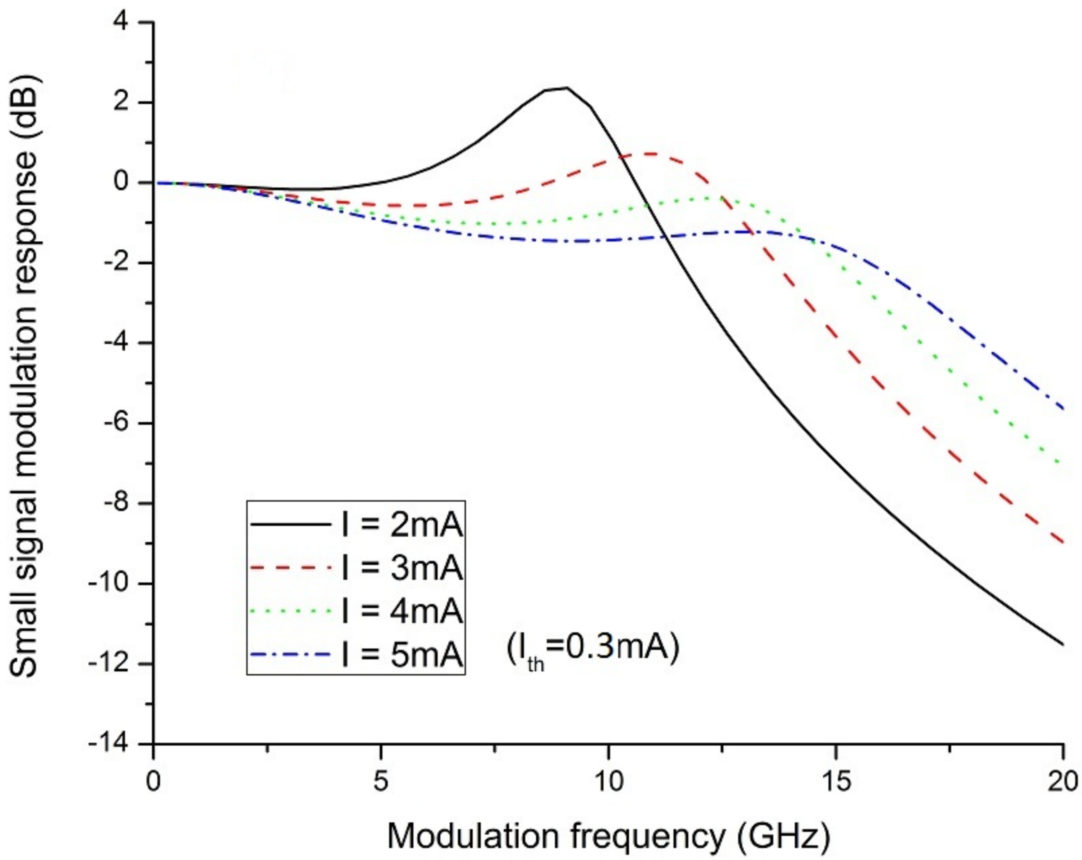

Figure 2-8. Small signal modulation response of QD laser

The other difference in the small signal response between this QD laser and the QW lasers is that, because of different schemes of the carrier transport, the corresponding carrier-transport-induced parasitic response is different. This parasitic response has a tendency to decline as the frequency increases. For QW laser, this parasitic response is relatively weak and the small signal response curve is almost flat before the peak of relaxation resonance. For QD laser, we can see in Figure 2-8, the curves start to decline before the relaxation resonance peak. This parasitic decline also gets faster if the driving current increases.

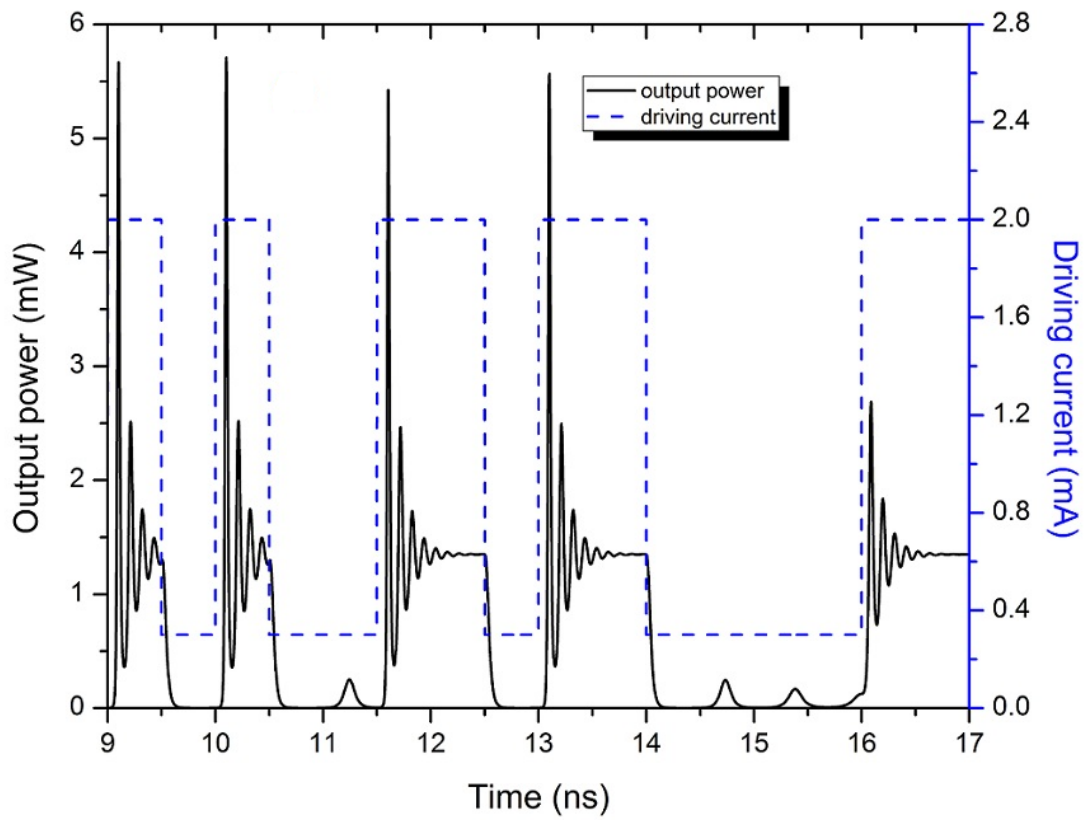

Figure 2-9. Large signal modulation response of QD laser

Figure 2-9 shows the large signal response for this designed laser. A square wave current modulation is applied, with current jumps between 0.3mA and 2mA and represents code "0" and code "1", respectively, and the frequency of the pseudo random code is 2GHz. Figure 2-9 gives the output power with modulation. For code "1", the real-time SMSR has slight changes while still remains as relatively high values. This result implies that the large signal modulation will not reduce the SMSR and this designed laser can work under large signal modulation up to several GHz.

2.5 SMSR when varying the broadening parameters

Generally, the SMSR increases when the higher driving current is applied. Figure 2-10 gives the SMSR under different driving currents. And the multiple curves in the figure are corresponding to the several optimized cases listed in Table 2-2, with respect to the settings of inhomogeneous and homogeneous broadening, which are also shown in the legend of Figure 2-10. In each case, Γ_{in} is pre-selected and Γ_{ho} is optimized to lead to a narrowest output power spectrum, thus the SMSR is expected to be the highest for the given Γ_{in} .

From Figure 2-10, we can see that the SMSR is reduced when the inhomogeneous broadening has larger width, i.e., when the inhomogeneous broadening gets wider, the best SMSR obtained by adjusting the homogeneous broadening will have to be degraded.

For a cavity length of 200μm, Figure 2-10 shows that for driving current larger than 5mA, if the inhomogeneous-broadening FWHM is lower than 17.5meV, the SMSR could be over 38dB. And consider the non-ideal laser operation conditions in reality such as the partition noise, this SMSR can be slightly reduced.

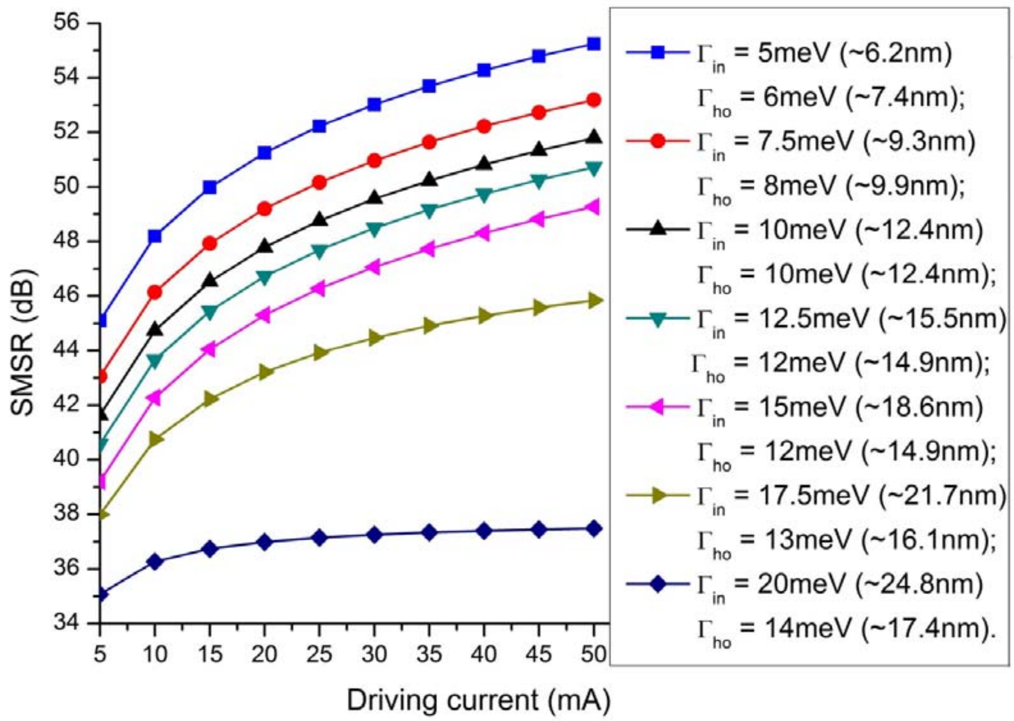

Figure 2-10. SMSR vs. driving current with different settings of inhomogeneous and homogeneous broadening

From this point of view, to design for a single-mode QD laser with a sufficient SMSR, the first requirement is that the inhomogeneous broadening has to be controlled with a limited value, which is generally the lower the better; and then following the analysis described before, the optimized homogeneous broadening can be calculated; thus with the two values the best possible SMSR can be obtained.

The other requirement is to adjust the homogeneous broadening to the optimized value. This can be achieved by carefully designing the energy levels of the QDs, for the reason that the inter-level spacing energy of the ground state and the wetting layer has influence on the homogenous broadening [20].

2.6 Summary

In this chapter the interplay of the homogeneous broadening and inhomogeneous broadening of the Fabry-Perot quantum-dot laser are researched and discussed. These two broadenings are essential to form the shape of the gain spectrum and thus determine the output power spectra. Moreover, they also decide the SMSR when the single-mode laser is designed.

In this work, the rate equation model is used to analyse the effect of the two broadenings on the laser characteristics. This model is described in details and then verified with comparison to simulation and experimental results in the reference. From the simulation experiments, we show that the inhomogeneous broadening reflects the spontaneous emission spectrum and the homogeneous broadening causes the collective lasing. As a result, the laser modal-gain and output-power spectra widths are both increase when the FWHM of inhomogeneous broadening increases; and will first decrease and then increase when the FWHM of homogeneous broadening increases.

Therefore, for each given inhomogeneous broadening Γ_{in}, the optimum homogeneous broadening Γ_{ho} can be found. While the inhomogeneous broadening is limited by the fabrication techniques, the homogeneous broadening can be tuned to match with the corresponding optimum value. This scheme can be applied for the narrow output-spectrum or the single-mode QD laser design.

Then the single longitudinal-mode QD laser is designed and the output is simulated. With a cavity length of 200μm, the SMSR under the bias current of 10mA is 43.7dB and under bias current of 5mA is 40.6dB, when the two broadening widths both equals to 10meV. Besides, the modulation response is also discussed and a 3dB bandwidth of 17GHz is achieved under the bias current of 5mA.

Moreover, several optimized values of the two broadenings parameters are also applied for this laser design and the SMSRs under different driving currents are shown. The results demonstrate that to achieve a SMSR over 38dB, the inhomogeneous broadening should be lower than 17.5meV. This work can provide a quantitative reference basis for the single-mode quantum-dot laser design.

Chapter 3

Semiconductor Nano-structure: Quantum-dot Distributed Feedback (DFB) laser

3.1 Introduction

Compared with the index-coupled DFB laser, the gain-coupled DFB laser emitting at the Bragg wavelength without the two-mode degeneracy has several remarkable advantages [56-59]. Firstly, the gain-coupled DFB laser guarantees the single-mode operation without the phase shift or anti-reflection coating which is necessary in the index-coupled DFB laser; therefore a higher production yield can be achieved. Secondly, the gain-coupled DFB laser is less sensitive to the external feedback [60-61], thus the isolator-free optical transmitter with lower cost and smaller size is enabled based on the gain-coupled DFB laser. By partially wet-etching the multiple quantum-wells active layer [62] or introducing the lateral-coupling grating [63], the gain-coupled DFB laser has been obtained experimentally.

While the fabrication techniques of the quantum dot material have become more and more mature, the quantum-dot gain-coupled DFB laser is also realized by periodically etching away some of the quantum dots [49] or using the lateral absorptive metal grating [50-51]. By going to 0-D structures for the density of states, the gain-coupled QD DFB laser inherits the merits of QD FP laser such as the higher material gain and improved temperature stability, and it also shows the above advantages of the gain-coupled lasers [23, 64-67]. Besides, the line width of QD DFB laser is found to be much narrower than that of the conventional quantum-well DFB laser at comparable output powers [65, 68], which is essential for various applications, such as coherent light sources and local oscillators in optical communication systems.

To study the performance of the QD DFB laser and further improve the laser design, a well-established and efficient numerical model is in demand. This model must at least describe three aspects of the laser characteristics, 1) the longitudinal structure along the cavity and the gain grating; 2) the carrier transport of the QDs; 3) the interplay of the inhomogeneous broadening and homogeneous broadening of the QDs.

The numerical methods for the conventional index-grating or gain-grating DFB laser have been well developed, such as the travelling wave model [69-72], the standing wave model based on the cold-cavity modes [73-74] or hot-cavity modes [75]. By these one-dimensional methods, the static and dynamic performance of laser operation and the interplay of carriers and photons along the cavity can be effectively described. These models have offered important assistance for understanding the properties and optimizing the design of conventional DFB lasers. However, for the QD DFB laser, the particular carrier-transport processes and the gain-broadening effects in the QD assemble must be further included in the modelling. To our knowledge, a comparable model for the QD DFB laser which fulfills above requirements has not yet been reported.

In this chapter, we developed a one-dimensional time-domain standing wave model for the gain-grating QD DFB laser. Illustrated in Figure 3-1 is the basic schematic structure of such laser, in which the gain grating is formed by periodically existing QD layers in the longitudinal direction. Therefore, the gain grating depends on the real-time gain of the QDs and further, the injection current. This dynamic grating is reflected in our model, as well as the carrier transport processes of the QDs. Moreover, the inhomogeneous and homogeneous broadening effects are also described by suitable probability models and involved in the modelling of the gain.

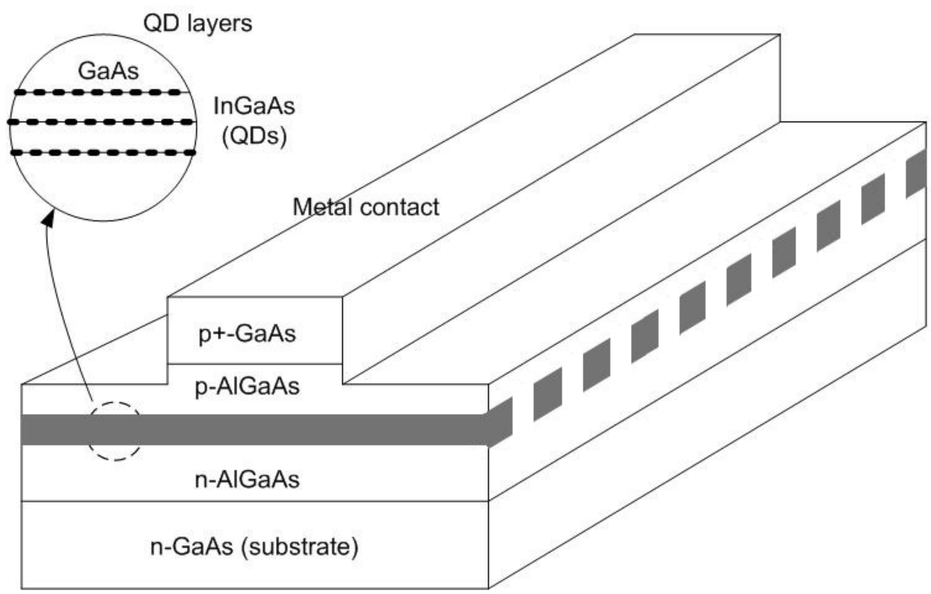

Figure 3-1. Schematic structure of the QD DFB laser

The details of the model are described in section 3.2, with all of the aspects including the gain grating, the governing coupled-wave equations, expansion of cavity modes, carrier rate-equation of the QDs and the algorithm implementation. Then in section 3.3, the simulation results of a typical example are presented and analyzed. Lastly, a brief summary is given in section 3.4.

3.2 Time-domain standing wave model for the QD DFB laser

To simulate the quantum-dot DFB laser, we developed a one-dimensional time-domain standing wave model which is based on the coupled-mode equations and the expansion on the longitudinal cavity modes. The cavity modes are firstly solved with the longitudinal characteristics of the cavity and the gain grating, and then used as the base functions when the real-time injection current is applied. At each time step, the amplitudes of the cavity modes are calculated and the one-dimensional results such as the carrier and photon distributions are obtained. This model is based on similar models which are well established and have been applied successfully on the simulation of the index-coupled DFB laser and the conventional gain-coupled DFB laser [73-76], while the carrier transport of QDs and the gain broadening effects are included. At the same time, a pre-determined coupling coefficient is used to effectively describe the gain grating and this scheme is proved to be self-consistent. Details of our model are described in this section.

3.2.1 The gain grating

When the gain grating with the period denoted as Λ is introduced, the Bragg condition gives the relationship of the Bragg wavelength λ and the period,

$$\Lambda = \frac{\lambda}{2n_{eff}} \tag{3.1}$$

where n_{eff} represents the effective index of the longitudinal mode with wavelength λ (or close to λ because of a small wavelength detuning.)

And for this chosen longitudinal mode, the modal gain of the first-order sinusoidal gain-grating can be written as,

$$g(z) = g_0 + \Delta g \sin(\frac{2\pi}{\Lambda} z) \tag{3.2}$$

Meanwhile, the gain can be regarded as an imaginary part of the complex modal index,

$$n(z) = n_0 + i\frac{g(z)}{k_0} = n_0 + i\frac{g_0}{k_0} + i\frac{\Delta g}{k_0}\sin(\frac{2\pi}{\Lambda} z) \tag{3.3}$$

where k_0 denotes the free-space wave number and n_0 represents the modal index. If there is no index-grating and the index change due to the gain grating is also negligible, n_0 is a constant. And the complex dielectric function is (with the condition that $\frac{g(z)}{k_0} << n$),

$$\varepsilon(z) = \varepsilon_0 n^2 \left(1 + i\frac{2g(z)}{k_0 n}\right) \tag{3.4}$$

Therefore, the coupling constant due to the gain grating is [77-79],

$$\kappa = i\frac{\Delta g}{2} \tag{3.5}$$

If the gain grating shows a square-wave-like perturbation varying from 0 to Γg along z-direction, and the duty cycle is 50%, as shown in Figure 3-2, we can get that the first-order coefficient $\Delta g = \Gamma g / \pi$. Then we have that $\kappa = i \dfrac{\Gamma g}{2\pi}$.

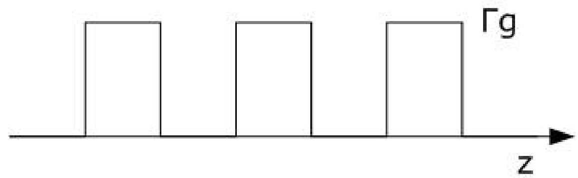

Figure 3-2. Illustration of the gain grating along *z*-direction

3.2.2 Coupled-wave equations

For the DFB laser, the grating causes the coupling between forward- and backward-propagating optical waves. This coupling can be described by the time-dependant coupled-wave equations along the *z*-direction, i.e., the direction of the light propagation [80],

$$
\begin{aligned}
\frac{1}{v_g}\frac{\partial F(z,t)}{\partial t} + \frac{\partial F(z,t)}{\partial z} &= \left[\frac{\Gamma g(z,t)}{2}\left(1 + j\alpha_m\right) - \frac{\alpha_i}{2}\right] F(z,t) + j\kappa R(z,t) + \tilde{s}_f(z,t) \\
\frac{1}{v_g}\frac{\partial R(z,t)}{\partial t} - \frac{\partial R(z,t)}{\partial z} &= \left[\frac{\Gamma g(z,t)}{2}\left(1 + j\alpha_m\right) - \frac{\alpha_i}{2}\right] R(z,t) + j\kappa F(z,t) + \tilde{s}_r(z,t)
\end{aligned}
\tag{3.6}
$$

where $F(z,t)$ and $R(z,t)$ represent the slow-varying envelopes of the forward- and backward-propagating waves, respectively; v_g denotes the group velocity, Γ the confinement factor, g the material gain, α_m the linewidth enhancement factor, α_i the internal loss, κ the coupling constant, $\tilde{s}_f(z,t)$ and $\tilde{s}_r(z,t)$ the noises generated from the spontaneous emission. According to the discussion in 3.2.1, here the coupling constant is,

$$\kappa(z,t) = i\frac{\Gamma g(z,t)}{2\pi} \tag{3.7}$$

If r_1 and r_2 represent the field reflectivities on the cavity left- and right-end facets, respectively, and L denotes the cavity length, then we have the boundary conditions,

$$\begin{aligned} F(0,t) &= r_1 R(0,t) \\ R(L,t) &= r_2 F(L,t) \end{aligned} \tag{3.8}$$

Further, the coupled-wave equations can be rewritten to [81],

$$\begin{aligned} \frac{1}{v_g}\frac{\partial F(z,t)}{\partial t} &= \left[\frac{\Gamma g(z,t)}{2}\left(1+j\alpha_m\right) - \frac{\alpha_i}{2} - \frac{\partial}{\partial z}\right]F(z,t) + j\kappa R(z,t) + \tilde{s}_f(z,t) \\ \frac{1}{v_g}\frac{\partial R(z,t)}{\partial t} &= \left[\frac{\Gamma g(z,t)}{2}\left(1+j\alpha_m\right) - \frac{\alpha_i}{2} + \frac{\partial}{\partial z}\right]R(z,t) + j\kappa F(z,t) + \tilde{s}_r(z,t) \end{aligned} \tag{3.9}$$

Using the vector representations,

$$\Psi(z,t) = \begin{bmatrix} F(z,t) \\ R(z,t) \end{bmatrix} \tag{3.10}$$

$$\tilde{S}(z,t) = \begin{bmatrix} \tilde{s}_f(z,t) \\ \tilde{s}_r(z,t) \end{bmatrix} \tag{3.11}$$

the matrix form of the coupled-wave equations is,

$$\frac{\partial \Psi}{\partial t} = H_t \Psi + v_g \tilde{S} \tag{3.12}$$

And the matrix operator H_t is,

$$H_t = v_g \begin{bmatrix} \frac{\Gamma g}{2}\left(1 + j\alpha_m\right) - \frac{\alpha_i}{2} - \frac{\partial}{\partial z} & j\kappa \\ j\kappa & \frac{\Gamma g}{2}\left(1 + j\alpha_m\right) - \frac{\alpha_i}{2} + \frac{\partial}{\partial z} \end{bmatrix} \tag{3.13}$$

3.2.3 Cavity modes

The matrix operator H_t can be written into two parts, one is related to the cavity characteristics and the gain grating; and the other is related to the gain and linewidth enhancement effect, both introduced by the bias current [81],

$$H_t = H^0 + H^I \tag{3.14}$$

$$H^0 = v_g \begin{bmatrix} -\frac{\alpha_i}{2} - \frac{\partial}{\partial z} & j\kappa \\ j\kappa & -\frac{\alpha_i}{2} + \frac{\partial}{\partial z} \end{bmatrix} \tag{3.15}$$

$$H^I = v_g \begin{bmatrix} \frac{\Gamma g}{2}\left(1 + j\alpha_m\right) & 0 \\ 0 & \frac{\Gamma g}{2}\left(1 + j\alpha_m\right) \end{bmatrix} \tag{3.16}$$

The eigen-vectors of the operator H^0, which is also called ‘the cavity modes’, are used as base functions of the mode-expansion for the real-time laser operation [81].

$$H^0 \Phi_n^0 = \xi_n^0 \Phi_n^0 \tag{3.17}$$

where ξ_n^0 denotes the *n*-th eigen-value, and the corresponding eigen-vector Φ_n^0 is,

$$\Phi_n^0(z) = \begin{bmatrix} \phi_f^0(z) \\ \phi_r^0(z) \end{bmatrix}_n \tag{3.18}$$

The subscripts f and r denotes the forward- and backward-propagating of the cavity modes, respectively. The eigen-value ξ_n^0 is a complex number, of which the real part describes the decay rate of the corresponding cavity mode and the imaginary part represents the detuning of the modal wavelength from the Bragg wavelength.

For the uniform-grating DFB laser, using the transfer matrix method, we can deduct the transcendental equation for the eigen-value ξ_n^0 [81-82],

$$\gamma_n\left(r_1 r_2 - 1\right)\cosh\gamma_n L + \left[\left(r_1 r_2 + 1\right)X_n + j\left(r_1 + r_2\right)\kappa\right]\sinh\gamma_n L = 0 \tag{3.19}$$

where,

$$\begin{aligned} X_n &= -\xi_n^0 / v_g - \alpha_i/2 \\ \gamma_n{}^2 &= X_n{}^2 + \kappa^2 \end{aligned} \tag{3.20}$$

This transcendental equation can be solved by numerical root-searching methods, i.e. giving $r_1, r_2, L, \alpha_i, \kappa$, we can get ξ_n^0.

Meanwhile, the eigen-vectors have analytical solutions,

$$\begin{bmatrix} \phi_f^0(z) \\ \phi_r^0(z) \end{bmatrix}_n = \begin{bmatrix} r_1\cosh\gamma_n z + \dfrac{r_1 X_n + j\kappa}{\gamma_n}\sinh\gamma_n z \\ \cosh\gamma_n z + \dfrac{-X_n - j\kappa r_1}{\gamma_n}\sinh\gamma_n z \end{bmatrix} \tag{3.21}$$

These eigen-vectors $\Phi_n^0(z)$ are not orthogonal to each other because the cavity is not energy conservative. However, it is proved that there is a series of adjoint eigen-vectors $W_m(z)$ which are biorthogonal to $\Phi_n^0(z)$ [81], i.e.,

$$\int_0^L \overline{\Phi}_n^0(z) \cdot \overline{W}_m(z) dz = \delta_{nm} \tag{3.22}$$

Here both eigen-vectors are normalized,

$$\begin{aligned} &\overline{\Phi}_n^0(z) = c_n \Phi_n^0(z) \\ &\left|c_n\right|^2 = \frac{1}{\int_0^L \left|\Phi_n^0(z)\right|^2 dz} \end{aligned} \tag{3.23}$$

And the adjoint eigen-vectors have the expressions that,

$$\begin{aligned} &\overline{W}_m(z) = c'_m \begin{bmatrix} \phi_r^0(z) \\ \phi_f^0(z) \end{bmatrix}_m \\ &\left|c'_m\right|^2 = \frac{1}{\int_0^L \left|W_m(z)\right|^2 dz} \end{aligned} \tag{3.24}$$

3.2.4 The standing wave model

The slow-varying envelopes of the optical waves can be expanded using the cavity modes as the base functions,

$$\Psi(z,t) = \sum_{n=1}^{K} A_n(t) \overline{\Phi}_n^0(z) \tag{3.25}$$

where $A_n(t)$ represent amplitudes of the cavity modes and vary with time. Here totally K modes are considered.

Substitute (3.25) into the coupled-wave equation (3.12), then multiply with the adjoint function $\overline{W}_m(z)$ with any m and integrate along the cavity, use equation (3.17) and the orthogonal relation (3.22), thus we can get the coupled-mode equations,

$$\frac{dA_m(t)}{dt} = p_{mm}A_m(t) + \sum_{n=1(n\neq m)}^{K} p_{mn}A_n(t) + v_g\eta_m(t) \tag{3.26}$$

where the coefficients and the noise term are,

$$p_{mm} = \xi_m^0 + \int_0^L \overline{W}_m(z)H^I\overline{\Phi}_m^0(z)dz \tag{3.27}$$

$$p_{mn} = \int_0^L \overline{W}_m(z)H^I\overline{\Phi}_n^0(z)dz \tag{3.28}$$

$$\eta_m(t) = \int_0^L \tilde{S}(z,t)\overline{W}_m(z)dz \tag{3.29}$$

3.2.5 Carrier rate-equations

Similar to the scheme used in Chapter 2, to describe the inhomogeneous and homogeneous broadening of quantum dots, firstly all of dots are grouped according to their central emission wavelength. The difference of the central emission wavelength comes from the non-uniformity of the dots in their size, shape or composition during the fabrication, i.e., the inhomogeneous broadening. Here the central emission wavelength of each group has a spacing of $\Delta\lambda$ to the next group, and totally L groups are considered for a sufficiently wide spectrum which covers over 99.9% of the dots. The dot number in the groups satisfies the Gaussian distribution. And the proportion of the dot number in each group to the total quantum-dot number is,

$$\begin{aligned} G_l &= \Delta\lambda \cdot G\left(\lambda_l - \lambda_0\right) \\ G\left(\lambda_l - \lambda_0\right) &= \frac{1}{\sqrt{2\pi}\xi_{g0}}\exp\left(-\frac{\left(\lambda_l - \lambda_0\right)^2}{2\xi_{g0}^2}\right) \end{aligned} \tag{3.30}$$

where λ_l denotes the central emission wavelength of the *l*-th group, λ_0 the central wavelength of the Gaussian distribution and ξ_{g0} the variance.

Then the probability for the *l*-th group dots to contribute to the *n*-th cavity mode is decided by the homogeneous broadening which is governed by the Lorenzian distribution,

$$\begin{aligned} L_{n,l} &= \Delta\lambda \cdot L(\lambda_n - \lambda_l) \\ L(\lambda_n - \lambda_l) &= \frac{1}{2\pi} \frac{\Gamma_{ho}}{(\lambda_n - \lambda_l)^2 + \Gamma_{ho}^2/4} \end{aligned} \tag{3.31}$$

where Γ_{ho} represents the FWHM of the Lorenzian distribution and λ_n denotes the modal wavelength of the *n*-th cavity mode, which can be calculated from the propagation constant β_n. And as discussed before, the imaginary part of the eigenvalue describes the detuning of the propagation constant of the cavity mode from the Bragg condition, then we have,

$$\beta_n = \beta_B - \frac{\mathrm{Im}(\xi_n^0)}{v_g} \tag{3.32}$$

Then we can write the carrier rate equations which describe the variation of the carrier density in the wetting layer and the ground state for each quantum-dot group,

$$\begin{aligned} \frac{dN_w(z,t)}{dt} &= \frac{I}{eV_{act}} - \frac{N_w(z,t)}{\tau_{wr}} - \frac{N_w(z,t)}{\overline{\tau}_d(z,t)} \\ \frac{dN_g^l(z,t)}{dt} &= \frac{N_w(z,t)G_l}{\tau_d^l(z,t)} - \frac{N_g^l(z,t)}{\tau_r} - v_g \sum_n \left[g_{nl}^{(1)}(z,t) S_n(z,t) \right] \end{aligned} \tag{3.33}$$

In these equations, the superscript or subscript $l = 1, 2, \cdots, L$, and we also use N_w to represent the carrier density in the wetting layer, N_g as the carrier density in the ground state, S_n as the photon density for the n-th cavity modes, V_{act} as the volume of active region, τ_d as the carrier relaxation time from the wetting layer to the ground state, τ_{wr} as the carrier recombination lifetime in the wetting layer, and τ_r as the carrier recombination lifetime in the ground state. The carrier relaxation time in the wetting-layer rate equation $\overline{\tau}_d$ takes average of τ_d in all quantum dots groups, and in each group, τ_d depends on the occupation ratio of the ground state [53],

$$\begin{aligned} \left[\overline{\tau}_d\left(z,t\right)\right]^{-1} &= \sum_l \left[\tau_d^l\left(z,t\right)\right]^{-1} G_l \\ \left[\tau_d^l\left(z,t\right)\right]^{-1} &= \tau_{d0}^{-1}\left[1 - P_l\left(z,t\right)\right] \end{aligned} \tag{3.34}$$

The occupation ratio is calculated by,

$$P_l\left(z,t\right) = \frac{N_g^l\left(z,t\right)}{2N_D G_l} \tag{3.35}$$

where N_D denotes the volume density of quantum dots.

The linear optical gain provided by the l-th group of quantum dots to the n-th cavity mode is expressed by [53],

$$g_{nl}^{(1)}\left(z,t\right) = \frac{e^2 h N_D}{c n_r \varepsilon_0 m_0^2} \frac{\left|P_{cv}^{\sigma}\right|^2}{E_l} \left[2P_l\left(z,t\right) - 1\right] G_l L_{n.l} \tag{3.36}$$

where m_0 denotes the electron mass and P_{cv}^{σ} the transition matrix element. E_l denotes the central transition energy of the *l*-th quantum-dot group, which has a simple relation with λ_l.

Then the total gain for the *n*-th cavity mode is a summation of the gain provided by all of the quantum-dot groups, i.e., $\sum_l g_{nl}^{(1)}(z,t)$, which is used in the matrix operator H^I.

The photon density in the *n*-th cavity mode is calculated from the optical-mode amplitude and the eigenfunctions,

$$S_n(z,t) = |A_n(t)|^2 \left(\left|\bar{\Phi}_f^0(z)\right|^2 + \left|\bar{\Phi}_r^0(z)\right|^2 \right) \Big|_n \tag{3.37}$$

And the output power emitted from the left or right facet is calculated by [80, 83],

$$\begin{aligned} I_n^L(t) &= S_n(0,t) \frac{hc}{\lambda_n} \frac{dw}{\Gamma} v_g \left(1 - r_1^2\right) \\ I_n^R(t) &= S_n(L,t) \frac{hc}{\lambda_n} \frac{dw}{\Gamma} v_g \left(1 - r_2^2\right) \end{aligned} \tag{3.38}$$

3.2.6 Iteration process for obtaining the coupling constant

The coupling constant is required to be pre-determined before searching for the cavity modes and solving the coupled-mode equations. As we showed in equation (3.7), the coupling constant is related to the material gain / the modal gain, i.e., $\kappa = i\frac{\Gamma g}{2\pi}$. And when the laser reaches the steady state, the modal gain $\frac{\Gamma g}{2}$ is clamped to the modal loss, which is specified in the real part of the eigen-value. If ξ_1^0 represents the first eigen-value of matrix operator H^0, of which the corresponding cavity mode is the main mode, i.e., the modal loss is the lowest, then,

$$\mathrm{Re}\left(-\frac{\xi_1^0}{v_g}\right)=\frac{\Gamma g}{2} \tag{3.39}$$

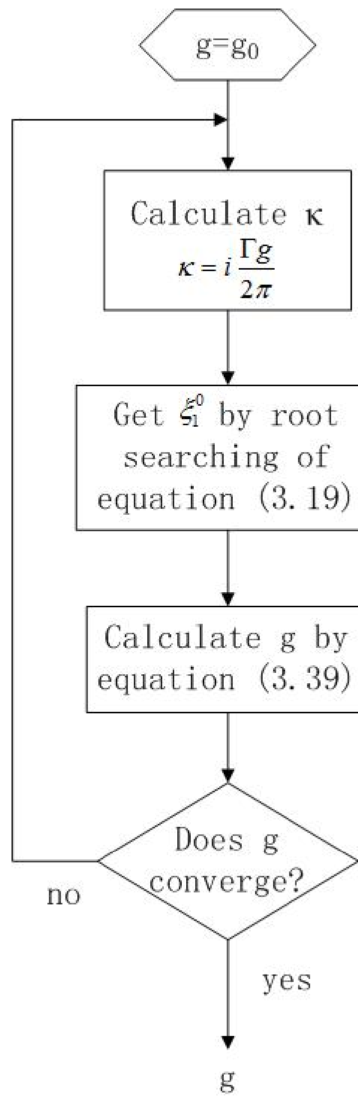

Figure 3-3. Iteration process for the threshold gain

Here, as the pre-determined values, we take constant values for the coupling constant and material gain, and ignore their variance along the cavity.

And for the purely gain-coupled DFB lasers, the main mode will be located exactly at the Bragg wavelength, i.e., the detuning is zero, thus ξ_1^0 is actually a real number. This is also proved through our root-searching program.

With these relationships, we can estimate the material gain and the coupling constant by an iteration process in a self-consistent way. Figure 3-3 shows the algorithm of the iteration process.

3.2.7 Summary of the algorithm implementation

The implementation of our algorithm is summarized as follows. Firstly the coupling constant is pre-determined by the iteration process described in section 3.3.6. Then the cavity modes are searched by solving the transcendental equation (3.19). While the eigen-values are obtained by root-searching, the eigen-vectors are calculated by expression (3.21) and normalized as shown in equation (3.23), as well as their adjoint eigen-vectors through equation (3.24).

After the cavity modes are obtained, the self-coupling term p_{mm} and the cross-coupling term p_{mn} can be calculated through equation (3.27) and (3.28). Then under a given time-dependent driving current, the coupled-mode equation (3.26) is solved by time-marching through Euler's method, together with the carrier rate equations (3.33). Meanwhile, the spontaneous emission noise term η_m is added. Therefore, the optical mode amplitudes as well as the carrier density distributions along the cavity are obtained and the laser output power is calculated at each time step.

3.3 Simulation results

The quantum-dot DFB laser in our simulation is designed as follows. The materials are all the same as those in the quantum-dot laser of Chapter 2, i.e., self-assembled InGaAs/GaAs quantum-dot layers in AlGaAs cladding and with a ridge waveguide structure. And one step further, the three layers of the quantum dots are periodically etched away to form the gain grating. The grating period is designed to make the Bragg wavelength located at the peak of the quantum-dot gain spectrum, which is 1240nm. And the anti-reflection mask is applied on the left and right end facets.

3.3.1 Parameters

Most of the parameters about the quantum-dot material are the same with those used in Chapter 2. As a typical value, the inhomogeneous broadening is assumed to be 20meV, while the homogeneous broadening is assumed to be 10meV. The parameters and their values used in simulation are listed in Table 3-1.

Table 3-1. QD DFB laser parameters [53]

Parameters	**Values**
cavity length L	300 μm
width of quantum dot layers w	10 μm
thickness of each quantum dot layer d	8 nm
number of quantum dot layers N_{qdl}	3
internal loss α_i	6 cm^{-1}
facet reflectivity r_1	0
facet reflectivity r_2	0
confinement factor Γ	0.06
effective index n_g	3.5
central lasing energy E_0	1 eV
band gap energy E_g	0.8 eV
spin-orbit interaction energy Δ	0.35 eV
electron effective mass m_e	$0.04 * m_0$
spontaneous emission coefficient β	10^{-4}
carrier lifetime in ground state τ_r	2.8 ns
carrier lifetime in wetting layer τ_{wr}	2.8 ns
relaxation lifetime τ_{d0}	10 ps
volume density of quantum dots N_D	6.3×10^{22} m^{-3}
active region volume $V_{act} = N_{qdl} dwL$	2.2×10^{-16} m^3
linewidth enhancement factor α_m	$0 \sim 2$

3.3.2 Cavity modes

For this specified quantum-dot DFB laser, from the iteration process the coupling constant is found to be $i \cdot 20.8cm^{-1}$ and the material gain is $2180cm^{-1}$. While the cavity length is $300\mu m$, $|\kappa|L$ is calculated to be around 0.62, which is close to the values researched in the reference [84].

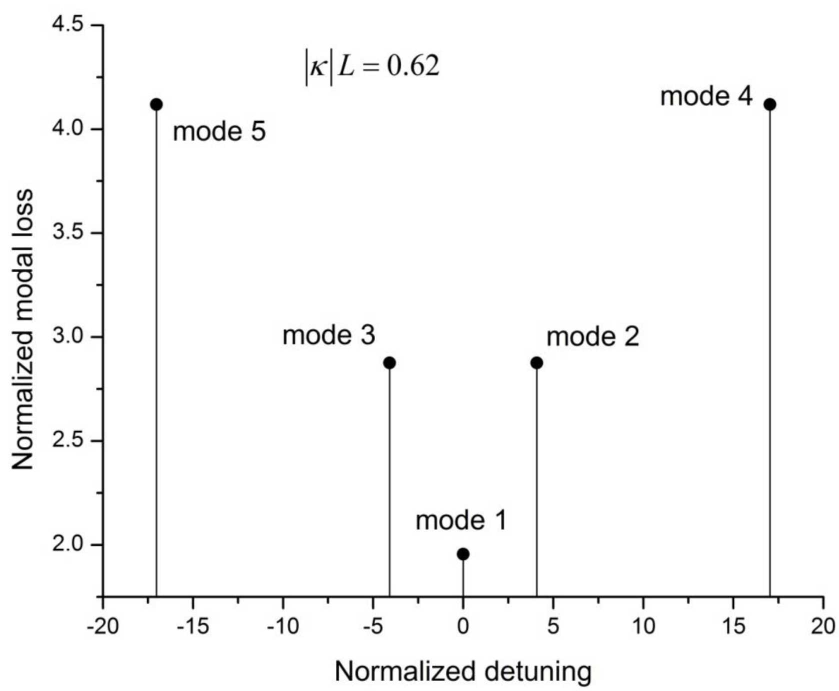

Figure 3-4. Spectrum for cavity modes of the quantum-dot DFB laser

Then the cavity modes are obtained by root-searching. Figure 3-4 gives the spectrum of the first five modes. The normalized detuning is calculated as $\mathrm{Im}\left(-\frac{\xi_n^0}{v_g}\right)L$ and the normalized modal loss as $\mathrm{Re}\left(-\frac{\xi_n^0}{v_g}\right)L$.

As shown in Figure 3-4, the mode 1 has the lowest modal loss, therefore, it will be the main mode selected in the laser. And it locates at the Bragg wavelength, which is characteristic for a purely gain-coupled DFB laser. Here the Bragg wavelength is 1240nm, the same as the peak wavelength of the quantum-dot gain spectrum; and the wavelengths of the mode 2~5 are 1236.68nm, 1243.33nm, 1226.26nm and 1254.05nm, respectively.

Then the corresponding cavity modes are calculated; modal profiles along *z*-direction are obtained and then normalized using equation (3.23). Figure 3-5 shows the normalized intensity distribution along the cavity. The intensity is a summation of the forward and the backward wave for each cavity mode, thus the distribution is symmetric because the cavity structure is symmetric along *z*-direction. As we can see, the main mode has the lowest variation along the cavity.

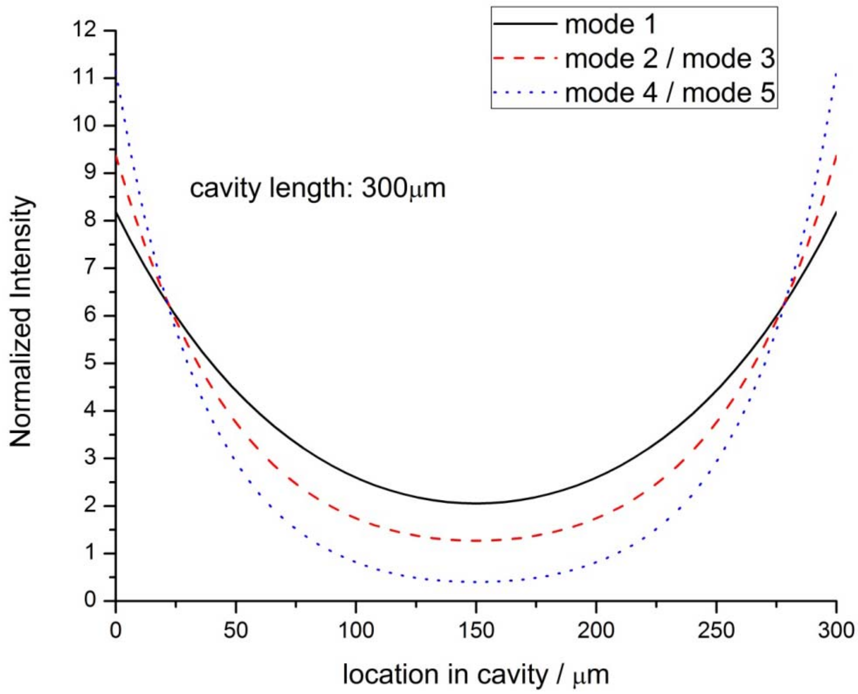

Figure 3-5. Intensity distribution of the cavity modes along the cavity

3.3.3 The laser operation

In this section, the simulation results of the laser operation is demonstrated, including the L-I curve, the output spectrum, longitudinal distributions of the carrier, photon, gain and the coupling coefficient, and dynamic responses with the small signal and large signal modulation.

I. The L-I curve

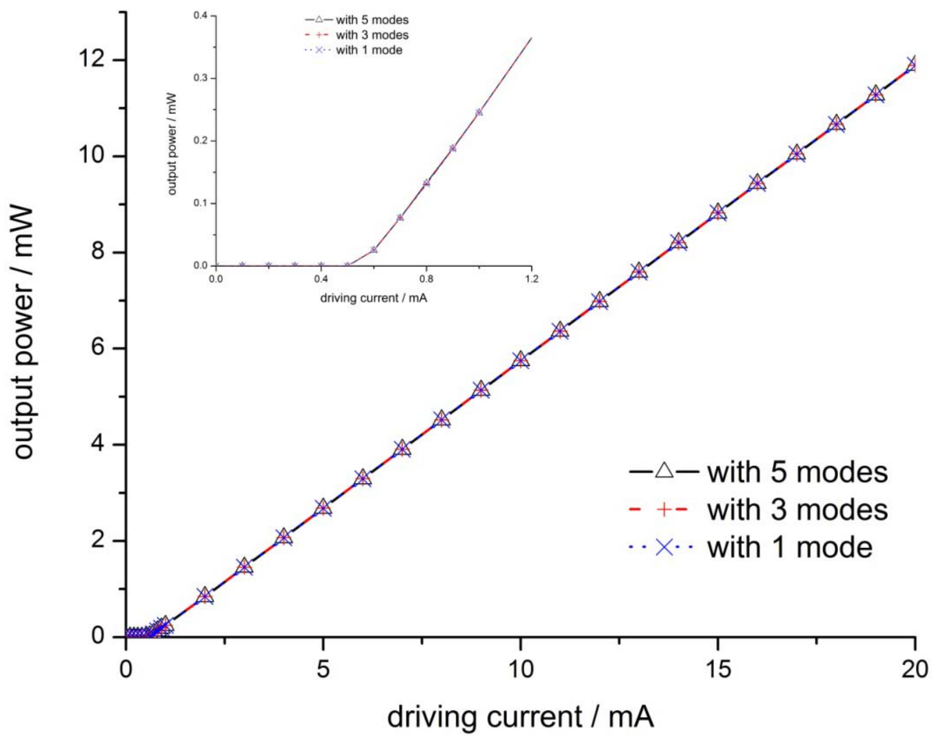

Figure 3-6. Comparison of the results using 5 modes, 3 modes and 1 mode: L-I curve of the quantum-dot DFB laser; the inset enlarges the curve around the threshold current.

Firstly the L-I curve is calculated using 5 modes, 3 modes and 1 mode, respectively. The result is compared and shown in Figure 3-6. The curves overlap quite well in the whole range as shown in this figure and the detailed inset around threshold. This means in our case only 1 mode is enough to describe the laser output while the other modes are highly suppressed.

II. The output spectrum

The output power spectrum at the injection current of 10mA shown in Figure 3-7(a) also depicts that the side modes are highly suppressed. As we can see in this figure, the side modes located at 1236.68nm and 1243.33nm have very low power and are actually drowned out in the noise. And the main mode locates at the Bragg wavelength, with a power of around 6mW. This figure shows a very high side-mode suppression ratio.

The spectrum also shows a very narrow peak. From the detailed Figure 3-7(b), the linewidth is calculated to be around 60MHz. This value is unsurprising; for quantum dot DFB lasers, the linewidth of several MHz has been reported in the experimental measurements [65]. This is mainly due to the relatively smaller linewidth enhancement factor, lower threshold current and smaller population inversion factor in the quantum-dot lasers, comparing to the quantum-well lasers [65, 85-87].

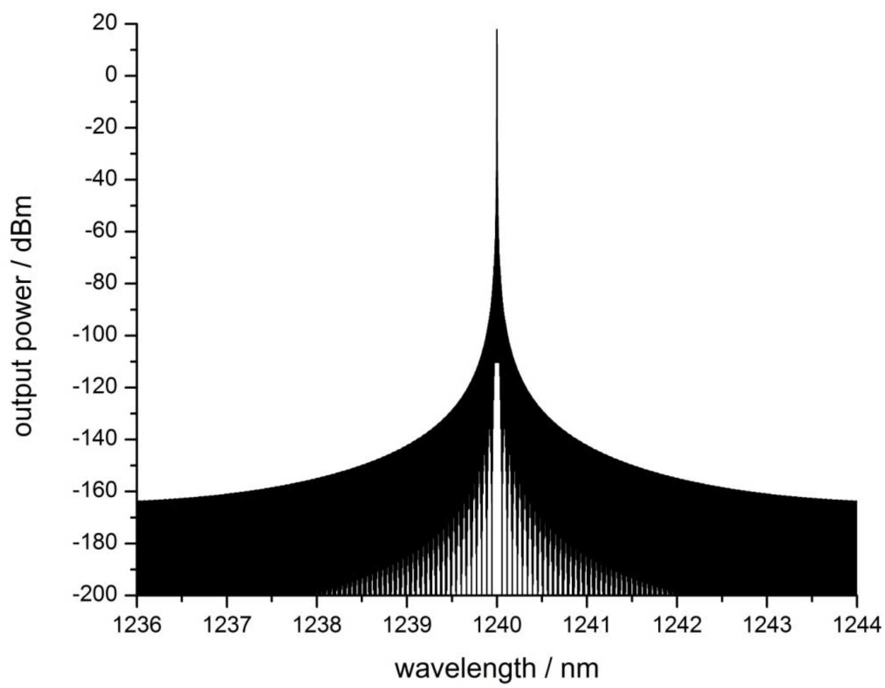

(a)

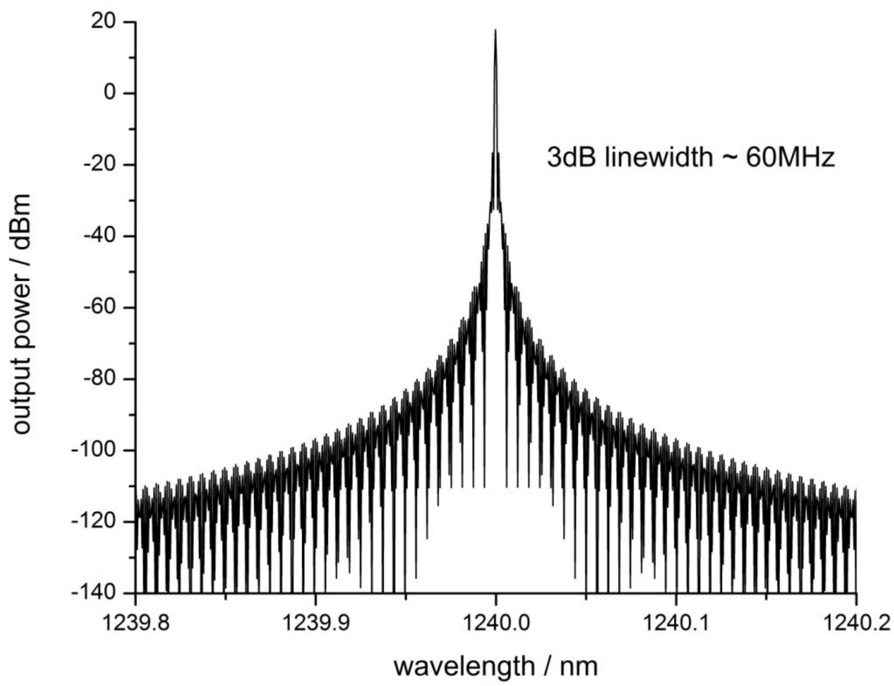

(b)

Figure 3-7. Laser output power spectrum (a); enlargement around the peak (b); I=10mA

III. Longitudinal distributions of the carrier, photon, gain and the coupling coefficient

Figure 3-8 and 3-9 demonstrate the carrier density distribution and the main-mode photon density distribution along the laser cavity at the injection current of 10mA. As we can see, for the two curves in Figure 3-8, one is the carrier density distribution in the 101^{th} quantum-dot group whose central emission wavelength locates at the Bragg wavelength; the other is the total carrier density distribution including all of the quantum-dot groups. The two curves have very similar shape, and the reason is that the carriers are all forced to contribute to the main mode in this situation. These two figures also give the information of the longitudinal spatial hole burning (LSHB) effect, which is similar to that of the uniform index-grating DFB laser.

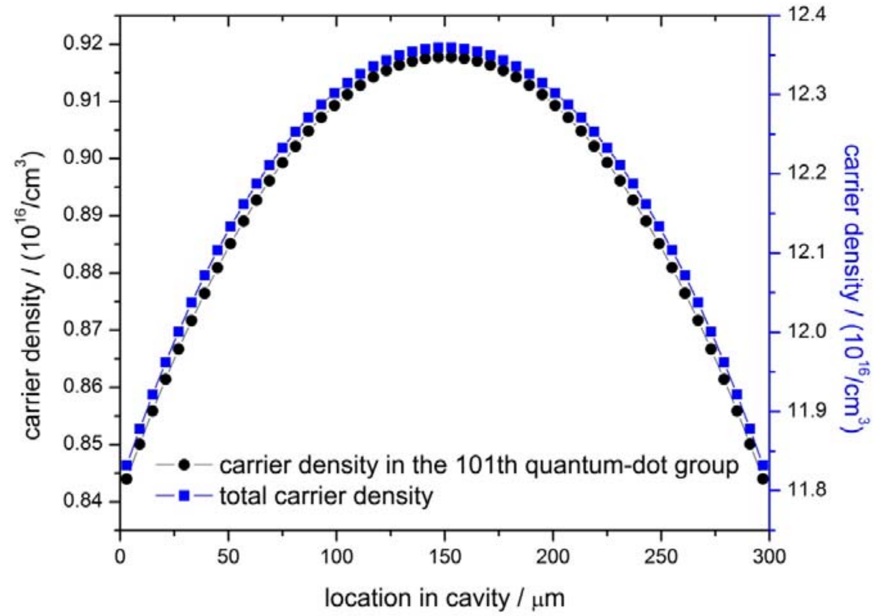

Figure 3-8. Carrier density distribution for the main mode along the cavity; I=10mA

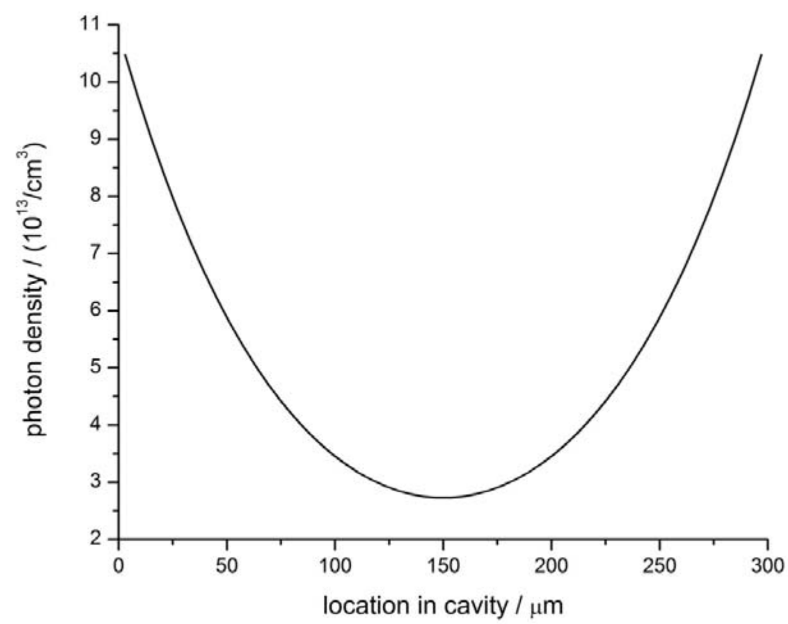

Figure 3-9. Photon density distribution for the main mode along the cavity; I=10mA

Figure 3-10 gives the longitudinal distributions of modal gain and material gain as well as the coupling coefficient along the cavity, after the laser reaches the steady state at the injection current of 10mA. The gain is not uniform along the cavity because of the non-uniform carrier distribution. As we can see, in the central part of the cavity, the gain is higher because the carrier density is also higher. Thus the coupling coefficient which is proportional to the gain shows a similar distribution. In our simulation, the average of the material gain and the coupling coefficient are very close to the estimated values obtained from the pre-executed iteration process, as a proof of the consistency of this method.

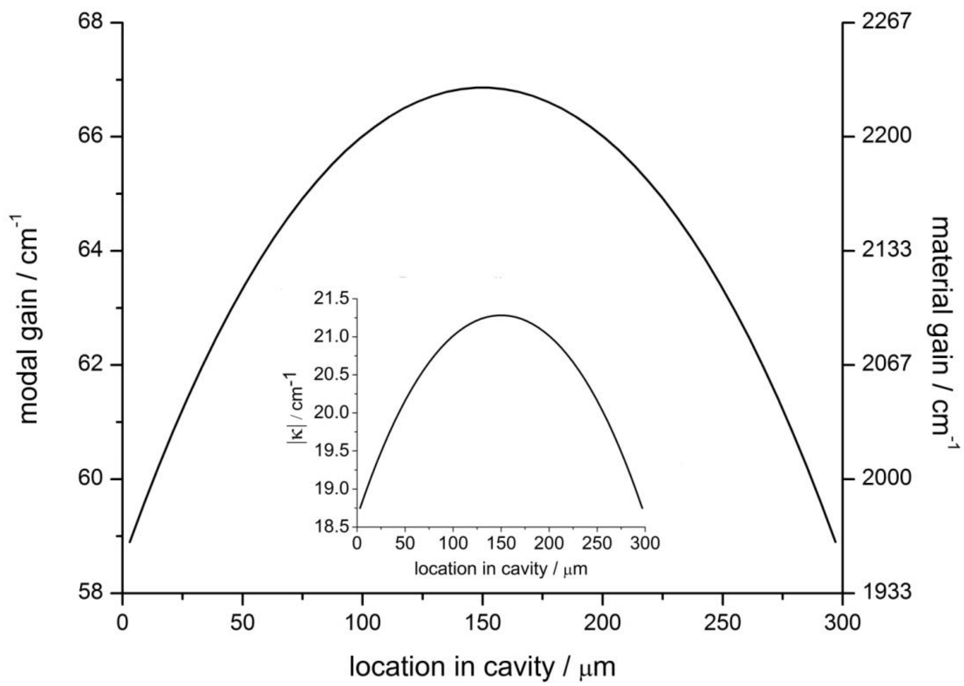

Figure 3-10. The gain distribution and the coupling coefficient for the main mode along the cavity; I=10mA

IV. Dynamic responses

The small signal responses of this QD DFB laser at three bias currents close to the threshold are shown in Figure 3-11. From this figure, we can see that the relaxation frequency get higher when the bias current increases. However, the carrier-transport-induced parasitic response which is explained in last chapter declines quite fast in this case and limits the 3dB bandwidth, and when the bias current is higher, this parasitic decline is even worse.

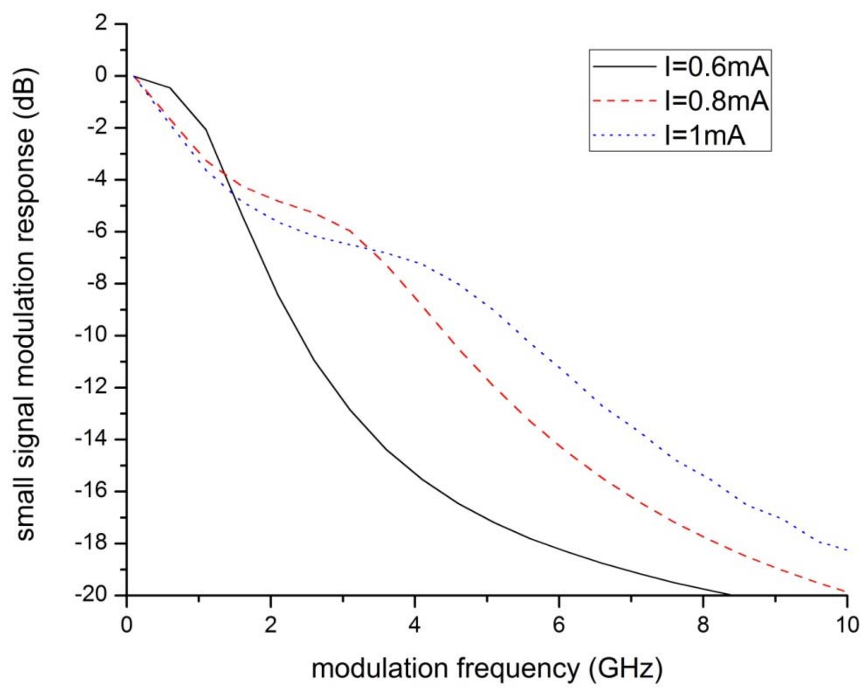

Figure 3-11. Small signal modulation response of the QD DFB laser

The reason of this fast decline is that, in this QD DFB laser, all of the carriers are forced to contribute to the main optical mode, thus the carrier transport process takes longer time compared to that in the QD Fabry-Perot laser which is studied in last chapter.

Figure 3-12 demonstrates the large signal response of the QD DFB laser. The current jumps between 0.6mA and 0.7mA, with frequency of 0.2GHz or 1GHz. In the case of 0.2GHz, the output power follows the current changes and shows flat tops and bottoms; however, in the case of 1GHz, the output power cannot follow and it is more like a triangular wave.

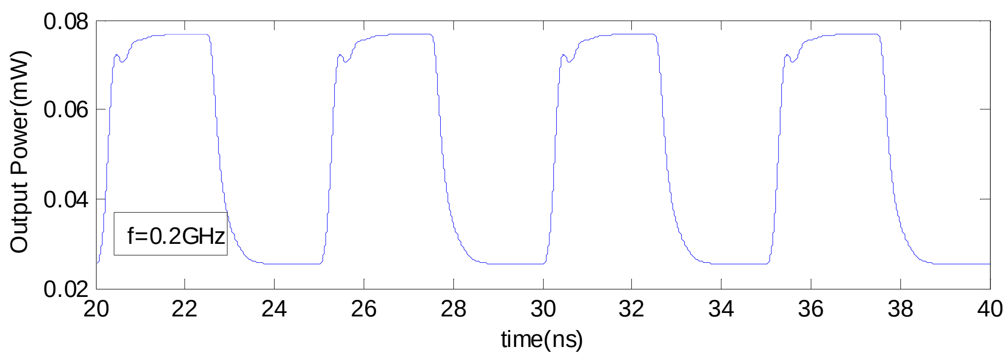

(a)

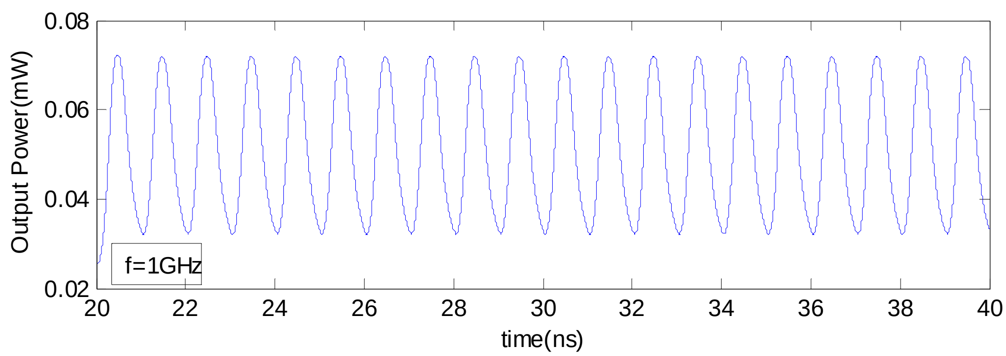

(b)

Figure 3-12. Output power vs. time with square wave modulation; current from 0.6mA to 0.7mA; (a) f=0.2GHz; (b) f=1GHz

From the simulation results, this laser design is not the best for the modulation response. Therefore, more research is required for the carrier transport and the corresponding modulation response, which for now we know that it is like a parasitic RC time constant. It is possible to improve the modulation response of the QD DFB laser by optimizing the laser design.

3.4 Summary

In this work, a one-dimensional time-domain standing wave model is designed for the first time for the simulation of the gain-grating QD DFB laser. The cavity modes of such laser are obtained and analysed, which are similar to the cavity modes in a conventional gain-grating DFB laser. In this model, the inhomogeneous and homogeneous broadening effects are included for the QD assemble, and the carrier transport processes are described by the rate equations which are also one-dimensional along the cavity.

The simulation results for a typical gain-coupled QD DFB laser are demonstrated. For this specified laser, only one cavity mode is enough for the method, showing a very high side-mode suppression ratio. The output spectrum also proves that. Moreover, a quite narrow linewidth of about 60MHz is achieved.

The simulation also gives details about the longitudinal distributions of the carrier, photon, gain and the coupling coefficient. It shows that the longitudinal spatial hole burning (LSHB) effect of this laser has a similar shape to that of the uniform index-grating DFB laser.

The dynamic responses of the given laser with the small signal and large signal modulation are also simulated. The results show that the carrier-transport-induced parasitic response declines quite fast and limits the modulation bandwidth. Based on this conclusion, further research can be carried on for reducing this response and optimizing the laser design.

Chapter 4

Metal Nano-particle: Mie Theory Calculation for Optical Properties of a Single Particle

4.1 Introduction

In recent years the fabrication of metal nano-particle with different size, shape and composition has been rapidly advanced, thanks to the development of lithography techniques and wet chemical methods [88-91]. Various applications of these particles are also found in a wide range of engineering, chemistry and biology and make the metal particle to be an important component in nano-optics [5, 92-95].

The most special and attractive feature of this metal nano-particle is its plasmon resonance with an incident electromagnetic wave, and the resonance wavelength often locates in the light wave range [96-98]. This is also called the localized surface plasmon polariton (LSPP) effect. With the incidence of the electromagnetic wave, the electrons inside of the particle including the free electrons and the inner electrons have collective motion coursed by the oscillating electrical field. Then the electrons movement introduces a dipole and higher-order electrical and magnetic poles, radiating new electromagnetic wave and generating a local field. At a specific frequency, a strong resonance happens, and the local field is enhanced. This resonance frequency is generally determined by the particle size, shape and composition.

The absorption and scattering of the metal nano-particle can be calculated by the classical Mie theory, provided that the size-dependent dielectric constants are used to describe the quantum effects [99-101]. Mie theory gives rigorous solution for the spherical shape particle; and for the particle with other shapes, if the dipole is dominated in the motion of electrons, for example, in the ellipsoid or nano-rod, it can also provide approximated results [102-105].

While the metal particle has many applications in other areas, our purpose is to investigate its potential applications in the optoelectronic devices. For this purpose, the optical properties of the noble metal nano-particle are researched and calculated by the Mie theory. We find that there are two major restrictions for its potential applications in this area. One is that, for the noble metal nano-particle, the resonance peak generally locates in the range of 300~600nm, which is away from the wavelengths used for optical communications. The other issue is that, because the metal has strong absorption to the light wave, the Q-factor is restricted, and the peak has a width generally larger than dozens of nanometers. Therefore, in this work some methods are discussed to push through these restrictions.

In this chapter, firstly the Mie theory is reviewed, and then the calculation results of the metal nano-particles are given and the plasmon resonance is investigated. Then several methods of moving the resonance peak to longer wavelength are discussed. In the last part, the mechanism that the resonance peak can be narrowed by reducing the absorption is testified.

4.2 Mie theory for the metal nano-particle

4.2.1 The classical Mie theory

In a homogeneous medium, the fields **E** and **H** satisfy the Maxwell vector wave equations,

$$\nabla^2 \mathbf{A} + k^2 m^2 \mathbf{A} = 0 \tag{4.1}$$

where **A** represents **E** or **H**, *k* represents the wave vector in vacuum and *m* represents the refractive index of the medium.

If there is a solution ψ for the scalar wave equation $\nabla^2 \psi + k^2 m^2 \psi = 0$, it can be proved that the vectors $\mathbf{M}_\psi$ and $\mathbf{N}_\psi$ satisfy the vector wave equation with the following definitions [102],

$$\begin{aligned} \mathbf{M}_\psi &= \nabla \times (\mathbf{r}\psi) \\ mk\mathbf{N}_\psi &= \nabla \times \mathbf{M}_\psi \end{aligned} \tag{4.2}$$

Moreover, they are also related by,

$$mk\mathbf{M}_\psi = \nabla \times \mathbf{N}_\psi \tag{4.3}$$

From this statement, if there are two solutions *u* and *v* of the scalar wave equation, the following is a solution to Maxwell equations,

$$\begin{cases} \mathbf{E} = \mathbf{M}_v + i\mathbf{N}_u \\ \mathbf{H} = m\left(-\mathbf{M}_u + i\mathbf{N}_v\right) \end{cases} \tag{4.4}$$

The classical Mie theory is an analytical solution to the Maxwell vector wave equations in spherical coordinates, to describe the plane-wave scattering by a homogeneous sphere (with the refractive index m_1) in an infinite medium (with the refractive index m).

The incident plane wave can be described by,

$$\begin{cases} \mathbf{E} = \hat{x}\exp(-ikmz + i\omega t) \\ \mathbf{H} = \hat{y}\exp(-ikmz + i\omega t) \end{cases} \tag{4.5}$$

It can also be written in the form of (4) with u and v given as follows in spherical coordinates [102],

$$\begin{cases} u = \exp(i\omega t)\cos\varphi \sum_{n=1}^{\infty} (-i)^n \dfrac{2n+1}{n(n+1)} P_n^1(\cos\theta) j_n(kmr) \\ v = \exp(i\omega t)\sin\varphi \sum_{n=1}^{\infty} (-i)^n \dfrac{2n+1}{n(n+1)} P_n^1(\cos\theta) j_n(kmr) \end{cases} \tag{4.6}$$

where P_n^1 is the associated Legendre polynomial of the first degree, and j_n is the spherical Bessel function.

The scattered wave also can be expressed by the same form with similar expansion [102],

$$\begin{cases} u = \exp(i\omega t)\cos\varphi \sum_{n=1}^{\infty} -a_n (-i)^n \dfrac{2n+1}{n(n+1)} P_n^1(\cos\theta) h_n^{(2)}(kmr) \\ v = \exp(i\omega t)\sin\varphi \sum_{n=1}^{\infty} -b_n (-i)^n \dfrac{2n+1}{n(n+1)} P_n^1(\cos\theta) h_n^{(2)}(kmr) \end{cases} \tag{4.7}$$

where $h_n^{(2)}$ represents the spherical Bessel function of the second kind; a_n and b_n indicate the n-th order coefficients that are to be determined, and represent the amplitudes of the *n*-th order electrical pole and the *n*-th magnetic pole, respectively. For instance, a_1 represents the intensity of the electrical dipole.

The wave inside the sphere is expressed by [102],

$$\begin{cases} u = \exp(i\omega t)\cos\varphi \sum_{n=1}^{\infty} m_1 c_n (-i)^n \dfrac{2n+1}{n(n+1)} P_n^1(\cos\theta) j_n(kmr) \\ v = \exp(i\omega t)\sin\varphi \sum_{n=1}^{\infty} m_1 d_n (-i)^n \dfrac{2n+1}{n(n+1)} P_n^1(\cos\theta) j_n(kmr) \end{cases} \tag{4.8}$$

where c_n and d_n are also coefficients to be determined.

The coefficients can be determined by matching the boundary conditions on the surface of the spherical particle. As we know, the tangential components ($\mathbf{E}_\theta, \mathbf{E}_\varphi, \mathbf{H}_\theta, \mathbf{H}_\varphi$) are continuous on the surface, which means that these four expressions (from (4.2), (4.3), (4.4))

$$v, \quad \frac{1}{m}\frac{\partial(ru)}{\partial r}, \quad mu, \quad \frac{\partial(rv)}{\partial r}$$

all have the same values at either side of the boundary (r = a). Therefore, the coefficients can be solved with deductions [102],

$$\begin{aligned} a_n(x,y) &= \frac{\psi_n'(y)\psi_n(x) - m\psi_n(y)\psi_n'(x)}{\psi_n'(y)\xi_n(x) - m\psi_n(y)\xi_n'(x)} \\ b_n(x,y) &= \frac{m\psi_n'(y)\psi_n(x) - \psi_n(y)\psi_n'(x)}{m\psi_n'(y)\xi_n(x) - \psi_n(y)\xi_n'(x)} \end{aligned} \tag{4.9}$$

where,

$$\begin{aligned} x &= 2\pi a/\lambda = 2\pi am/\lambda_{vac} \\ y &= xm_1/m \end{aligned} \tag{4.10}$$

and,

$$\psi_n(\rho) = \sqrt{\frac{\pi\rho}{2}} J_{n+1/2}(\rho)$$
$$\xi_n(\rho) = \sqrt{\frac{\pi\rho}{2}} H^{(2)}_{n+1/2}(\rho) \tag{4.11}$$

Therefore, the solution with the parameters x and y can be obtained [102],

$$\mathbf{E}_\theta = \mathbf{H}_\varphi = -\frac{i}{kr}\exp(-ikmz + i\omega t)\cos\varphi S_2(\theta)$$
$$-\mathbf{E}_\varphi = \mathbf{H}_\theta = -\frac{i}{kr}\exp(-ikmz + i\omega t)\sin\varphi S_1(\theta) \tag{4.12}$$

where the scattering functions are,

$$S_1(\theta) = \sum_{n=1}^{\infty} \frac{2n+1}{n(n+1)}\left(a_n \pi_n(\cos\theta) + b_n \tau_n(\cos\theta)\right)$$
$$S_2(\theta) = \sum_{n=1}^{\infty} \frac{2n+1}{n(n+1)}\left(b_n \pi_n(\cos\theta) + a_n \tau_n(\cos\theta)\right) \tag{4.13}$$

and the Mie angular functions are defined as,

$$\pi_n(\cos\theta) = \frac{1}{\sin\theta} P_n^1(\cos\theta)$$
$$\tau_n(\cos\theta) = \frac{d}{d\theta} P_n^1(\cos\theta) \tag{4.14}$$

4.2.2 Efficiency factors and cross sections for extinction, scattering and absorption

From the scattering theory, the three dimensionless efficiency factors (or Mie coefficients) for the extinction, scattering and absorption are defined as below [103],

$$\begin{aligned} Q_{ext} &= C_{ext} / G \\ Q_{sca} &= C_{sca} / G \\ Q_{abs} &= C_{abs} / G \end{aligned} \tag{4.15}$$

where G is the geometrical cross section of the particle, for instance, $G = \pi a^2$ for a sphere of radius a; C_{ext}, C_{sca} and C_{abs} are the cross sections for the extinction, scattering and absorption, respectively. Those are defined as the equivalent areas on which the incident energy equals to the extinct, scattered or absorbed energy, respectively. And the extinct energy is the sum up of the scattered and absorbed energy, therefore we have,

$$Q_{abs} = Q_{ext} - Q_{sca} \tag{4.16}$$

Due to the fundamental extinction formula, which gives the extinction cross-section of a particle, we have [105-106],

$$C_{ext} = \frac{4\pi}{k^2} \operatorname{Re}\{S(0)\} \tag{4.17}$$

and from (4.13),

$$S(0) = S_1(0) = S_2(0) = \frac{1}{2} \sum_{n=1}^{\infty} (2n+1)\left(a_n + b_n\right) \tag{4.18}$$

Therefore,

$$Q_{ext} = \frac{2}{x^2} \sum_{n=1}^{\infty} (2n+1) \operatorname{Re}\left(a_n + b_n\right) \tag{4.19}$$

Also for the scattering efficiency factor, we have,

$$Q_{sca} = \frac{2}{x^2} \sum_{n=1}^{\infty} (2n+1)\left(\left|a_n\right|^2 + \left|b_n\right|^2\right) \tag{4.20}$$

The absorption efficiency factor can be calculated by the subtraction of the above two factors.

4.2.3 Small-particle limit ($a << \lambda$) and the dipole approximation

Under the small-particle limit $|m|x << 1$, *i.e.,* $a << \lambda$, the entire particle experiences nearly the same electric field and behaves as a single electric dipole. Thus it is quasi-static and can be solved under the dipolar approximation; in this case, the Mie theory reduces to the so-called Rayleigh scattering theory [102].

With the dipole approximation, among the Mie coefficients, only the first one remains a non-zero value as [102],

$$a_1 = -P\frac{2ix^3}{3} \qquad \text{where,} \quad P = \frac{m_1^2 - m^2}{m_1^2 + 2m^2} \tag{4.21}$$

then,

$$\begin{aligned} S_1 &= \frac{3}{2}a_1 \\ S_2 &= \frac{3}{2}a_1 \cos\theta \end{aligned} \tag{4.22}$$

Therefore,

$$Q_{abs} = Q_{ext} - Q_{sca} = 4x \operatorname{Im} P - \frac{8x^4}{9}|P|^2 \tag{4.23}$$

With the small-particle limit, the second term can be neglected. Then,

$$Q_{abs} = 4x \operatorname{Im} P \tag{4.24}$$

From the expressions (4.24), (4.21) and (4.10), the absorption cross-section is,

$$\begin{aligned}
C_{abs} = \pi a^2 \cdot Q_{abs} &= 4\pi x a^2 \,\mathrm{Im}\left(\frac{m_1^2 - m^2}{m_1^2 + 2m^2}\right) \\
&= \frac{8\pi^2 m}{\lambda_{vac}} a^3 \,\mathrm{Im}\left(\frac{m_1^2 - m^2}{m_1^2 + 2m^2}\right) \\
&= \frac{4\pi\omega}{c} \varepsilon_m^{1/2} a^3 \,\mathrm{Im}\left(\frac{\varepsilon - \varepsilon_m}{\varepsilon + 2\varepsilon_m}\right)
\end{aligned} \tag{4.25}$$

where ε and ε_m are the dielectric functions of the spherical particle and the surrounding medium, respectively.

4.2.4 Ellipsoidal particle or nano-rod

Comparing to the sphere particle, the ellipsoidal shape causes splitting of the resonance peak due to the three unequal axes.

Under the dipolar approximation, for incident light polarized along the *i* direction (*i*=*x*,*y*,*z*), the absorption cross section is [102],

$$C_{abs} = \frac{2\pi V \varepsilon_m^{3/2}}{\lambda L_i^2} \frac{\varepsilon_i}{\left| \varepsilon + \frac{1 - L_i}{L_i} \varepsilon_m \right|^2} \tag{4.26}$$

where L_i is a direction-dependent factor determined by the ellipsoid shape.

For spheres, $L_i = 1/3$. For spheroids, which is a special case for ellipsoid that two of the three axes have equal length, we have, $L_x + L_y + L_z = 1$.

There are two categories of the spheroid,

(1) Prolate spheroid, which has a cigar shape, i.e., the two short axes are equal, a>b=c; we have [102],

$$L_y = L_z = \left(1 - L_x\right)/2 > 1/3 > L_x \tag{4.27}$$

$$L_x = \frac{1-e^2}{e^2}\left(\frac{1}{2e}\ln\frac{1+e}{1-e} - 1\right) \tag{4.28}$$

(2) Oblate spheroid, which has a disk shape, i.e., the two long axes are equal, a=b>c; we have [102],

$$L_z = 1 - 2L_x > 1/3 > L_x = L_y \tag{4.29}$$

$$L_x = \frac{\left(1-e^2\right)^{1/2}}{2e^3}\left[\frac{\pi}{2} - \arctan\frac{\left(1-e^2\right)^{1/2}}{e}\right] - \frac{1-e^2}{2e^2} \tag{4.30}$$

where,

$$\begin{aligned} e^2 &= 1 - \eta^2 \\ \eta &= c/a \end{aligned} \tag{4.31}$$

The nano-rod can also be simulated by a similar η, which is defined as the ratio of the short axis to the long axis.

4.2.5 Dielectric function of the metal particle

Noble metals have unique electron configurations. Firstly, the *d*-shell is closed, which is different from other transition metals with open *d*-shells. This means *s*-band and *d*-band are separated from each other. Secondly, the valence *d*-band and conduction *s*-band have a quite small energy gap, which means the *d*-electrons have strong impact on the free electrons and then influence the optical properties. This feature differs from alkali metals, of which the interaction between *s*-electron and *d*-electron is very weak thus the pure jellium model can be used.

Therefore, the dielectric function of the noble metal $\varepsilon(\omega)$ contains two contributions from *s*-band and *d*-band electrons (respectively the free electrons or the intra-band parts, and the bounded electrons or the inter-band parts) [107],

$$\varepsilon(\omega) = \varepsilon^s(\omega) + \varepsilon^d(\omega) - 1 \tag{4.32}$$

$\varepsilon^s(\omega)$ can be expressed by the Drude model; and for the nano-particle, a size-dependent electron scattering rate $\Gamma(R)$ is introduced because of the mean-free-path effect [108], which is due to the electrons scattering by the particle surface.

$$\varepsilon^s(\omega) = 1 - \frac{\omega_p^2}{\omega(\omega + i\Gamma(R))} \tag{4.33}$$

Or with $E = \hbar\omega$, the above expression is rewritten to,

$$\varepsilon^s(E) = 1 - \frac{E_p^2}{E(E + i\hbar\Gamma(R))} \tag{4.34}$$

And,

$$\hbar\Gamma(R) = \hbar\Gamma_\infty + \frac{A\hbar v_F}{1.602\times10^{-19}\cdot R} \tag{4.35}$$

where,

A is a model-dependent parameter and is set to 1 in calculation;

$\hbar\Gamma_\infty$ is taken equal to 0.1eV;

$E_p = \hbar\omega_p$ is the plasma energy/frequency and the values are respectively 9.07eV (copper), 8.85eV (silver) and 8.98eV (gold);

v_F is the Fermi velocity and the values are respectively $1.57\times10^6 m/s$ (copper), $1.39\times10^6 m/s$ (silver) and $1.40\times10^6 m/s$ (gold);

$\varepsilon^d(\omega)$ of the three noble metals, which are experimentally measured, are found in the reference [107].

4.3 Optical properties of the metal nano-sphere

Mie theory is rigorous for the sphere with the plane-wave incidence. Because the nano-particle considered here is generally very small compared to the incident light wavelength, in most cases, the particle cannot see the spatial variance of the incident amplitude, thus it can be regarded as the plane wave. Based on this assumption, the scattering and absorption of the metal particle to the light wave are calculated.

4.3.1 Localized surface plasmon resonance: the multi-poles

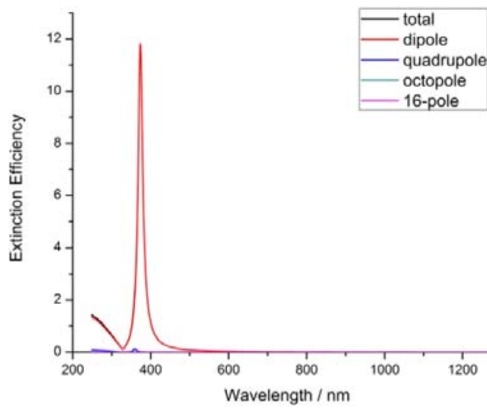

(a) R=20nm

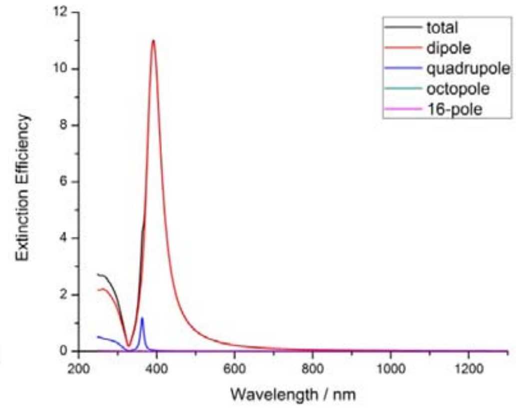

(b) R=40nm

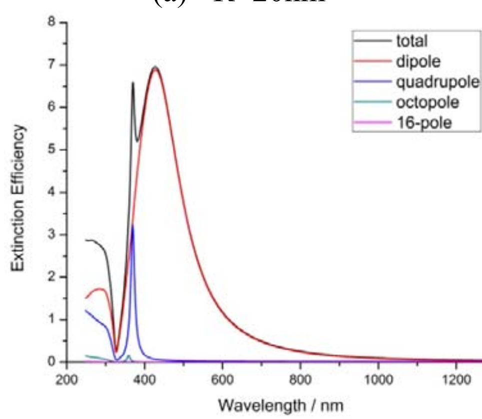

(c) R=60nm

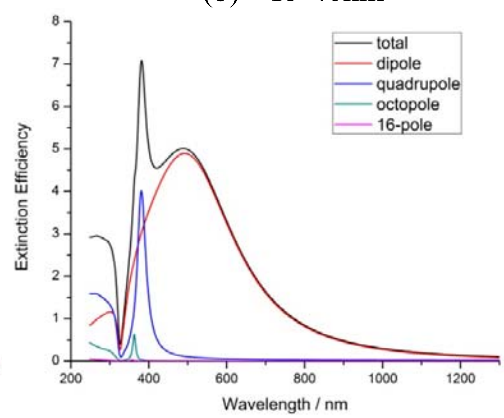

(d) R=80nm

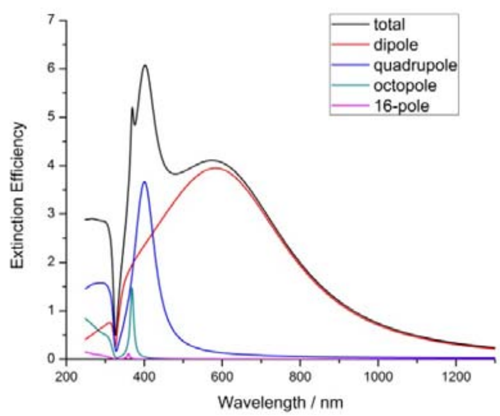

(e) R=100nm

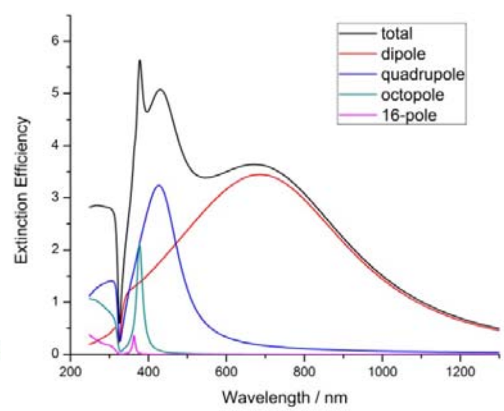

(f) R=120nm

Figure 4-1. Extinction efficiency spectra of silver nano-sphere with different radius in the air; the multi-poles arise in order.

The Mie theory is a series expansion of the electron movement and the particle size decides how many terms are involved. When the nano-sphere is small enough, i.e., the condition of the dipole approximation is satisfied, the motion of electrons only demonstrates a dipole-like resonance. When the particle size becomes larger, the multi-poles appear one by one and contribute to the total scattering, absorption and extinction. Figure 4-1 shows the extinction spectra of a silver sphere in the air; and with different radius, the figure shows that the higher-order poles arise in order.

Figure 4-1 demonstrates the appearance of multi-poles resonance as well as the change of the resonance peak and wavelength for a silver sphere in the air. As we can see, when the radius is smaller than 20nm, only the dipole resonance has a significant amplitude and the resonance wavelength is around 360~370nm. When the radius increases, the dipole resonance peak moves to longer wavelength and also becomes wider. At the same time, the quadrupole arises at the same wavelength position (around 360nm) and then reaches to its maximum with a slight red-shift; and then following the dipole peak, the quadrupole peak has a larger red-shift, shrinks and becomes wider. The higher-order octopole and 16-pole peaks have similar behaviours as the particle size increases. The total-extinction spectrum shows a multiple-peak curve, and each peak corresponds to one of the multi-poles resonances, with the lower-order resonance peaks locating at the longer wavelength side.

4.3.2 Size effects

The particle size has strong effects on the resonance peaks. The so-called *'extrinsic size effect'* refers to the macro-scope aspect which involves the size-dependent interference with the electromagnetic wave. The phase retardation of the wave by the particle can induce higher-order multipoles in it and cause the frequency shift, which are described by the higher-order terms in Mie's theory.

Figure 4-2 gives the extinction spectra of the single silver, gold or copper sphere with different radius in the air, respectively. Take the silver sphere as example, as the particle size increases, the dipole resonance gets stronger and then weaker; the resonance wavelength always moves to the red side and the peak width broadens. We can find a maximum resonance which corresponds to an optimized particle size around 30nm, and the resonance wavelength around 380nm (violet color).

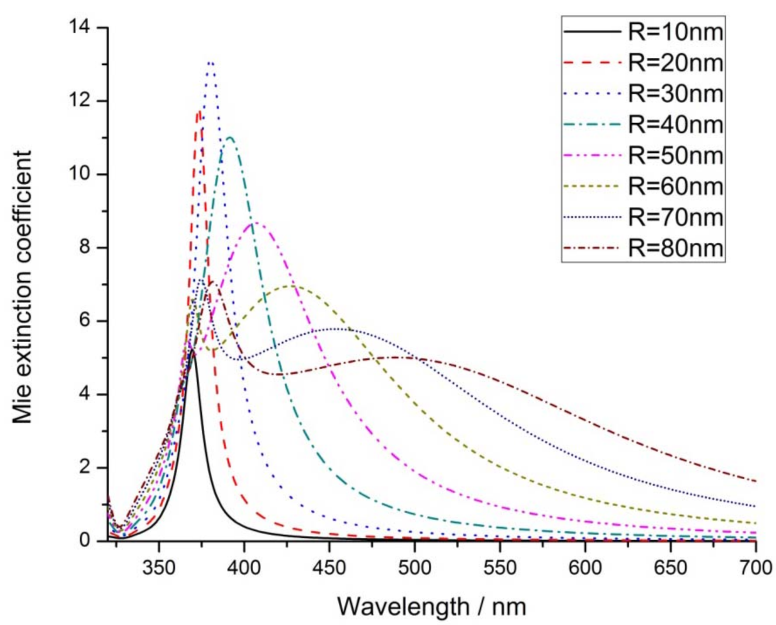

(a)

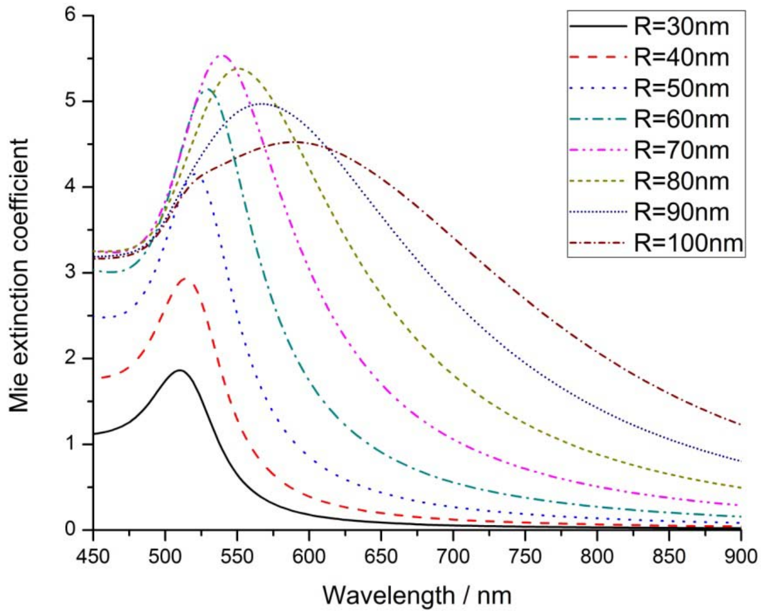

(b)

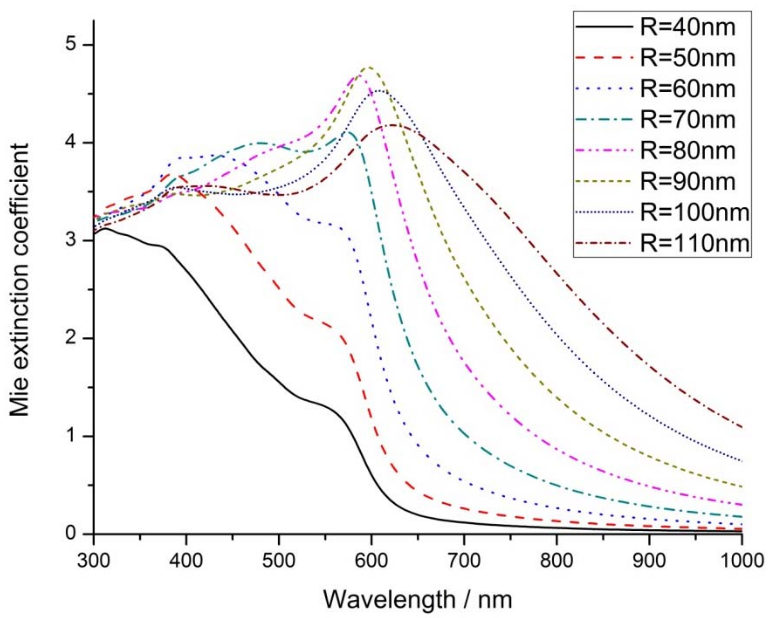

(c)

Figure 4-2. Extinction efficiency spectra of (a) silver; (b) gold; (c) copper nano-sphere with different radius in the air

Comparing to the silver sphere, the strong resonance of the gold sphere happens with larger size starting from 30nm, and also at longer wavelengths larger than 500nm (green color). The copper sphere has strong resonance at even larger size from 40nm, with wavelength larger than 550nm (yellow color). This is caused by the differences in the dielectric functions of the three noble metals.

For a silver sphere with the radius smaller than 10nm, the *'intrinsic size effects'* occurs, which refer to the quantum-mechanical ones when the particle size is much smaller than the light wavelength. Hopefully, these effects can be included in a size-dependent dielectric function of the metal. These effects and their impact on the resonance wavelength are summarized as follows.

1) The surface damping effect: red-shift

   When the particle size becomes close to or smaller than the mean free path of the conduction electron which is around 10nm, the so-called *surface damping effects* or *surface scattering-limited mean-free-path effect* appears. In this case, the mean free path of conduction electrons is reduced by the collision of the electrons with the particle surface. Thus the damping constant in Drude model increases and becomes size-dependent,

$$\Gamma = \Gamma_{\infty} + \frac{A v_F}{R} \tag{6}$$

   where v_F is the Fermi velocity and A is a model-dependent parameter. Similar models are well established in literatures [100-101, 107, 109-112].

This effect causes a red-shift of the resonance wavelength as the size decreases.

2) The ‘spill-out’ effect: red-shift

The definition of plasma frequency is expressed as $\omega_p = \left(ne^2 / \varepsilon_0 m_{eff} \right)^{1/2}$, where n is the electron density. For very small particles, the ‘spill-out’ of the free electrons on the particle surface induces the decreasing of the electron density; and the smaller the particle, relatively the more spill-out happens [113]. This effect also leads a red-shift of the resonance wavelength as the size decreases.

3) The lattice contraction effect: blue-shift

The stress on the surface of the particle causes the lattice contraction; and the contraction ratio is inverse proportional to the particle size. This also affects the electron density and then affects ω_p, but with the opposite way as the previous discussed spill-out effect. The result is a blue-shift of the resonance wavelength as the size decreases.

4) The effects on inter-band electrons: blue-shift

The above three effects are about the intra-band part of dielectric function $\varepsilon^s(\omega)$ which is due to *s*-electrons. The other part $\varepsilon^d(\omega)$ is generally regarded as size-independent. However, in fact, *d*-electrons have important influences on the resonance frequency especially for very small particles. When free electrons 'spill-out' of the surface, in the region near it, ineffective screening for core electrons appears. This leads to a relative small change of the dielectric constant of ε^d at the surface region. As the size decreases, this region has more influence on total ε^d and cause ε^d to decrease. Thus a blue-shift of the resonance wavelength appears.

The optical response of nano-particles can be measured individually by different methods [100, 107, 109-110, 112-116]. From these experimental results, we can find red-shifts of resonance energy as size decreases in most of them, while Cottancin and Lerme's groups report blue-shifts [107, 117], which also noticed by another group [113]. These 'blue-shifts' exist especially for particles smaller than 10nm and are interpreted mainly by the influence of *d*-electrons. The calculation method called *time-dependent local-density-approximation (TDLDA)* [107, 114, 117-124] successfully describes these blue-shifts.

4.4 Move to longer wavelength

From above calculations, the LSPP of noble metal particles generally happens in the range of 300~600nm. For the potential applications in optical communications, we would like to get the resonance at longer wavelengths, such as 1310nm or 1550nm.

Considering the quasi-static region, i.e., that the size is less than 20nm, under the quasi-static approximation or dipolar approximation and from Mie's theory, the dynamical polarizability of the spherical particle is [105],

$$\alpha(\omega) = \frac{\varepsilon(\omega) - \varepsilon_m}{\varepsilon(\omega) + 2\varepsilon_m} \varepsilon_m R^3 \tag{4.36}$$

where R represents the radius of particle, and ε_m the dielectric constant of the matrix. The absorption cross-section is [105],

$$\sigma(\omega) = \frac{4\pi\omega}{c\varepsilon_m^{1/2}} \mathrm{Im}[\alpha(\omega)] \tag{4.37}$$

Therefore, the resonance frequency ω_s is approximately determined by,

$$\mathrm{Re}\left(\varepsilon(\omega_s)\right) = -2\varepsilon_m \tag{4.38}$$

For noble metals, in the light wave region, $\mathrm{Re}\left(\varepsilon(\omega)\right)$ is negative and has a positive slope with frequency. If the surrounding media has a higher dielectric constant ε_m, ω_s decreases (red-shift), which means a longer resonance wavelength.

Moreover, if we can decrease the real part of the metal's dielectric function, with the same ε_m, the resonance wavelength also moves to the longer side.

The other way is to change the particle shape to ellipsoid or nano-rod. With these shapes, the dipole approximation is easier to sustain for larger size (the long axis), and as we know, with larger size the resonance wavelength also becomes longer.

4.4.1 Change the surrounding material

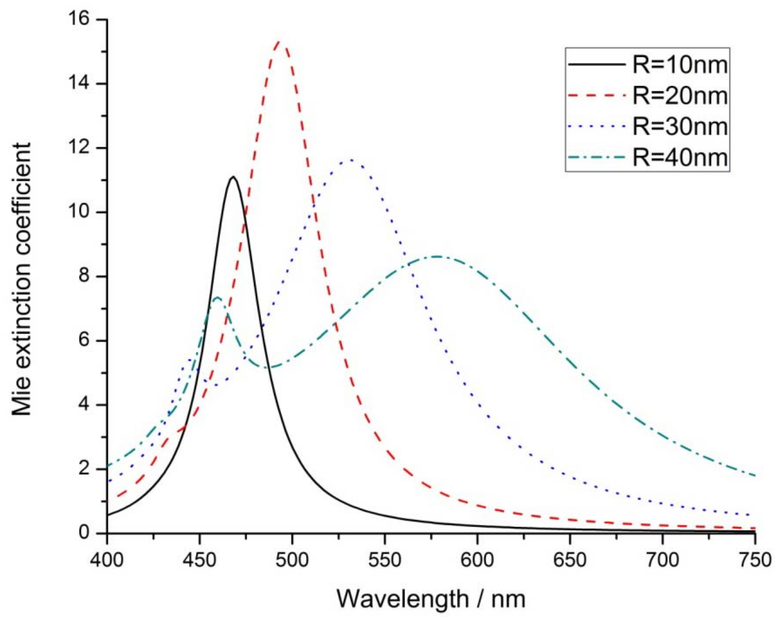

Figure 4-3. Extinction efficiency spectra of silver nano-sphere with different radius in the aluminia (ε = 3.2)

As discussed before, using a surrounding material with larger dielectric constant ε_m will induce a longer resonance wavelength. Figure 4-3 gives the extinction efficiency spectra of silver nano-sphere in the aluminia, whose dielectric constant is 3.2, and the dipole resonance peaks for radius 10nm, 20nm, 30nm and 40nm locate at 468nm, 494nm, 530nm and 578nm, respectively. This provides a comparison to Figure 4-2(a), which shows the extinction efficiency of silver nano-sphere in the air, and the resonance peak for the same radii are at 370~400nm.

4.4.2 Tungsten nano-spheres

After a survey of various suitable metals, we find that, comparing to the three noble metals, tungsten has smaller real parts of dielectric function in the light wave region, which means it is more likely to have resonance in longer wavelength.

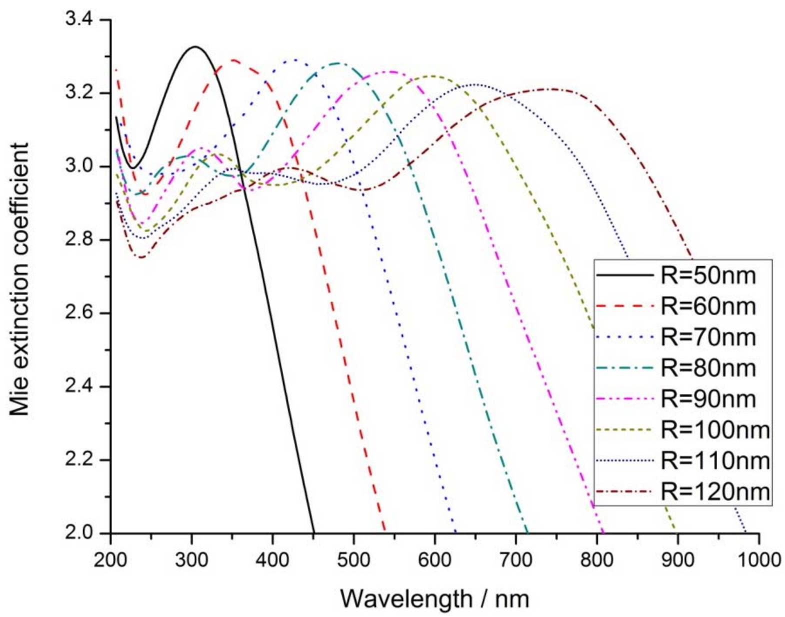

Figure 4-4. Extinction efficiency spectra of Tungsten nano-sphere with different radius in the air

Figure 4-4 shows the extinction efficiency spectra of single tungsten nano-sphere with different radius in the air. The dipole resonance is dominant in all shown curves, with radius from 50nm to 120nm, and the resonance wavelength covers a much wider range from 300nm to 800nm. The short come of the tungsten particle is that, because of relatively stronger absorption, the resonance peak is not as sharp as those of the noble metal particles.

4.4.3 Change the shape to the ellipsoid or nano-rod

For the nano-rod or the ellipsoid, especially the cigar-shaped prolate spheroid, when the incident light is polarized along the long axis of the particle, we can apply the dipole approximation for the calculation. The equations are listed in section 4.2.4.

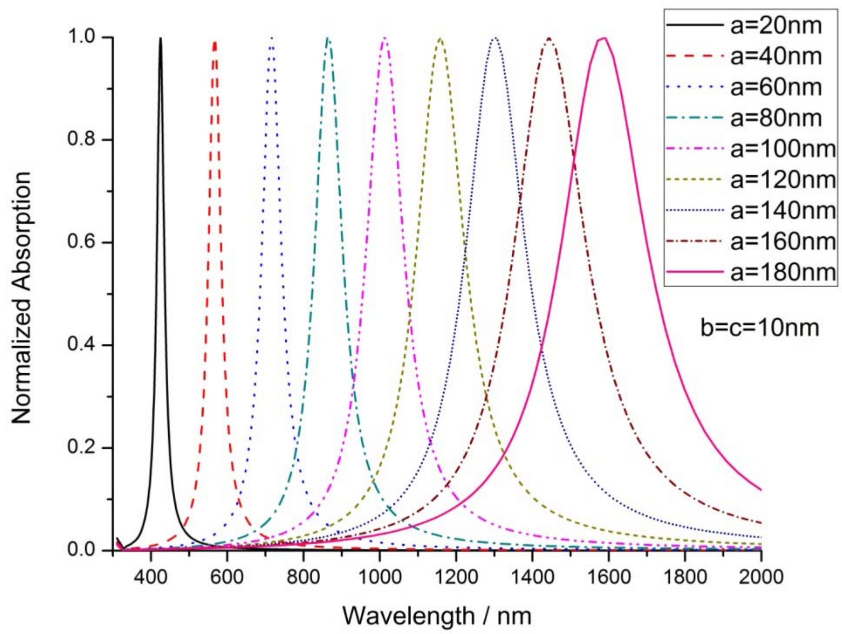

Figure 4-5. Normalized absorption spectra of silver prolate spheroid in the air; a is the long axis, b and c are the two short axis.

As an example, Figure 4-5 gives the normalized absorption spectra of a silver prolate spheroid. When increasing the long axis from 20nm to 180nm, the absorption peak moves from 424nm to 1580nm. The peak also becomes wider at longer wavelengths.

4.5 Artificial imaginary part for a narrow resonance peak

From the above results, we find that the FWHM of the resonance peak of noble-metal particles generally ranges from dozens of nanometers to several hundreds of nanometers. This peak width is caused by the strong absorption of the metal to the light wave, which is represented by the imaginary part of dielectric function. Therefore, the resonance peak can be sharper by reducing the absorption of the metal particle.

By eliminating the imaginary part of the metal's dielectric function, we can see the resonance peak becomes sharper and sharper as shown in Figure 4-6. The FWHM of the extinction peak is 35nm with the original value of the imaginary part, and it becomes 19.5nm when the imaginary part is reduced to a half of the original value, and 11.7nm when reduced to one fourth, and 6.9 nm when reduced to one tenth, and 4.0nm when reduced to one percent. At the same time, the absorption peak (the red one) shrinks and the scattering becomes the major part of the extinction.

A narrow resonance peak is meaningful for the application of these particles in the aspect of better spectrum selectivity and higher nonlinearity. The calculation results show that the peak can be narrowed by suppressing the imaginary part of the dielectric function of the metal material. To achieve that, possible implementation methods include cooling down the particle or constructing super-lattice during the fabrication.

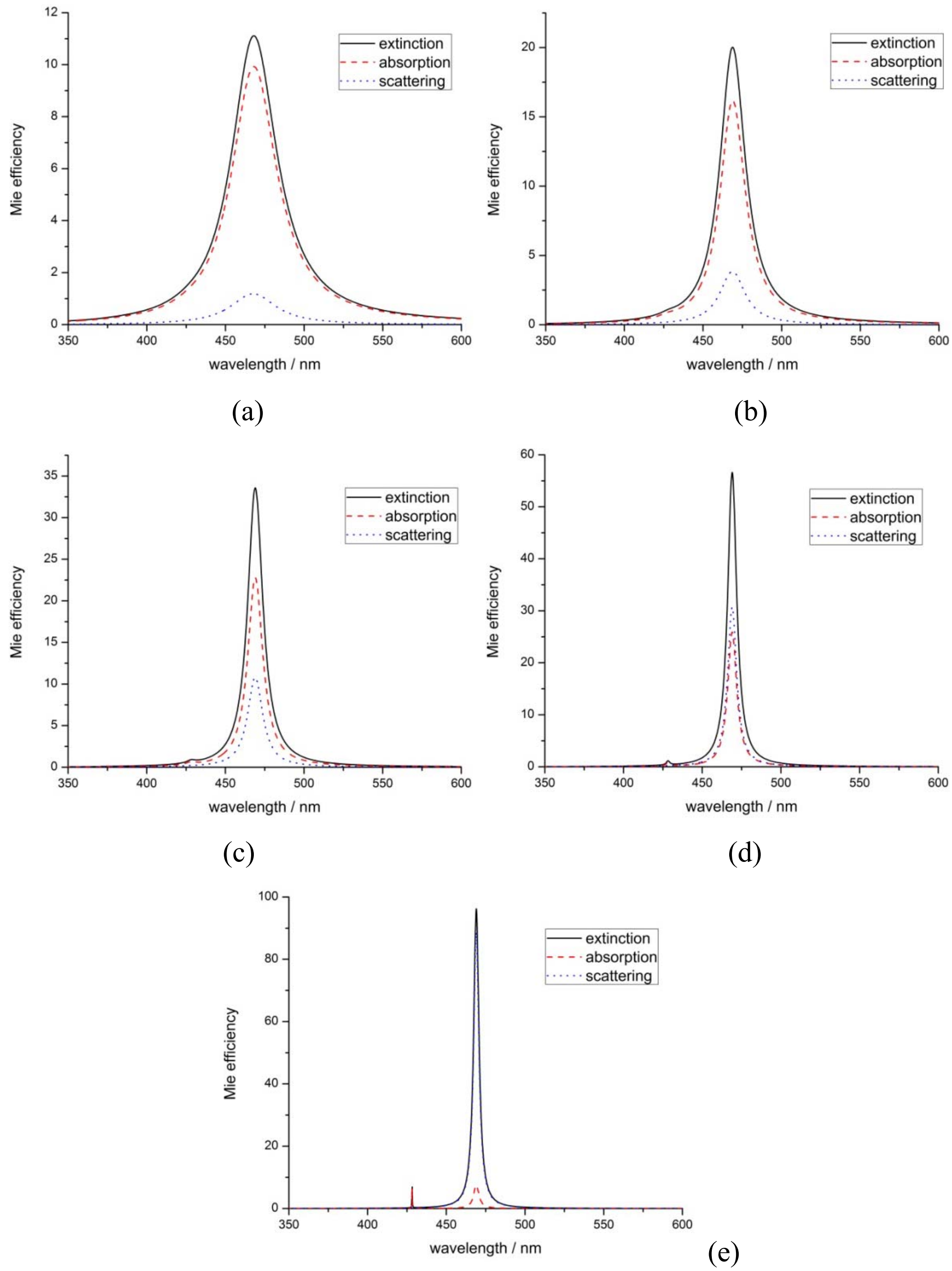

Figure 4-6. The extinction, absorption and scattering spectra of a silver nano-sphere in the air; the imaginary part of the metal's dielectric function is multiplied by a factor of (a) 1; (b) 0.5; (c) 0.25; (d) 0.1; (e) 0.01.

4.6 Summary

In this chapter, the LSPP of the metal nano-particle is calculated by Mie theory. By changing the particle size, the generation of multi-poles and the size effects on the resonance peak width and wavelength are discussed. For the purpose of moving the resonance peak to a longer wavelength, several possible methods are testified, including using a surrounding material with higher refractive index; changing the particle material to tungsten; and changing the particle shape to the ellipsoid shape. Calculation results show that the resonance wavelength moves to the longer side in all of the three situations. These methods can also been used in combination and achieve the resonance wavelengths for specified applications.

As for the peak width, the resonance peak of the ellipsoidal particle has a narrower width compared with that of a spherical particle; and the simulation results also confirm that if the absorption of metal material can be suppressed, the resonance peak can have a much narrower width and achieve a high Q-factor. To reduce the absorption, possible implementation methods including cooling down the particle or constructing super-lattice during the fabrication can be further investigated.

This research suggests further developments of the metal nano-particle for the applications in many disciplines where the suitable wavelength and Q-factor is required, including the design of the novel nano-photonic devices for optical communications.

Chapter 5
Metal Nano-structure: Distributed Bragg Reflector (DBR) Laser Design with Metal Nano-strip Grating

5.1 Introduction

The Distributed Bragg reflector (DBR) laser is a competitive candidate for applications in optical telecommunication networks because of its simple design and fabrication, and the performance merits such as the single-mode operation, the narrow linewidth and the wavelength tunableness [125]. The schematic structure of a simple ridge-waveguide DBR laser is shown in Figure 5-1.

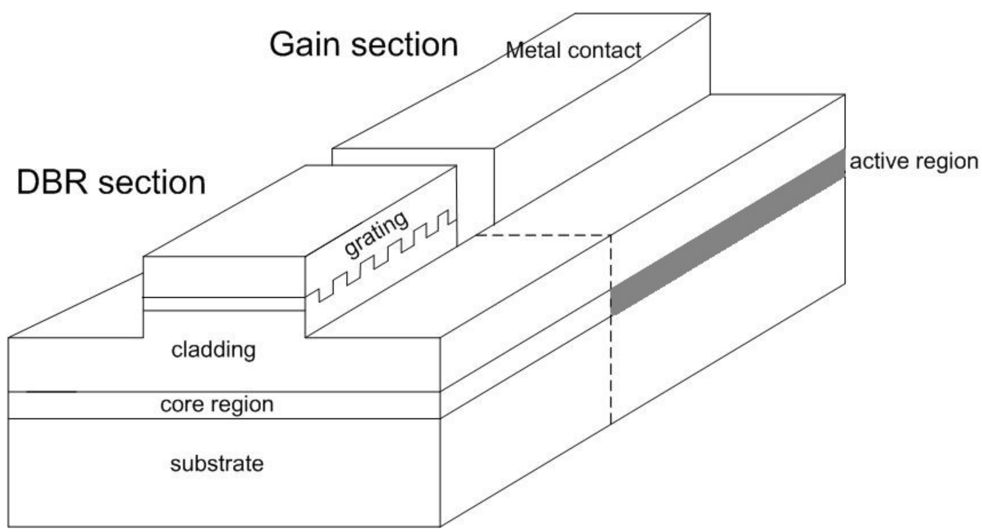

Figure 5-1. Schematic structure of the DBR laser

In a conventional DBR laser, the Bragg grating is a refractive-index grating made of slightly different semiconductor materials. Here we propose a novel Bragg grating design using periodically buried metallic nano-strips. By replacing the semiconductor grating by the metallic nano-structure grating, because of the large difference of the metal and the semiconductor's refractive index, it is easier to achieve a high reflectivity with small structures. Moreover, the coupling constant can be tuned in a wide range by simply changing the design parameters of the nano-structure. Due to the development of nano-scale fabrication techniques, this metallic nano-structure now is easier to fabricate.

In this work, the metal grating is investigated by the mode matching method (MMM) and the coupled-wave theory (CWT). The results from these two methods are compared. Simulation results shows that the metal grating can achieve a wide range of κL by simply changing the design parameters, such as the spacing of the grating and the core region, the thickness of nano-strips and the duty cycle. Further, for the simulation of the laser output, the multi-mode rate equation model is applied. The results confirm the single-mode operation for the designed parameters of the metal grating.

This chapter is organized as follows. In section 5.2, the metal grating which constitutes the DBR region is theoretically simulated and discussed by the two methods and the influence of the design parameters on the reflection spectrum is investigated. Then in section 5.3 the laser output with the designed metal grating is simulated by the rate-equation model. And the output power and SMSR under different parameters of the metal grating are studied.

5.2 DBR section based on the metal nano-strip grating

The structure of the DBR region is shown in Figure 5-2. The metal strips (Au) are buried in the cladding region, with spacing to the core region denoted by *D*. The grating period is Λ and the duty cycle is a/Λ . The refractive index of gold is 0.5183-9.0707i for wavelength of 1310nm. And the refractive index is 3.25 for the core region which is made of InGaAsP, and 3.1 for the substrate and cladding which are made of InP. The thickness of the core region is fixed as 0.2μm and the thickness of the gold strips is 50nm. The grating period is tuned to make that the Bragg wavelength equals to 1310nm, which is also the reference wavelength of the laser output.

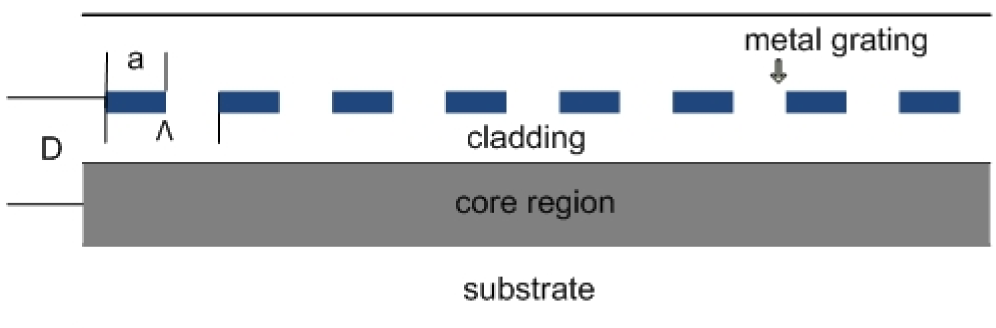

Figure 5-2. Sectional view of the DBR region

5.2.1 Coupled-wave theory (CWT)

The grating is a periodic perturbation of the refractive index or dielectric constant. Because of the spacing from the grating to the core region, the perturbation to the cavity optical mode is relatively weak. This condition will be reviewed by comparing the transverse main-mode pattern in the grating subsections, one with the metal and the other one without the metal. With this condition verified, the coupled-wave theory is suitable to describe the interaction of the forward wave and the reflected backward wave, although the accuracy may be degraded when the grating moves closer to the active region.

The transverse mode patterns are calculated by the mode solver. We use the high-order finite-difference method [126] with the perfectly matched layer (PML) [127] to solve for the main mode (see Appendix A). The patterns are shown in Figure 5-3 for the case $D = 0.6\mu m$.

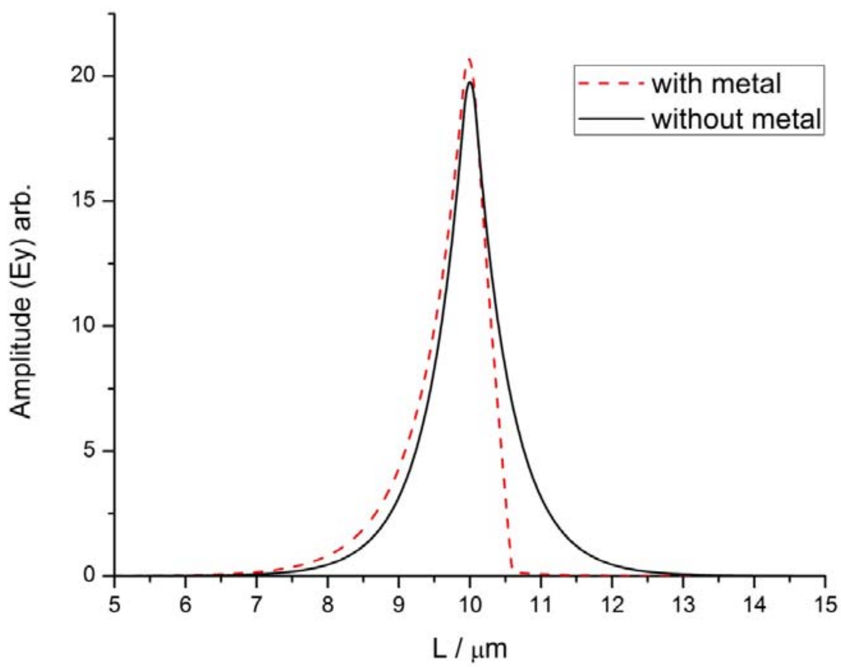

Figure 5-3. Field pattern of the main mode, red line: with metal;

blue line: without metal; λ=1310nm

In Figure 5-3, the black line shows the main mode pattern without metal, which is symmetric, with its power restricted in the core region and exponentially decaying in the cladding and substrate region; the red line shows the mode pattern with the metal strip, because that the electrical field in the metal is nearly zero, the pattern is changed on one side. The difference between the two mode patterns is mainly in the cladding region where the modal power is limited. Therefore, we can consider that the metal strip only has a weak perturbation to the main mode, and then the coupled-wave theory can be applied.

Figure 5-4 shows the dielectric constant perturbation in the grating area. $\Delta\varepsilon$ is the dielectric constant difference between the metal and the surrounding semiconductor material in the cladding. In the grating region, along z-direction (the propagation direction), this perturbation is ideally a square wave. With the periodicity, the perturbation can be decomposed into a Fourier series and each term represents a sinusoidal perturbation with the corresponding order. For example, if ε_1 denotes the first-order Fourier series coefficient, it also indicates the amplitude of the first-order of perturbation. When duty cycle is 50%, we get that $\varepsilon_1 = \Delta\varepsilon/\pi$.

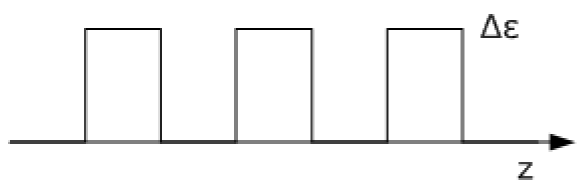

Figure 5-4. Perturbation of the dielectric constant along *z*-direction

From the coupled-wave theory, the coupling coefficient for the first-order grating is given as (see Appendix B),

$$\kappa = \frac{\omega}{4}\int \phi \cdot \varepsilon_1 \phi dxdy \tag{5.1}$$

where ω denotes the angular velocity and Φ the transverse mode pattern. In our case, in the grating area, $\Delta\varepsilon = \left(n_{metal}\right)^2 - \left(n_{cladding}\right)^2$. The coupling coefficient is,

$$\kappa = \frac{\omega\varepsilon_0}{4\pi}\left(\left(n_{metal}\right)^2 - \left(n_{cladding}\right)^2\right)\int_{grating\ area} \phi_{without\_metal}\phi_{with\_metal} dxdy \tag{5.2}$$

where n_{metal} and $n_{cladding}$ represents the refractive index of the metal and the cladding material, respectively; and $\phi_{without\_metal}$ and ϕ_{with_metal} represents the transverse mode pattern of the main mode, with the metal and without the metal, respectively, and are calculated by the mode solver.

With the coupling constant, we can deduct the reflectivity and transmission for the grating with arbitrary length L from the coupled-wave theory (see Appendix B). Use A and B to represent the forward and backward field amplitudes, respectively, and with the given condition that $B(L) = 0$, the reflectivity R and transmission T with regard to the field amplitude are [128],

$$R = \frac{B(0)}{A(0)} = \frac{-i\kappa \sinh SL}{S\cosh SL + i(\Delta\beta + i\gamma)\sinh SL} \tag{5.3}$$

$$T = \frac{A(L)}{A(0)} = e^{i\Delta\tilde{\beta}L}\frac{S}{S\cosh\left(SL\right) + i(\Delta\beta + i\gamma)\sinh\left(SL\right)} \tag{5.4}$$

where,

$$S = \sqrt{\kappa^2 - \Delta\tilde{\beta}^2} = \sqrt{\kappa^2 - \left(\Delta\beta + i\gamma\right)^2} \tag{5.5}$$

and $\Delta\beta = \beta - \frac{\pi}{\Lambda}$ corresponding to the detuning of the working wavelength to the Bragg wavelength; $\tilde{\beta}$ represents the complex modal propagation constant,

$$\begin{aligned} \tilde{\beta} &= \beta + i\gamma = n_{eff} k_0 \\ \beta &= \mathrm{Re}\left(n_{eff}\right) \cdot k_0 \\ \gamma &= \mathrm{Im}\left(n_{eff}\right) \cdot k_0 \end{aligned} \tag{5.6}$$

And the power reflectivity and power transmission are calculated by $|R|^2$ and $|T|^2$, respectively.

5.2.2 Mode matching method (MMM)

While the coupled mode theory considers only the forward and backward fundamental mode, the mode matching method involves a number of modes which are possibly significant in the waveguide structure, thus the MMM has better accuracy. At the same time, it generally has no analytical solution and requires more calculation.

The scheme of the MMM is as follows. Firstly the modes are solved by the high-order finite-difference method at each different sub-section. With the modal patterns all known, it is only needed to find the modal amplitudes. The output modal amplitudes is connected with the given input modal amplitudes through the scattering matrix. And the total scattering matrix of the structure is found by cascading the scattering matrix from the input port to the output port. At the waveguide discontinuities, the scattering matrix is obtained by matching the modal amplitudes and utilizing the boundary condition (the continuity of the tangential electric and magnetic fields) and the orthogonality of the modes (see Appendix C).

For the DBR grating, the structure is periodic, thus the total scattering matrix can be easily found by repeatedly cascading the scattering matrix of one period. Assume the input is the fundamental mode from the gain section of the laser, and from the scattering matrix we can calculate the reflected and transmitted light beams which both are composed of the multiple modes.

5.2.3 Comparison of the results from the two methods

To compare the accuracy of CWT and MMM, first we run simulation by the two methods for the case that the spacing of the grating and core region *D* equals 0.6μm; the grating length (also the length of the DBR section) *L* equals 200μm. The power reflectivity spectrum is shown in Figure 5-5.

The MMM uses over 80 modes including the radiation modes and is regarded more accurate. The CWT only considers the main mode with forward and backward propagation directions, thus the coupling from the main mode to the radiation modes is neglected. As shown in Figure 5-5, because of this reason, the power reflectivity around the peak is higher than results from the MMM.

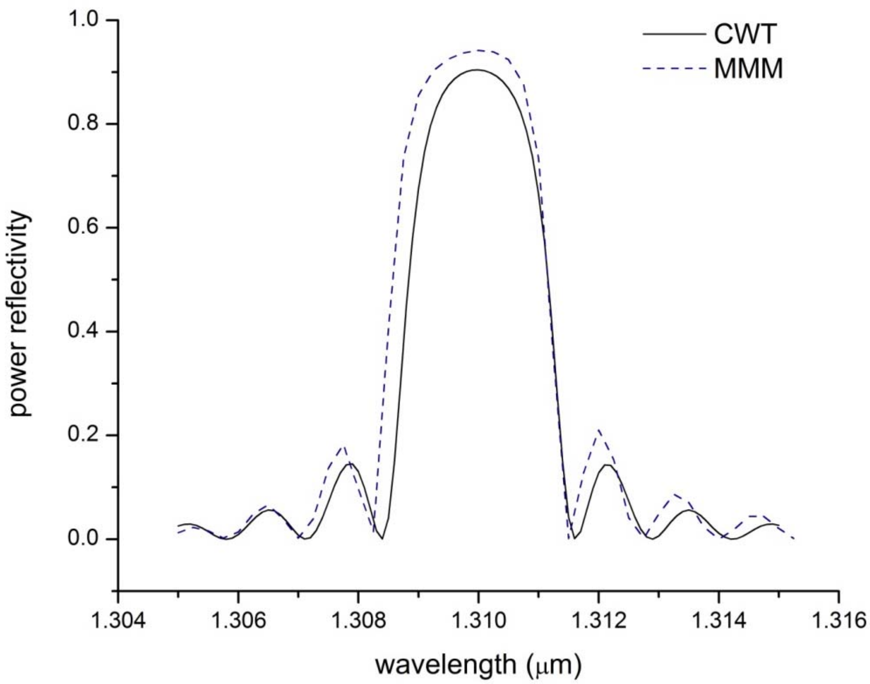

Figure 5-5. Comparison of the power reflectivity spectrum calculated by coupled-wave theory (CWT) and mode-matching method (MMM); D=0.6μm; L=200μm

Figure 5-6 demonstrates the difference of the peak values from the two methods when varying the grating length. The top two curves are for the case that *D* equals 0.6μm; the bottom two curves are for that *D* equals 0.8μm, which means the perturbation is weaker thus we can see the values are closer, and also the difference is smaller for a shorter grating length. Generally the CWT is more accurate for weak perturbation and short grating length because the coupling to radiation modes is less. However, from the top two curves that *D* equals 0.6μm, for longer grating length because the peak reflectivity is close to 1, the difference is even smaller.

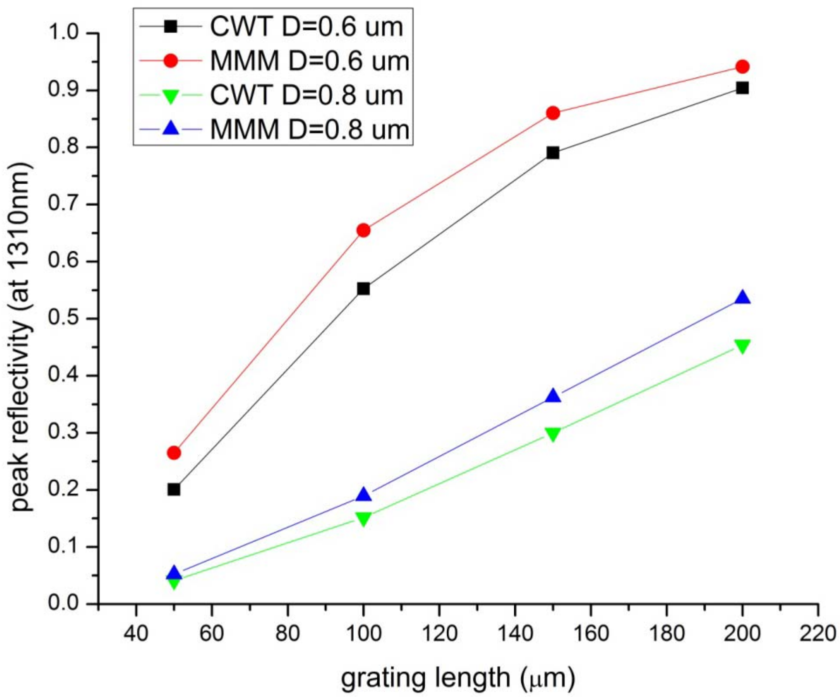

Figure 5-6. Comparison of the peak reflectivity calculated by coupled-wave theory (CWT) and mode-matching method (MMM); D=0.6μm

5.2.4 Design of the DBR region

The DBR region is to reflect the selected longitudinal mode back to the gain region, thus we need a narrow bandwidth and a high main-mode reflectivity. Because the material is chosen to be gold and the metal strip thickness is also fixed to be 50nm for the convenience of fabrication, the structural parameters we can design for the grating are, 1) the spacing between the grating and the core region *D*; 2) the grating length *L*; 3) the duty cycle a/Λ .

The spacing *D* decides the strength of the coupling between the forward and backward waves; the smaller the spacing *D* is, the stronger the coupling is. Table 5-1 gives the coupling constant and the effective index of the main mode when varying the spacing *D*. Figure 5-7 shows the real part and imaginary part of the coupling constant when the spacing *D* changes from 0.35μm to 0.8μm.

spacing	n_{eff} (with metal)	Kappa (1/cm)
D = 0.4 μm	3.109398 + i* 9.079969e-5	- 225.719 + i* 1.121
D = 0.5 μm	3.115515 + i* 5.991596e-5	- 149.224 + i* 0.529
D = 0.6 μm	3.119408 + i* 3.726416e-5	- 96.919 + i* 0.3291
D = 0.7 μm	3.121828 + i* 2.322021e-5	- 63.016+ i* 0.206
D = 0.8 μm	3.123346 + i* 1.466778e-5	- 41.255 + i* 0.130

Table 5-1. Modal index and coupling constant when varying the spacing between the grating and the core region

The coupling constant has a large real part and a small imaginary part, because it is proportional to the difference of the dielectric constants of the metal and the cladding material, due to the equation (5.2).

As shown in Figure 5-7, the real part of the coupling constant is proportional to the spacing *D* and reaches a large range when varying the spacing *D*. It has a small absolute value of less than $50cm^{-1}$ when the spacing is 0.8μm; and larger than $250cm^{-1}$ when the spacing is 0.35μm.

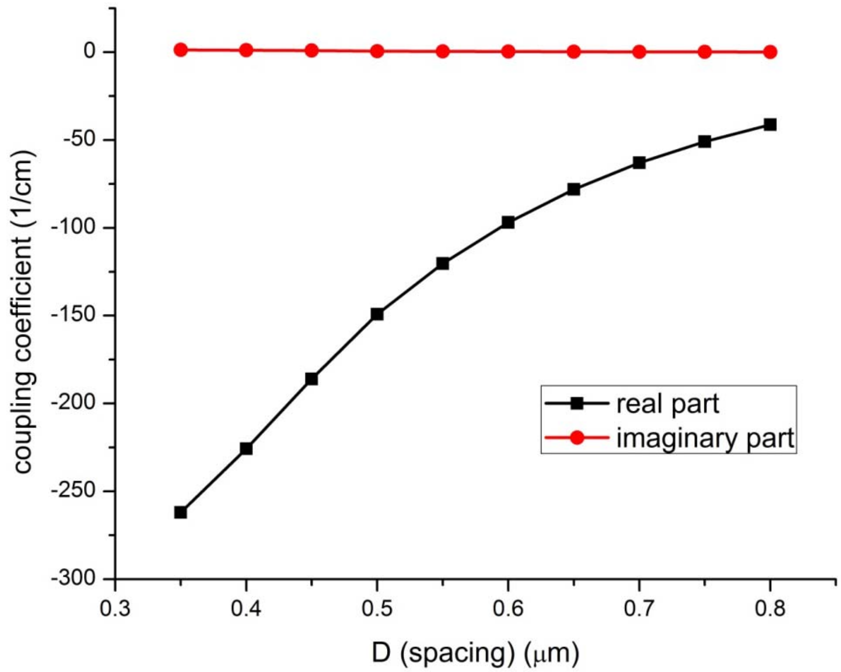

Figure 5-7. Coupling constant when varying the spacing of the grating and core region

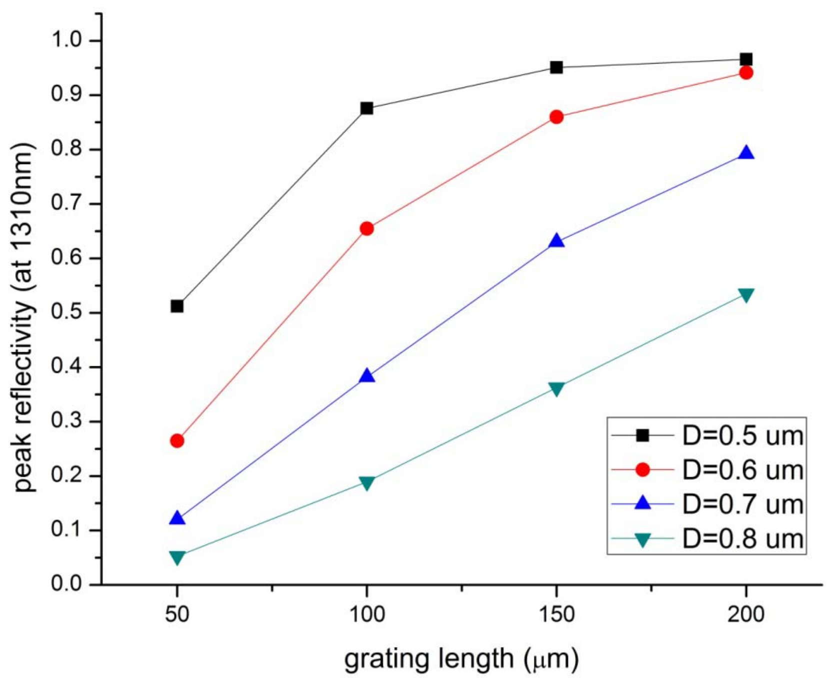

Figure 5-8. Dependence of peak reflectivity on grating length and spacing

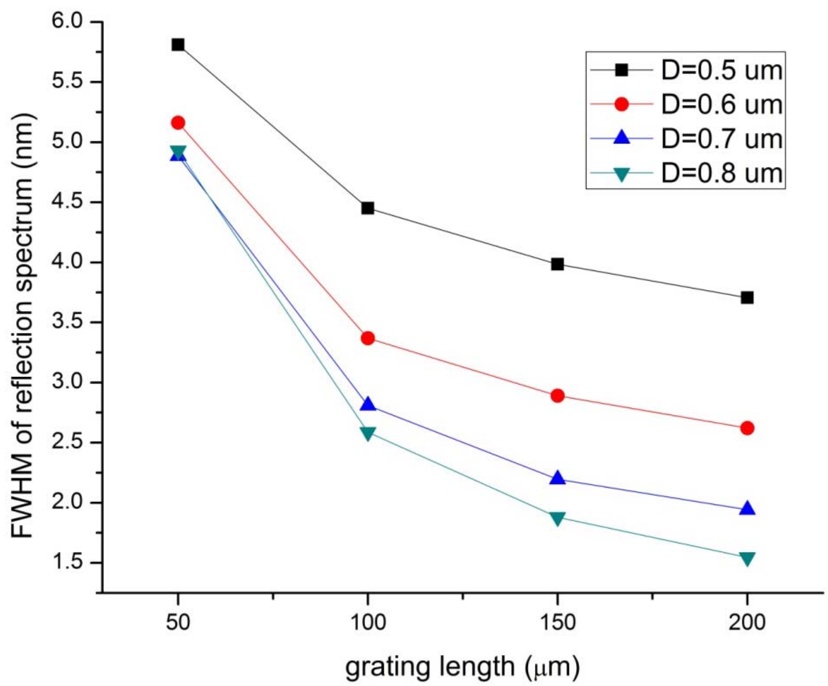

Figure 5-9. Dependence of FWHM of reflection spectrum on grating length and spacing

If the real part of the coupling constant has a larger absolute value, it is easier to get a high peak-reflectivity with relatively shorter grating length; if it has a smaller absolute value, a narrower output bandwidth can be obtained with a longer grating length. From Figure 5-8 and Figure 5-9 we can see this. In these two figures the peak reflectivity and the full-width half-maximum (FWHM) of the reflection spectrum when varying the grating length and the spacing are demonstrated, respectively.

Therefore, for the DBR region, we need the coupling constant in between to get both a narrow bandwidth and a high peak-reflectivity. For example, from Figure 5-8 and Figure 5-9, when the spacing D is 0.6μm, which means the real part of the coupling constant is 96.9cm^{-1}, and the grating length is 200μm, the peak reflectivity reaches 0.94

and the bandwidth is 2.62nm. Thus a single longitudinal-mode can be selected and the peak reflectivity also satisfied the requirement of a DBR laser.

As for the duty cycle, 50% should be the best because the first-order coefficient reaches its maximum and the coupling is the strongest. When the spacing *D* is 0.6μm and the grating length is 200μm, Figure 5-10 gives the power reflection spectrum when varying the duty cycle; Figure 5-11 shows the peak reflectivity and the FWHM of the reflection spectrum with different values of the duty cycle. As shown in these two figures, the power reflection drops when the duty cycle is away from 50%. Although we can get a smaller FWHM, the peak reflectivity drops too much that we cannot endure the power loss, thus we still remain at a 50% duty cycle.

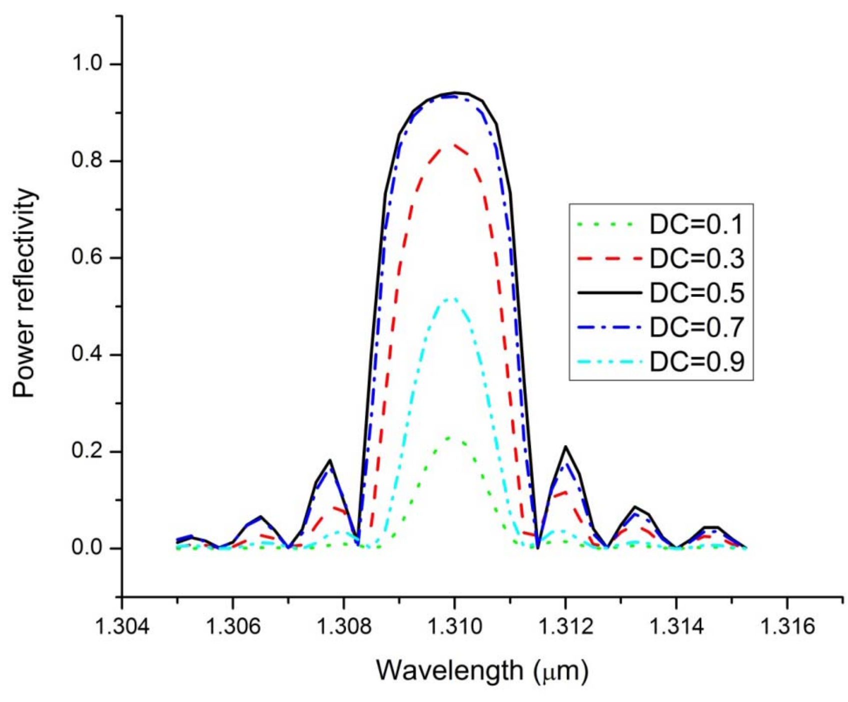

Figure 5-10. Power reflection spectrum when varying the duty cycle

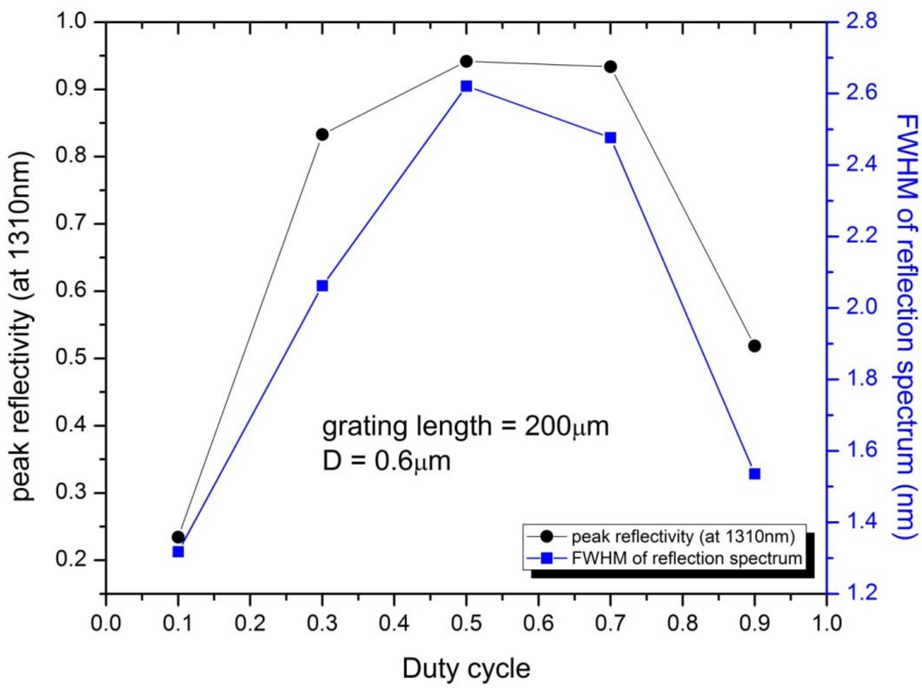

Figure 5-11. Dependence of the peak reflectivity and FWHM on the duty cycle

5.3 Design of the DBR laser

In this section the output of the DBR laser is simulated using a multi-mode rate equation model. For the design parameters of the metal grating, the duty cycle is fixed to be 50%, and the spacing D of 0.6μm, 0.7μm and 0.8μm are testified. The main mode is at 1310nm with designed grating period.

To compare the mode selectivity, the mode spacing is also fixed. For the DBR laser, the mode spacing is,

$$\Delta\lambda = \frac{\lambda^2}{2n_{eff}L_{total}} \tag{5.7}$$

where λ denotes the working wavelength, n_{eff} represents the effective modal index of the main mode in the gain section, and the total cavity length L_{total} has two parts,

$$L_{total} = L_A + L_{Geff} \tag{5.8}$$

where L_A denotes the length of the gain section and L_{Geff} the effective penetration length of the grating,

$$L_{Geff} = \frac{\tanh(\kappa L_G)}{2\kappa} \tag{5.9}$$

and L_G is the grating length.

The coupling constant and the effective penetration length are listed in Table 5-2 for different spacing *D* and grating length.

To make sure the mode spacing is the same for different spacing *D* and grating length, we fix the total cavity length L_{total} to be 300μm. This means that the active region has different length while the penetration length is different. For example, with the grating length L_G equals 200μm, we use a longer active region for the spacing *D* equals 0.6μm than that *D* equals 0.8μm.

Table 5-2. The effective penetration length of the grating

Spacing	Kappa (1/cm)	L_{Geff} when L_G=100μm	L_{Geff} when L_G=200μm
D = 0.6 μm	- 96.919 + i* 0.3291	38.6068	49.49501
D = 0.7 μm	- 63.016+ i* 0.206	44.28738	67.53474
D = 0.8 μm	- 41.255 + i* 0.130	47.34403	82.15193

5.3.1 Multi-mode rate equation model

The multi-mode rate equation model is represented by the rate equations for the photon number in each longitudinal mode and the carrier density [129-134],

$$\begin{aligned}\frac{dS_m}{dt} &= g_m\left(N, S_1 \cdots S_M\right) S_m - \frac{S_m}{\tau_{pm}} + \Gamma \beta V_{act} B_{eff} N^2 \\ \frac{dN}{dt} &= \frac{I(t)}{qV_{act}} - \frac{1}{V_{act}} \sum_{m=1}^{M} g_m\left(N, S_1 \cdots S_M\right) S_m - B_{eff} N^2\end{aligned} \tag{5.10}$$

where M modes are considered; S_m represents the photon number in *m-th* mode, N the carrier density in the active region, V_{act} the volume of the active region, Γ the confinement factor of the main mode calculated from the mode solver, β the spontaneous emission coefficient, B_{eff} the effective recombination rate, τ_{pm} the photon lifetime for the *m-th* mode, q the electron charge and $I(t)$ the real-time injection current. $g_m\left(N, S_1 \cdots S_M\right)$ represents the gain for the *m-th* mode and it contains the linear gain and the nonlinear gain,

$$g_m\left(N, S_1 \cdots S_M\right) = A_m - B_m S_m \tag{5.11}$$

The linear gain has a parabolic spectral dependence near the gain peak,

$$A_m = \Gamma a\left[N - N_0 - b\left(\lambda_m - \lambda_{peak}\right)^2\right] \tag{5.12}$$

where a denotes the differential gain, N_0 the transparency carrier density, b the gain broadening factor, λ_m the wavelength of the *m-th* mode and λ_{peak} the wavelength of the gain peak.

And the nonlinear gain coefficient is defined as,

$$B_m = B_c\left(N - N_S\right) \tag{5.13}$$

where B_c denotes the self-saturation factor and N_S the nonlinear gain transparency carrier density.

The photon lifetime is,

$$\tau_{pm}^{-1} = \frac{c}{n_{eff}}\left[\alpha_i + \frac{1}{2L_{total}}\ln\left(\frac{1}{R_1 R_m}\right)\right] \tag{5.14}$$

where c denotes the light velocity in vacuum, n_{eff} the effective modal index, α_i the internal loss, R_m the power reflectivity from the DBR section for the *m-th* mode and R_1 the power reflectivity from the facet on the other end.

And the output power of the *m-th* mode emitted from the facet with power reflectivity R_1 is,

$$I_m = S_m \frac{hc}{\lambda_m}\left(1 - R_1\right)\frac{1}{\Gamma\tau_{pm}} \tag{5.15}$$

The values of the parameters used in the simulation are listed in Table 5-3.

Table 5-3. DBR laser parameters [130]

Parameters	**Values**
cavity total length L_{total}	300 μm
internal loss α_i	10 cm^{-1}
facet reflectivity R_1	0.32
confinement factor Γ	0.3056
effective modal index n_{eff}	3.126
reference lasing wavelength λ_{peak}	1310 nm
differential gain a	$1.62\times10^{-12}\ m^3/s$
transparency carrier density N_0	$1.2\times10^{24}\ m^{-3}$
Nonlinear gain transparency carrier density N_S	$1\times10^{24}\ m^{-3}$
spontaneous emission coefficient β	5×10^{-5}
effective recombination rate B_{eff}	$3\times10^{-16}\ m^3/s$
self-saturation factor B_c	$2\times10^{-20}\ m^3/s$
gain broadening factor b	$9\times10^{20}\ m^{-3}nm^{-2}$

5.3.2 Simulation results

In the simulation, the power spectra of the grating obtained from the MMM method is used to determine the power reflectivity for each longitudinal mode; the coupling constant obtained from the CWT is used to calculate the penetration length. The total effective cavity length is fixed to be 300μm, thus the wavelength spacing for the longitudinal modes is also fixed. Then the rate-equation model is solved by the Runge-Kutta method.

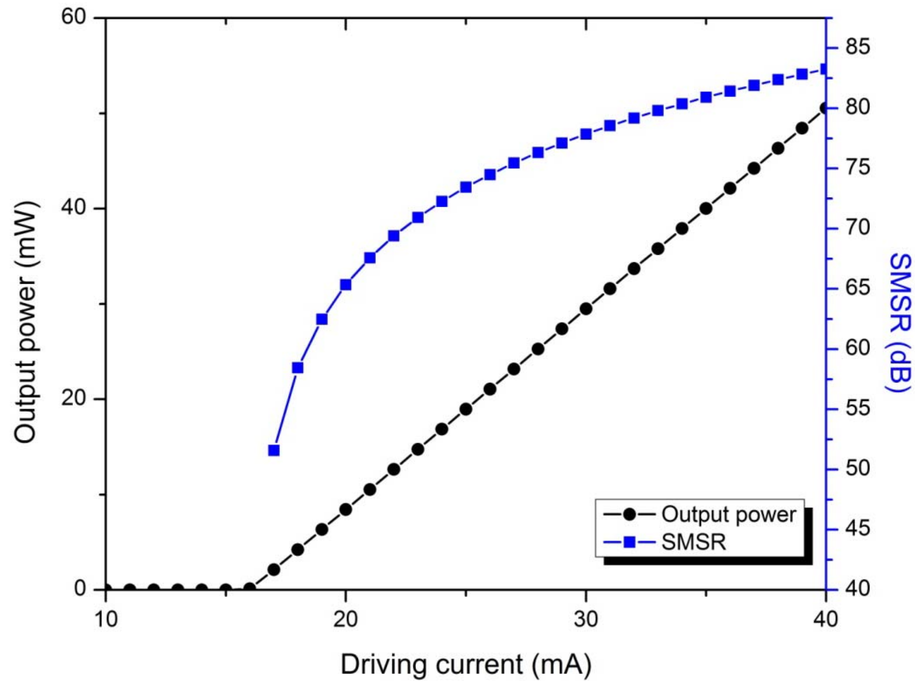

Figure 5-12. Output power and SMSR of the DBR laser when $D=0.6\mu m$ and the grating length is $150\mu m$

When the spacing of the grating to the core region *D* equals 0.6μm and the grating length is 150μm, Figure 5-12 shows the laser output power and the SMSR when varying the driving current. The threshold current is around 16mA. Above the threshold current, the laser is under single-mode operation and the SMSR reaches 50dB and higher.

Figure 5-13 and Figure 5-14 demonstrate the output power and the SMSR of the DBR laser when varying the spacing *D* and the grating length under driving current of 40mA. For the spacing *D* of 0.6μm, 0.7μm and 0.8μm, respectively, and the grating length from 100μm to 200μm, the laser output is simulated. The single longitudinal mode is selected in all cases with a SMSR over 75dB.

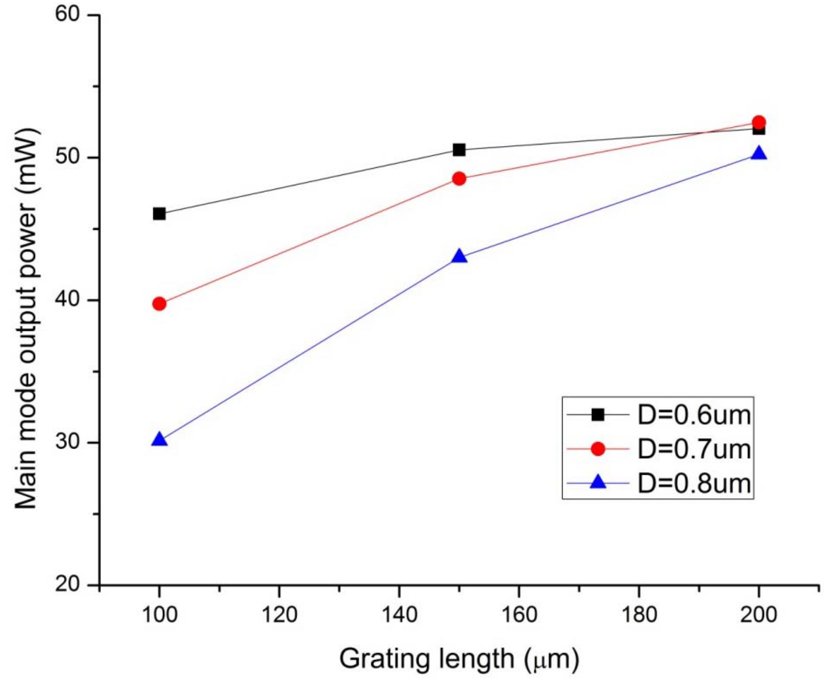

Figure 5-13. Output power of the DBR laser when varying the spacing and the grating length; I=40mA

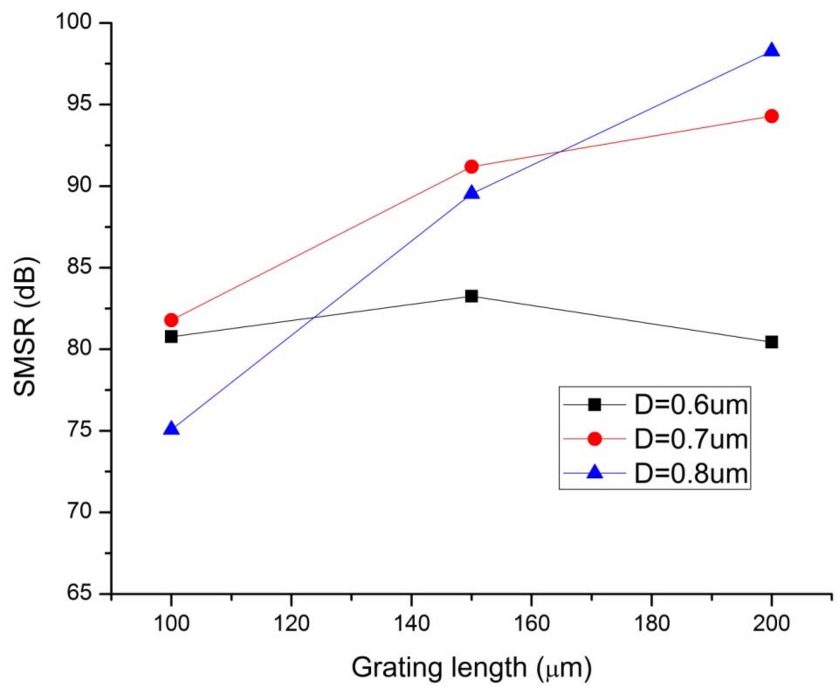

Figure 5-14. SMSR of the DBR laser when varying the spacing and the grating length; I=40mA

From Figure 5-13 we can also see that, for a short grating length such as 100μm, with a smaller spacing *D*, such as 0.6μm, the output power is higher than that of a larger spacing, thus the threshold current is lower. This is because the coupling is stronger and the peak reflectivity can reach a higher value for a short grating length. And if the grating length is long enough, for example, when it equals 200μm, the peak reflectivity is close to 1 for all spacing *D,* such that, the output power does not have much difference as we can see in Figure 5-13.

As for the SMSR, from Figure 5-14 we can see that, for a larger spacing *D*, such as 0.8μm, or with weaker coupling, the SMSR can reach higher value with a long grating length such as 200μm. This is because with weaker coupling and if the grating length is long enough, the reflectivity spectrum has a smaller bandwidth comparing to a stronger coupling. But for a small spacing such as 0.6μm, the SMSR doesn't improve much when increasing the grating length.

Therefore, if a short cavity length is needed, a relatively smaller spacing should be chosen; if a very high SMSR is required, relatively larger spacing and longer grating length should be designed.

5.4 Summary

In this chapter I propose a novel design of the DBR laser by replacing the index-grating with the periodically-buried metal nano-strips. By varying the design parameters of the metal grating, a wide range of the coupling constant is achieved, partially because of the large refractive-index difference of the metal and the surrounding semiconductor.

First of all, the simulation method of the metal grating is investigated. The coupled-wave theory which is commonly used for the index-grating now shows a limited accuracy because of the large index difference. Therefore, the complex mode matching method is applied. The simulation shows that the results of the two methods differ in the values and the difference depends on the parameters of the metal grating.

Then using the two methods, the coupling constant and the reflection spectrum of the metal grating is researched with different settings of the grating parameters, such as the spacing of the metal-strips and the core region, the grating length and the duty cycle. As predicted, the coupling constant reaches for a wide range when varying the spacing of the metal-strips and the core region. When the spacing and the grating length are both changed, we get different values of κL, and also the reflection spectrum can be tuned accordingly for different requirements of the peak reflectivity and the FWHM. Moreover, to be used as a reflector for the DBR laser, the duty cycle of the metal grating is fixed at 50% because the simulation shows the peak reflectivity drops dramatically when the duty cycle is away from this value.

Lastly, the rate-equation simulation of the metal-grating DBR laser demonstrates the single-mode operation for a broad range of the metal-grating's design parameters, thus the design freedom is provided. For various applications of the DBR laser, the requirements such as a shorter cavity length, a lower threshold current, or a very high SMSR can be satisfied by properly changing the design parameters.

Chapter 6
Conclusions and Future Topics

6.1 Summary of Contributions

The objective of this thesis was to theoretically investigate the semiconductor laser diode design with the new nano-materials such as the semiconductor quantum dot or metal nano-particle and metal nano-strips, whereas the research topics for each category are different because of the unequal development level of related devices for the current stage. Research on the QD FP laser focuses on the gain-broadening effects which usually prevent the single-mode operation; on the QD DFB laser, the one-dimensional standing wave model is developed to further uncover its properties; on the metal nano-particles, the methods that are able to adjust the SPP resonance wavelength and Q-factor are discussed; and a metal-strip based Bragg grating is adopted for the design of a novel DBR laser.

The major contributions of this thesis are summarized as follows.

1. An optimizing scheme of the QD FP laser for the single longitudinal-mode selectivity is established. It is concluded that for each given inhomogeneous broadening, the optimum homogeneous broadening can be obtained from a rate-equation analysis of the gain-broadening effects of such laser.

2. The condition for the single-mode operation of QD FP laser is discussed quantitatively with the optimized values of the gain-broadening effects and a single-mode QD FP laser is designed and analysed.
3. The one-dimensional standing-wave model for the QD DFB laser is developed and applied. With this model a typical QD DFB laser is simulated and the dynamic modulation response is discussed.
4. The LSPP effect of the metal nano-particle is investigated by Mie theory calculation with the emphasis on the tunableness of the resonance wavelength and Q-factor. It is shown that the resonance can be moved to the wavelengths for optical communications by suitable methods.
5. A novel Bragg grating based on the metal nano-strips is studied by the coupled-wave theory and the mode-matching method. Results show that the coupling constant can be tuned in a wide range by modifying the spacing of the grating and the core region, while the reflection spectrum can be designed accordingly for different requirements.
6. A DBR laser is designed based on the metal nano-strip grating. Simulation results show that it works under single-mode operation for a broad range of design parameters of the metal grating.

6.2 Suggestions for Future Research Topics

The idea of applying the nano-materials to the semiconductor laser cavity leads to great possibilities of further improving the device performance and gives rise to extensive research. Although this thesis has involved in many aspects and demonstrates clear results, there still remain some research topics worth further study. Therefore, I suggest the following recommendations for future work:

1. **The tunableness of the homogeneous broadening effect of QD.** To design the quantum dots and obtain the required homogeneous broadening bandwidth, several possible methods is required to be further investigated. For example, by controlling the energy levels of QD with suitable shape or composition, the homogeneous broadening can be tuned.
2. **Metal grating based on the metal nano-particles.** Instead of using the metal nano-strips, the metal grating can be designed based on the metal nano-particles. The wavelength selectivity due to the LSPP resonance may assist on the single-mode selection for the DBR laser, as a result, the grating length may be reduced while sufficient reflection is still provided, and hopefully, if it is short enough, the re-growth process during fabrication may not be needed any longer. This will eventually save the cost of the DBR laser.

Appendix A High-order Finite-Difference mode solver

The conventional finite difference method for TE or TM modes in waveguides uses the central difference (or forward/backward difference, for some occasions) formula. For TE modes, the wave equation for a one-dimensional waveguide structure and the central difference formula are [135],

$$\frac{d^2\hat{E}_y}{dx^2} + n^2\left(x\right)k^2\hat{E}_y = \beta^2\hat{E}_y \tag{A.1}$$

$$\frac{d^2\hat{E}_y}{dx^2} = \frac{\hat{E}_y^{i+1} + \hat{E}_y^{i-1} - 2\hat{E}_y^{i}}{\Delta x^2} + \mathrm{O}\left(\Delta x^3\right) \tag{A.2}$$

And for TM modes,

$$n^2\frac{d}{dx}\left(\frac{1}{n^2}\frac{d}{dx}\hat{H}_y\right) + n^2k^2\hat{H}_y = \beta^2\hat{H}_y \tag{A.3}$$

$$n^2\frac{d}{dx}\left(\frac{1}{n^2}\frac{d}{dx}\hat{H}_y\right) = \frac{n_i^2}{\Delta x^2}\left(\frac{1}{\left(n_{i+0.5}^2\right)}\hat{H}_y{}^{i+1} + \frac{1}{\left(n_{i-0.5}^2\right)}\hat{H}_y{}^{i-1} - \left(\frac{1}{\left(n_{i+0.5}^2\right)} + \frac{1}{\left(n_{i-0.5}^2\right)}\right)\hat{H}_y{}^{i}\right) + \mathrm{O}\left(\Delta x^3\right) \tag{A.4}$$

The central difference formula is based on scalar approximation and the accuracy is even worse if the index interface is not in the middle between the sampled points. To improve the accuracy, Chiou derived formulas based on higher-order Taylor expansion [126]. From the derivation, the fields at interface are expressed by Taylor series of the fields at sampled points and then matched using interface conditions.

Figure A-1 shows a general three sampled points and the interfaces between them at random locations. The formulas are listed as below.

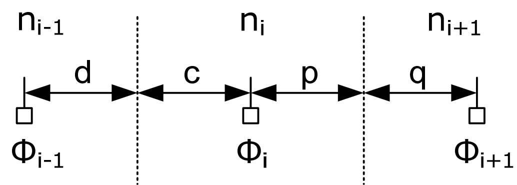

Figure A-6-1. Three sampled points and the interfaces [126]

From the Taylor expansion,

$$\begin{aligned}\phi_{i-1} &= e_0\phi_i + e_1\phi_i' + e_2\phi_i'' + e_3\phi_i''' + e_4\phi_i^{(4)} + O(\Delta x^5)\\ \phi_{i+1} &= f_0\phi_i + f_1\phi_i' + f_2\phi_i'' + f_3\phi_i''' + f_4\phi_i^{(4)} + O(\Delta x^5)\end{aligned} \tag{A.5}$$

the generalized Douglas scheme for the finite difference is,

$$\begin{aligned}\phi_i' &\approx \frac{f_2\phi_{i-1} + (f_0e_2 - e_0f_2)\phi_i - e_2\phi_{i+1}}{e_1f_2 - f_2e_1} = s_-\phi_{i-1} + s_0\phi_i + s_+\phi_{i+1} \equiv D_x\phi_i\\ \phi_i'' &\approx \frac{f_1\phi_{i-1} + (f_0e_1 - e_0f_1)\phi_i - e_1\phi_{i+1}}{e_2f_1 - f_1e_2} = t_-\phi_{i-1} + t_0\phi_i + t_+\phi_{i+1} \equiv D_x^2\phi_i\end{aligned} \tag{A.6}$$

And we have the relation [126],

$$D_x^2\phi_i \approx \left(1 + g_1D_x + g_2D_x^2\right)\phi_i'' \tag{A.7}$$

where,

$$g_1 = \frac{f_1e_3 - e_1f_3}{f_1e_2 - e_1f_2},\ \ g_2 = \frac{f_1e_4 - e_1f_4}{f_1e_2 - e_1f_2} \tag{A.8}$$

Then from the Helmholtz equation,

$$\phi'' + k_0^2n^2\phi = \beta^2\phi \tag{A.9}$$

using the above relation, we have,

$$D_x^2\phi_i + k_0^2 n^2\left(1 + g_1 D_x + g_2 D_x^2\right)\phi_i = \beta^2\left(1 + g_1 D_x + g_2 D_x^2\right)\phi_i \tag{A.10}$$

Therefore, the Eigen-value equation in matrix form is [126],

$$C^{-1}[A + k_0^2 N^2 (C - I)]\Phi = \beta^2\Phi \tag{A.11}$$

where,

$$\begin{aligned} &A: \ D_x^2 + k_0^2 n^2 \\ &N^2: \ diag(n_1^2, n_2^2, ..., n_i^2, ...) \\ &C: \ 1 + g_1 D_x + g_2 D_x^2 \end{aligned} \tag{A.12}$$

and as shown in equation (A.6), D_x consists of elements s_-, s_0, s_+ ; $D_x{}^2$ consists of elements t_-, t_0, t_+ ; both are quasi-diagonal.

The parameters e and f are derived from the interface matching and Taylor expansion at interface [126],

$$\begin{aligned} f_0 &= 1 + \frac{q^2\eta}{2} + \frac{q^4\eta^2}{24} + O(\Delta x^6) \\ f_1 &= p + \frac{pq^2\eta}{2} + \frac{pq^4\eta^2}{24} + \theta(q + \frac{q^3\eta}{6} + \frac{q^5\eta^2}{120}) + O(\Delta x^6) \\ f_2 &= \frac{p^2}{2} + \frac{q^2}{2} + \frac{p^2q^2\eta}{4} + \frac{q^4\eta}{12} + \theta(pq + \frac{pq^3\eta}{6}) + O(\Delta x^6) \\ f_3 &= \frac{p^3}{6} + \frac{pq^2}{2} + \frac{p^3q^2\eta}{12} + \frac{pq^4\eta}{12} + \theta(\frac{p^2q}{2} + \frac{q^3}{6} + \frac{p^2q^3\eta}{12} + \frac{q^5\eta}{60}) + O(\Delta x^6) \\ f_4 &= \frac{p^4}{24} + \frac{p^2q^2}{4} + \frac{q^4}{24} + \theta(\frac{p^3q}{6} + \frac{pq^3}{6}) + O(\Delta x^6) \end{aligned} \tag{A.13}$$

where,

$$\begin{aligned} &\eta = k_0^2\left(n_i^2 - n_{i+1}^2\right) \\ &\theta = \begin{cases} 1, & \text{for TE modes} \\ n_{i+1}^2 / n_i^2 , & \text{for TM modes} \end{cases} \end{aligned} \tag{A.14}$$

and $e_0,...,e_4$ can be written by replacing $p \to (-c), q \to (-d), n_{i+1} \to n_{i-1}$.

Appendix B Deduction of the coupled-wave theory

The coupled-wave theory is derived from the wave equation for a waveguide structure of which the dielectric tensor is periodically perturbed. For a one-dimensional waveguide structure (the refractive index is invariant along the y-direction, i.e., homogeneous in the scope of the modal field),

$$\varepsilon(x,z)=\varepsilon_a(x)+\Delta\varepsilon(x,z) \tag{B.1}$$

For the unperturbed structure with ε_a, we can solve for the modes. If m indicates the mode number, β_m and $\mathbf{E}_m(x)$ represent the propagation constant and the modal profile of the m-th mode, we have,

$$\left(\frac{\partial^2}{\partial x^2}+\frac{\partial^2}{\partial y^2}+\omega^2\mu\varepsilon_a(x)\right)\mathbf{E}_m(x)=\beta_m^2\mathbf{E}_m(x) \tag{B.2}$$

$\mathbf{E}_m(x)$ is normalized to satisfy,

$$\frac{1}{2}\mathrm{Re}\int\left(\mathbf{E}_m\times\mathbf{H}_m^*\right)\cdot\hat{z}dx=1 \tag{B.3}$$

where $\mathbf{H}_m(x)$ represents the associated magnetic field. And the modes are orthogonal,

$$\int\left(\mathbf{E}_m\times\mathbf{H}_n\right)\cdot\hat{z}dx=0 \quad \text{when } m\neq n \tag{B.4}$$

Due to the perturbation $\Delta\varepsilon$, the energy exchanges between the normal modes. Assume the perturbation is ‘weak’; the waves can be decomposed into the normal modes with slow-varying amplitudes $A_m(z)$,

$$\mathbf{E} = \sum_m A_m(z)\mathbf{E}_m(x)e^{j(\omega t - \beta_m z)} \tag{B.5}$$

The wave equation for the perturbed structure is,

$$\nabla^2 \mathbf{E} + \omega^2 \mu\left[\varepsilon_a(x) + \Delta\varepsilon(x,z)\right]\mathbf{E} = 0 \tag{B.6}$$

Substitute (B.2) into the wave equation and using the slow-varying condition that $\frac{d^2}{dz^2}A_m << \beta_m \frac{d}{dz}A_m$, we can get,

$$-2j\sum_m \beta_m \frac{dA_m(z)}{dz}\mathbf{E}_m(x)e^{-j\beta_m z} = -\omega^2\mu\sum_m \Delta\varepsilon(x,z)A_m(z)\mathbf{E}_m(x)e^{-j\beta_m z} \tag{B.7}$$

Then take the dot product of (B.7) with $\mathbf{E}_n(x)$ and integrate over *x*, using the orthogonal relations, and also for TE or TM modes we have,

$$\int\left(\mathbf{E}_m(x)\cdot\mathbf{E}_m(x)\right)dx = \frac{2\omega\mu}{|\beta_m|} \tag{B.8}$$

Therefore, we get,

$$\frac{dA_m(z)}{dz} = -j\frac{\beta_m}{|\beta_m|}\sum_n \frac{\omega}{4}\left\langle n\left|\Delta\varepsilon\right|m\right\rangle A_m(z)e^{-j(\beta_m-\beta_n)z} \tag{B.9}$$

where,

$$\left\langle n\left|\Delta\varepsilon\right|m\right\rangle = \int\left(\mathbf{E}_n(x)\cdot\Delta\varepsilon(x,z)\mathbf{E}_m(x)\right)dx \tag{B.10}$$

Because of the periodicity, we can take the Fourier expansion of the perturbation $\Delta\varepsilon(x,z)$ along z-direction,

$$\Delta\varepsilon(x,z) = \sum_{p=1,2,3,\ldots}\varepsilon_p(x)\exp\left(-ip\frac{2\pi}{\Lambda}z\right) \tag{B.11}$$

where Λ denotes the period of the perturbation. Then the coupled-wave equation (B.9) leads to [128],

$$\frac{dA_m(z)}{dz} = -j\frac{\beta_m}{|\beta_m|}\sum_n\sum_p C_{nm}^{(p)} A_m(z) e^{-j(\beta_m - \beta_n + p\frac{2\pi}{\Lambda})z} \tag{B.12}$$

where the coupling coefficient $C_{nm}^{(p)}$ represents the coupling between the n-th and m-th modes due to the p-th order of perturbation [128],

$$C_{nm}^{(p)} = \frac{\omega}{4}\left\langle n\middle|\varepsilon_p(x)\middle|m\right\rangle = \frac{\omega}{4}\int\left(\mathbf{E}_n(x)\cdot\varepsilon_p(x)\mathbf{E}_m(x)\right)dx \tag{B.13}$$

In our case, the grating is along z-direction and the total length is L. Consider the fundamental mode of which the modal profile is $\phi(x)$, the forward propagating mode has amplitude of $A(z)$ and the backward one has amplitude of $B(z)$, both are functions along z-direction with complex values. Then the total field is,

$$E(x,z) = A(z)\phi(x)e^{-j(\tilde{\beta}z-\omega t)} + B(z)\phi(x)e^{j(\tilde{\beta}z+\omega t)} \tag{B.14}$$

where $\tilde{\beta}$ represents the complex propagation constant,

$$\tilde{\beta} = n_{eff}k_0 = n_{eff}^R k_0 + i n_{eff}^I k_0 = \beta + i\gamma \tag{B.15}$$

R and I stand for the real part and imaginary part, respectively. Now γ represents the modal gain/loss, $\gamma = n_{eff}^I k_0$. When γ is negative, the mode is lossy, due to the material loss or coupling to radiation modes.

Then considering the contra-directional coupling due to the first-order grating, according to (B.12), the coupled-wave equation is,

$$\frac{dA(z)}{dz} = -i\kappa B(z)e^{i2\Delta\tilde{\beta}z}$$
$$\frac{dB(z)}{dz} = i\kappa A(z)e^{-i2\Delta\tilde{\beta}z} \tag{B.16}$$

where,

$$\Delta\tilde{\beta} = \frac{1}{2}\left(2\tilde{\beta} - \frac{2\pi}{\Lambda}\right) = \left(\beta - \frac{\pi}{\Lambda}\right) + i\gamma = \Delta\beta + i\gamma \tag{B.17}$$

$$\kappa = \frac{\omega}{4}\int \phi(x)\cdot\varepsilon_1(x)\phi(x)dx \tag{B.18}$$

and $\varepsilon_1(x)$ is the first-order Fourier coefficient of the perturbation $\Delta\varepsilon(x)$,

Further, with the condition that *B(L)=0,* the coupled-wave equation (B.16) has the analytical solution [128],

$$A(z) = A(0)e^{i\Delta\tilde{\beta}z}\,\frac{S\cosh\left(S\left(L-z\right)\right) + i\Delta\tilde{\beta}\sinh\left(S\left(L-z\right)\right)}{S\cosh\left(SL\right) + i\Delta\tilde{\beta}\sinh\left(SL\right)}$$
$$B(z) = A(0)e^{-i\Delta\tilde{\beta}z}\,\frac{-i\kappa\sinh\left(S\left(L-z\right)\right)}{S\cosh\left(SL\right) + i\Delta\tilde{\beta}\sinh\left(SL\right)} \tag{B.19}$$

where,

$$S = \sqrt{\kappa^2 - \Delta\tilde{\beta}^2} = \sqrt{\kappa^2 - \left(\Delta\beta + i\gamma\right)^2} = \sqrt{\kappa^2 + \left(\gamma - i\Delta\beta\right)^2} \tag{B.20}$$

Therefore, we get the reflectivity and transmission of the grating [128],

$$R = \frac{B(0)}{A(0)} = \frac{-i\kappa\sinh SL}{S\cosh SL + i(\Delta\beta + i\gamma)\sinh SL} \tag{B.21}$$

$$T = \frac{A(L)}{A(0)} = e^{i\Delta\tilde{\beta}L}\,\frac{S}{S\cosh\left(SL\right) + i(\Delta\beta + i\gamma)\sinh\left(SL\right)} \tag{B.22}$$

Appendix C Deduction of the mode matching method

The mode matching method (MMM) is generally used for modelling the discontinuities along the optical waveguide [136-138]. Here a brief deduction of the formula used in this thesis is given.

In a z-invariant waveguide, the field can be decomposed into a series of waveguide modes. For example, if we consider the first N modes which are significant, the tangential electric and magnetic fields can be expressed as,

$$\begin{aligned}\mathbf{E}_t &= \sum_{i=1}^{N}\left(a_i e^{-j\beta_i z} + b_i e^{j\beta_i z}\right)\mathbf{e}_{ti} \\ \mathbf{H}_t &= \sum_{i=1}^{N}\left(a_i e^{-j\beta_i z} - b_i e^{j\beta_i z}\right)\mathbf{h}_{ti}\end{aligned} \tag{C.1}$$

where β_i represents the propagation constant for the i-th mode; a_i and b_i represent the modal amplitudes for the forward and backward wave, respectively; $\mathbf{e}_{ti}$ and $\mathbf{h}_{ti}$ represent the normalized mode pattern for the tangential electric and magnetic fields, respectively, and the modes are orthogonal to each other, i.e., the inner product satisfies,

$$\left\langle \mathbf{e}_{ti}, \mathbf{h}_{tk} \right\rangle = \frac{1}{4}\int \left(\mathbf{e}_{ti}^* \times \mathbf{h}_{tk} + \mathbf{e}_{ti} \times \mathbf{h}_{tk}^*\right)\cdot \hat{z} ds = \delta_{ik} \tag{C.2}$$

If there is a discontinuity of refractive index in the waveguide structure, the modes on each side can be solved by the mode solver and the modal amplitudes can be matched through the boundary conditions. Choose z=0 at the interface without loss of generality, because of the continuity of the tangential fields, we have [137],

$$\begin{aligned}\sum_{i=1}^{N}\left(a_i^L+b_i^L\right)\mathbf{e}_{ti}^L&=\sum_{i=1}^{N}\left(a_i^R+b_i^R\right)\mathbf{e}_{ti}^R\\\sum_{i=1}^{N}\left(a_i^L-b_i^L\right)\mathbf{h}_{ti}^L&=\sum_{i=1}^{N}\left(a_i^R-b_i^R\right)\mathbf{h}_{ti}^R\end{aligned}\tag{C.3}$$

where the superscript L and R denote the waveguides on the left side (z<0) and the right side (z>0) of the junction, respectively. Take inner product of the two equations of (C.3) with $\mathbf{h}_{tk}^R$ and $\mathbf{e}_{tk}^R$, respectively, and we can get [137],

$$\begin{aligned}a_k^R&=\sum_{i=1}^{N}a_i^L\frac{\left\langle\mathbf{e}_{ti}^L,\mathbf{h}_{tk}^R\right\rangle+\left\langle\mathbf{e}_{tk}^R,\mathbf{h}_{ti}^L\right\rangle}{2\left\langle\mathbf{e}_{tk}^R,\mathbf{h}_{tk}^R\right\rangle}+\sum_{i=1}^{N}b_i^L\frac{\left\langle\mathbf{e}_{ti}^L,\mathbf{h}_{tk}^R\right\rangle-\left\langle\mathbf{e}_{tk}^R,\mathbf{h}_{ti}^L\right\rangle}{2\left\langle\mathbf{e}_{tk}^R,\mathbf{h}_{tk}^R\right\rangle}\\b_k^R&=\sum_{i=1}^{N}a_i^L\frac{\left\langle\mathbf{e}_{ti}^L,\mathbf{h}_{tk}^R\right\rangle-\left\langle\mathbf{e}_{tk}^R,\mathbf{h}_{ti}^L\right\rangle}{2\left\langle\mathbf{e}_{tk}^R,\mathbf{h}_{tk}^R\right\rangle}+\sum_{i=1}^{N}b_i^L\frac{\left\langle\mathbf{e}_{ti}^L,\mathbf{h}_{tk}^R\right\rangle+\left\langle\mathbf{e}_{tk}^R,\mathbf{h}_{ti}^L\right\rangle}{2\left\langle\mathbf{e}_{tk}^R,\mathbf{h}_{tk}^R\right\rangle}\end{aligned}\tag{C.4}$$

Equation (C.4) gives the modal amplitudes on the right side of the junction. Denote the vector $\left[a_1^R,a_2^R,\cdots,a_N^R\right]$ with A^R, $\left[b_1^R,b_2^R,\cdots,b_N^R\right]$ with B^R, $\left[a_1^L,a_2^L,\cdots,a_N^L\right]$ with A^L and $\left[b_1^L,b_2^L,\cdots,b_N^L\right]$ with B^L. From (C.4) we can express the junction by the transfer matrix T,

$$\begin{bmatrix}A^R\\B^R\end{bmatrix}=\begin{bmatrix}T_{11}&T_{12}\\T_{21}&T_{22}\end{bmatrix}\begin{bmatrix}A^L\\B^L\end{bmatrix}\tag{C.5}$$

and the transfer matrix can be changed into the scattering matrix S,

$$\begin{bmatrix}A^R\\B^L\end{bmatrix}=\begin{bmatrix}S_{11}&S_{12}\\S_{21}&S_{22}\end{bmatrix}\begin{bmatrix}A^L\\B^R\end{bmatrix}\tag{C.6}$$

The relationship is,

$$
\begin{aligned}
S_{11} &= T_{11} - T_{12} \cdot T_{22}^{-1} \cdot T_{21} \\
S_{12} &= T_{12} \cdot T_{22}^{-1} \\
S_{21} &= -T_{22}^{-1} \cdot T_{21} \\
S_{22} &= T_{22}^{-1}
\end{aligned}
\tag{C.7}
$$

The above scattering matrix also describes the junction or the refractive index discontinuity. After the junction, the wave propagates in a z-invariant waveguide and the propagation matrix is P for all the modes,

$$P = diag\left(e^{-j\beta_1 L}, e^{-j\beta_2 L}, \cdots, e^{-j\beta_N L}\right) \tag{C.8}$$

Cascade it into the scattering matrix of the junction, and the new scattering matrix S^{new} describes the junction and the following propagating section [137],

$$S^{new} = \begin{bmatrix} PS_{11} & PS_{12}P \\ S_{21} & S_{22}P \end{bmatrix} \tag{C.9}$$

The whole structure can be described by cascading the scattering matrix layer by layer from the input port to the output port. To cascade the scattering matrix, assume S^0 is the scattering matrix from the input port to current layer, and S^{next} is the scattering matrix of the next layer, the scattering matrix S from the input port to the next layer is obtained by this calculation [137],

$$
\begin{aligned}
S_{11} &= S_{11}^{next}\left(I - S_{12}^{0} S_{21}^{next}\right)^{-1} S_{11}^{0} \\
S_{12} &= S_{11}^{next}\left(I - S_{12}^{0} S_{21}^{next}\right)^{-1} S_{12}^{0} S_{22}^{next} + S_{12}^{next} \\
S_{21} &= S_{22}^{0}\left(I - S_{21}^{next} S_{12}^{0}\right)^{-1} S_{21}^{next} S_{11}^{0} + S_{21}^{0} \\
S_{22} &= S_{22}^{0}\left(I - S_{21}^{next} S_{12}^{0}\right)^{-1} S_{22}^{next}
\end{aligned}
\tag{C.10}
$$

After the scattering matrix is found, the structure is solved by multiply the scattering matrix with the given input modal amplitudes.

Bibiography

[1] W. W. Chow and S. W. Koch, *Semiconductor-Laser Fundamentals: Physics of the Gain Materials*: Springer, 1999.

[2] P. Harrison, *Quantum wells, wires and dots*: Wiley West Sussex, 2005.

[3] O. B. Shchekin and D. G. Deppe, "1.3μm InAs quantum dot laser with T= 161 K from 0 to 80°C," *Applied Physics Letters*, vol. 80, pp. 3277, 2002.

[4] S. A. Maier, *Plasmonics: Fundamentals and Applications*: Springer, 2007.

[5] A. V. Zayats, I. I. Smolyaninov, and A. A. Maradudin, "Nano-optics of surface plasmon polaritons," *Physics reports*, vol. 408, pp. 131-314, 2005.

[6] S. I. Bozhevolnyi, J. Erland, K. Leosson, P. M. Skovgaard, and J. M. Hvam, "Waveguiding in surface plasmon polariton band gap structures," *Physical review letters*, vol. 86, pp. 3008-3011, 2001.

[7] S. I. Bozhevolnyi, V. S. Volkov, K. Leosson, and A. Boltasseva, "Bend loss in surface plasmon polariton band-gap structures," *Applied Physics Letters*, vol. 79, pp. 1076, 2001.

[8] T. D. Backes and D. S. Citrin, "Plasmon Polaritons in 2-D Nanoparticle Arrays," *IEEE Journal of Selected Topics in Quantum Electronics*, vol. 14, pp. 1530-1535, 2008.

[9] W. L. Barnes, W. A. Murray, J. Dintinger, E. Devaux, and T. W. Ebbesen, "Surface plasmon polaritons and their role in the enhanced transmission of light

through periodic arrays of subwavelength holes in a metal film," *Physical review letters*, vol. 92, pp. 107401, 2004.

[10] L. Salomon, F. Grillot, A. V. Zayats, and F. de Fornel, "Near-Field Distribution of Optical Transmission of Periodic Subwavelength Holes in a Metal Film," *Physical review letters*, vol. 86, pp. 1110, 2001.

[11] L. Martin-Moreno, F. J. Garcia-Vidal, H. J. Lezec, K. M. Pellerin, T. Thio, J. B. Pendry, and T. W. Ebbesen, "Theory of Extraordinary Optical Transmission through Subwavelength Hole Arrays," *Physical review letters*, vol. 86, pp. 1114, 2001.

[12] H. Gao, J. Henzie, and T. W. Odom, "Direct Evidence for Surface Plasmon-Mediated Enhanced Light Transmission through Metallic Nanohole Arrays," *Nano Letters*, vol. 6, pp. 2104-2108, 2006.

[13] J. W. Mu and W. P. Huang, "A low-loss surface plasmonic Bragg grating," *Journal of Lightwave Technology*, vol. 27, pp. 436-439, 2009.

[14] A. Boltasseva, S. I. Bozhevolnyi, T. Nikolajsen, and K. Leosson, "Compact Bragg gratings for long-range surface plasmon polaritons," *Journal of Lightwave Technology,* vol. 24, pp. 912-918, 2006.

[15] S. I. Bozhevolnyi, A. Boltasseva, T. S, T. Nikolajsen, and K. Leosson, "Photonic bandgap structures for long-range surface plasmon polaritons," *Optics Communications*, vol. 250, pp. 328-333, 2005.

[16] C. S. Jett and P. Berini, "External cavity laser using a long-range surface plasmon grating as a distributed Bragg reflector," *Applied Physics Letters*, vol. 91, pp. 181114, 2007.

[17] J. A. Porto, F. J. Garcia-Vidal, and J. B. Pendry, "Transmission resonances on metallic gratings with very narrow slits," *Physical review letters*, vol. 83, pp. 2845, 1999.

[18] S. Astilean, P. Lalanne, and M. Palamaru, "Light transmission through metallic channels much smaller than the wavelength," *Optics Communications*, vol. 175, pp. 265-273, 2000.

[19] Z. Yu, P. Deshpande, W. Wu, J. Wang, and S. Y. Chou, "Reflective polarizer based on a stacked double-layer subwavelength metal grating structure fabricated using nanoimprint lithography," *Applied Physics Letters*, vol. 77, pp. 927, 2000.

[20] M. H. Lee, H. Gao, and T. W. Odom, "Refractive Index Sensing Using Quasi One-Dimensional Nanoslit Arrays," *Nano Letters*, vol. 9, pp. 2584-2588, 2009.

[21] M. J. Kofke, D. H. Waldeck, and G. C. Walker, "Composite nanoparticle nanoslit arrays: a novel platform for LSPR mediated subwavelength optical transmission," *Optics Express*, vol. 18, pp. 7705-7713, 2010.

[22] T. W. Lee and S. Gray, "Subwavelength light bending by metal slit structures," *Optics Express*, vol. 13, pp. 9652-9659, 2005.

[23] Y. Xie, A. Zakharian, J. Moloney, and M. Mansuripur, "Transmission of light through a periodic array of slits in a thick metallic film," *Optics Express*, vol. 13, pp. 4485-4491, 2005.

[24] Y. Xie, A. Zakharian, J. Moloney, and M. Mansuripur, "Transmission of light through slit apertures in metallic films," *Optics Express*, vol. 12, pp. 6106-6121, 2004.

[25] G. Veronis and S. Fan, "Bends and splitters in metal-dielectric-metal subwavelength plasmonic waveguides," *Applied Physics Letters*, vol. 87, pp. 131102, 2005.

[26] W. P. Huang, X. Li, C. Q. Xu, X. Hong, C. Xu, and W. Liang, "Optical transceivers for fiber-to-the-premises applications: System requirements and enabling technologies," *Journal of Lightwave Technology*, vol. 25, pp. 11-27, 2007.

[27] D. Bimberg, M. Grundmann, F. Heinrichsdorff, N. N. Ledentsov, V. M. Ustinov, A. E. Zhukov, A. R. Kovsh, M. V. Maximov, Y. M. Shernyakov, and B. V. Volovik, "Quantum dot lasers: breakthrough in optoelectronics," *Thin Solid Films*, vol. 367, pp. 235-249, 2000.

[28] H. Ishikawa, H. Shoji, Y. Nakata, K. Mukai, M. Sugawara, M. Egawa, N. Otsuka, Y. Sugiyama, T. Futatsugi, and N. Yokoyama, "Self-organized quantum dots and quantum dot lasers (invited)," *Journal of Vacuum Science & Technology A: Vacuum, Surfaces, and Films*, vol. 16, pp. 794, 1998.

[29] F. Lelarge, B. Dagens, J. Renaudier, R. Brenot, A. Accard, D. F. van, D. Make, G. O. Le, J. G. Provost, F. Poingt, J. Landreau, O. Drisse, E. Derouin, B. Rousseau, F.

Pommereau, and G. H. Duan, "Recent advances on InAs/InP quantum dash based, semiconductor lasers and optical amplifiers operating at 1.55 mu m," *IEEE Journal of Selected Topics in Quantum Electronics*, vol. 13, pp. 111-124, 2007.

[30] P. Bhattacharya, S. Ghosh, and A. D. Stiff-Roberts, "Quantum dot opto-electronic devices," *Annual Review of Materials Research*, vol. 34, pp. 1-40, 2004.

[31] H. Schweizer, M. Jetter, and F. Scholz, "Quantum-Dot Lasers," *Topics in Applied Physics*, vol. 90, pp. 185-236, 2003.

[32] J. P. Reithmaier and A. Forchel, "Recent advances in semiconductor quantum-dot lasers," *Comptes Rendus Physique*, vol. 4, pp. 611-619, 2003.

[33] D. Bimberg, M. Grundmann, N. N. Ledentsov, M. H. Mao, C. Ribbat, R. Sellin, V. M. Ustinov, A. E. Zhukov, Z. I. Alferov, and J. A. Lott, "Novel infrared quantum dot lasers: theory and reality," *Physica Status Solidi B-Basic Solid State Physics*, vol. 224, pp. 787-796, 2001.

[34] M. Grundmann, "The present status of quantum dot lasers," *Physica E*, vol. 5, pp. 167, 2000.

[35] M. Sugawara, "Theoretical bases of the optical properties of semiconductor quantum nano-structures," *Semiconductors and Semimetals*, vol. 60, pp. 1-116, 1999.

[36] N. Kirstaedter, O. G. Schmidt, N. N. Ledentsov, D. Bimberg, V. M. Ustinov, A. Y. Egorov, A. E. Zhukov, M. V. Maximov, P. S. Kop, and Z. I. Alferov, "Gain and differential gain of single layer InAs/GaAs quantum dot injection lasers," *Applied Physics Letters*, vol. 69, pp. 1226, 1996.

[37] Y. Arakawa and H. Sakaki, "Multidimensional quantum well laser and temperature dependence of its threshold current," *Applied Physics Letters*, vol. 40, pp. 939, 1982.

[38] G. T. Liu, A. Stintz, H. Li, K. J. Malloy, and L. F. Lester, "Extremely low room-temperature threshold current density diode lasers using InAs dots in $In_{0.15}Ga_{0.85}As$ quantum well," *Electronics Letters*, vol. 35, pp. 1163-1165, 1999.

[39] K. Mukai, Y. Nakata, K. Otsubo, M. Sugawara, N. Yokoyama, and H. Ishikawa, "High characteristic temperature of near-1.3μm InGaAs/GaAs quantum-dot lasers at room temperature," *Applied Physics Letters*, vol. 76, pp. 3349, 2000.

[40] X. Huang, A. Stintz, C. P. Hains, G. T. Liu, J. Cheng, and K. J. Malloy, "Very low threshold current density room temperature continuous-wave lasing from a single-layer InAs quantum-dot laser," *IEEE Photonics Technology Letters*, vol. 12, pp. 227-229, 2000.

[41] R. L. Sellin, C. Ribbat, M. Grundmann, N. N. Ledentsov, and D. Bimberg, "Close-to-ideal device characteristics of high-power InGaAs/GaAs quantum dot lasers," *Applied Physics Letters*, vol. 78, pp. 1207, 2001.

[42] M. Grundmann, J. Christen, N. N. Ledentsov, J. Bohrer, D. Bimberg, S. S. Ruvimov, P. Werner, U. Richter, U. Gosele, J. Heydenreich, V. M. Ustinov, A. Y. Egorov, A. E. Zhukov, P. S. Kopev, and Z. I. Alferov, "Ultranarrow luminescence lines from single quantum dots," *Physical Review Letters*, vol. 74, pp. 4043, 1995.

[43] J. Marzin, J. Gerard, A. Izrael, D. Barrier, and G. Bastard, "Photoluminescence of single InAs quantum dots obtained by self-organized growth on GaAs," *Physical Review Letters*, vol. 73, pp. 716, 1994.

[44] S. Nishikawa, S. Kohmoto, H. Nakamura, Y. Sugimoto, N. Ikeda, T. Ishikawa, T. Akiyama, H. Ishikawa, and O. Wada, "Dephasing time characterization of InAs quantum dots by four-wave mixing measurement," *Physica E: Low-dimensional Systems and Nanostructures*, vol. 13, pp. 273-277, 2002.

[45] P. Borri, W. Langbein, J. Mork, J. M. Hvam, F. Heinrichsdorff, M. H. Mao, and D. Bimberg, "Dephasing in InAs/GaAs quantum dots," *Physical Review B*, vol. 60, pp. 7784-7787, 1999.

[46] K. Matsuda, K. Ikeda, T. Saiki, H. Tsuchiya, H. Saito, and K. Nishi, "Homogeneous linewidth broadening in a $In_{0.5}Ga_{0.5}As$/GaAs single quantum dot at room temperature investigated using a highly sensitive near-field scanning optical microscope," *Physical Review B*, vol. 63, pp. 121304, 2001.

[47] N. N. Ledentsov, M. V. Maximov, D. Bimberg, T. Maka, C. M. Torres, I. V. Kochnev, I. L. Krestnikov, V. M. Lantratov, N. A. Cherkashin, and Y. M. Musikhin, "1.3μm luminescence and gain from defect-free InGaAs-GaAs quantum dots grown by metal-organic chemical vapour deposition," *Semiconductor Science and Technology*, vol. 15, pp. 604, 2000.

[48] Y. D. Jang, J. S. Yim, U. H. Lee, D. Lee, J. W. Jang, K. H. Park, W. G. Jeong, J. H. Lee, and D. K. Oh, "InAsN/GaAs quantum dots with an intense and narrow

photoluminescence peak at 1.3μm," *Physica E: Low-dimensional Systems and Nanostructures*, vol. 17, pp. 127-128, 2003.

[49] U. A. Griesinger, H. Schweizer, S. Kronmuller, M. Geiger, D. Ottenwalder, F. Scholz, and M. H. Pilkuhn, "Realization of dot DFB lasers," *IEEE Photonics Technology Letters*, vol. 8, pp. 587-589, 1996.

[50] F. Klopf, R. Krebs, A. Wolf, M. Emmerling, J. P. Reithmaier, and A. Forchel, "InAs/GaInAs quantum dot DFB lasers emitting at 1.3μm," *Electronics Letters*, vol. 37, pp. 634-636, 2001.

[51] M. Kamp, M. Schmitt, J. Hofmann, F. Schafer, J. P. Reithmaier, and A. Forchel, "InGaAs/AlGaAs quantum dot DFB lasers operating up to 213°C," *Electronics Letters*, vol. 35, pp. 2036, 1999.

[52] A. Tierno and T. Ackemann, "Tunable, narrow-band light source in the 1.25μm region based on broad-area quantum dot lasers with feedback," *Applied Physics B - Lasers and Optics*, vol. 89, pp. 585-588, 2007.

[53] M. Sugawara, K. Mukai, Y. Nakata, H. Ishikawa, and A. Sakamoto, "Effect of homogeneous broadening of optical gain on lasing spectra in self-assembled $In_xGa_{1-x}As$ /GaAs quantum dot lasers," *Physical Review B*, vol. 61, pp. 7595-7603, 2000.

[54] A. Sakamoto and M. Sugawara, "Theoretical calculation of lasing spectra of quantum-dot lasers: Effect of homogeneous broadening of optical gain," *IEEE Photonics Technology Letters*, vol. 12, pp. 107-109, 2000.

[55] M. Sugawara, N. Hatori, H. Ebe, M. Ishida, Y. Arakawa, T. Akiyama, K. Otsubo, and Y. Nakata, "Modeling room-temperature lasing spectra of 1.3μm self-assembled InAs/GaAs quantum-dot lasers: Homogeneous broadening of optical gain under current injection," *Journal of Applied Physics*, vol. 97, pp. 043523, 2005.

[56] K. David, G. Morthier, P. Vankwikelberge, R. G. Baets, T. Wolf, and B. Borchert, "Gain-coupled DFB lasers versus index-coupled and phase shifted DFB lasers: a comparison based on spatial hole burning corrected yield," *IEEE Journal of Quantum Electronics*, vol. 27, pp. 1714-1723, 1991.

[57] K. David, J. Buus, G. Morthier, and R. Baets, "Coupling coefficients in gain-coupled DFB lasers: Inherent compromise between coupling strength and loss," *IEEE Photonics Technology Letters*, vol. 3, pp. 439-441, 1991.

[58] M. Kamp, J. Hofmann, A. Forchel, F. Schafer, and J. P. Reithmaier, "Low-threshold high-quantum-efficiency laterally gain-coupled InGaAs/AlGaAs distributed feedback lasers," *Applied Physics Letters*, vol. 74, pp. 483, 1999.

[59] A. J. Lowery and D. Novak, "Performance comparison of gain-coupled and index-coupled DFB semiconductor lasers," *IEEE Journal of Quantum Electronics*, vol. 30, pp. 2051-2063, 1994.

[60] Y. Nakano, Y. Deguchi, K. Ikeda, Y. Luo, and K. Tada, "Resistance to external optical feedback in a gain-coupled semiconductor DFB laser," presented at 12th IEEE International Semiconductor Laser Conference Digest, 1990.

[61] R. Hui, M. Kavehrad, and T. Makino, "External feedback sensitivity of partly gain-coupled DFB semiconductor lasers," *Photonics Technology Letters, IEEE*, vol. 6, pp. 897-899, 1994.

[62] T. Inoue, S. Nakajima, Y. Luo, T. Oki, H. Iwaoka, Y. Nakano, and K. Tada, "CW operation of a InGaAsP/InP gain-coupled distributed feedback laser with a corrugated active layer," *Photonics Technology Letters, IEEE*, vol. 3, pp. 958-960, 1991.

[63] M. Kamp, J. Hofmann, F. Schafer, M. Reinhard, M. Fischer, T. Bleuel, J. P. Reithmaier, and A. Forchel, "Lateral coupling - a material independent way to complex coupled DFB lasers," *Optical Materials*, vol. 17, pp. 19-25, 2001.

[64] H. Su, L. Zhang, A. L. Gray, R. Wang, T. C. Newell, K. J. Malloy, and L. F. Lester, "High external feedback resistance of laterally loss-coupled distributed feedback quantum dot semiconductor lasers," *IEEE Photonics Technology Letters*, vol. 15, pp. 1504-1506, 2003.

[65] H. Su, L. Zhang, R. Wang, T. C. Newell, A. L. Gray, and L. F. Lester, "Linewidth study of InAs-InGaAs quantum dot distributed feedback lasers," *IEEE Photonics Technology Letters*, vol. 16, pp. 2206-2208, 2004.

[66] J. Wang, U. A. Griesinger, and H. Schweizer, "Intrinsic carrier capture time in deep-etched quantum-box (70 nm diameter) lasers at low temperature: An indication of extremely high quantum capture efficiency," *Applied Physics Letters*, vol. 70, pp. 1152, 1997.

[67] J. Wang, U. A. Griesinger, M. Geiger, F. Scholz, and H. C. Schweizer, "Carrier capture times in quantum-well,-wire, and-box distributed-feedback lasers characterized by dynamic lasing emission measurements," *IEEE Journal of Selected Topics in Quantum Electronics*, vol. 3, pp. 223-229, 1997.

[68] H. Su and L. F. Lester, "Dynamic properties of quantum dot distributed feedback lasers," *Journal of Physics D: Applied Physics*, vol. 38, pp. 2112-2118, 2005.

[69] W. Li, X. Li, and W. P. Huang, "A traveling-wave model of laser diodes with consideration for thermal effects," *Optical and quantum electronics*, vol. 36, pp. 709-724, 2004.

[70] L. M. Zhang and J. E. Carroll, "Large-signal dynamic model of the DFB laser," *IEEE Journal of Quantum Electronics,* vol. 28, pp. 604-611, 1992.

[71] B. Tromborg, H. E. Lassen, and H. Olesen, "Traveling wave analysis of semiconductor lasers: modulation responses, mode stability and quantum mechanical treatment of noise spectra," *IEEE Journal of Quantum Electronics*, vol. 30, pp. 939-956, 1994.

[72] Y. P. Xi, W. P. Huang, and X. Li, "High-order split-step schemes for time-dependent coupled-wave equations," *IEEE Journal of Quantum Electronics*, vol. 43, pp. 419-425, 2007.

[73] Y. Xi, X. Li, and W. P. Huang, "Time-domain standing-wave approach based on cold cavity modes for simulation of DFB lasers," *IEEE Journal of Quantum Electronics*, vol. 44, pp. 931-937, 2008.

[74] Y. Xi, X. Li, and W. P. Huang, "Standing-wave model based on modes of cold cavity for simulation of laser diodes," *Integrated Photonics and Nanophotonics Research and Applications*, 2007.

[75] Y. Xi, W. P. Huang, and X. Li, "A Standing-Wave Model Based on Threshold Hot-Cavity Modes for Simulation of Gain-Coupled DFB Lasers," *Journal of Lightwave Technology*, vol. 27, pp. 3853-3860, 2009.

[76] Y. Xi, X. Li, and W. P. Huang, "An Efficient Standing-Wave Model for Simulation of λ/4-Shifted DFB Lasers," Asia Optical Fiber Communication and Optoelectronic Exposition and Conference, Optical Society of America, 2008.

[77] H. Kogelnik and C. V. Shank, "Coupled Wave Theory of Distributed Feedback Lasers," *Journal of Applied Physics*, vol. 43, pp. 2327, 1972.

[78] A. Yariv, "Coupled-mode theory for guided-wave optics," *IEEE Journal of Quantum Electronics*, vol. 9, pp. 919-933, 1973.

[79] W. Streifer, D. Scifres, and R. Burnham, "Coupling coefficients for distributed feedback single- and double-heterostructure diode lasers," *IEEE Journal of Quantum Electronics*, vol. 11, pp. 867-873, 1975.

[80] J. E. Carroll, J. Whiteaway, and D. Plumb, *Distributed feedback semiconductor lasers*: IEE, London, UK, 1998.

[81] Y. Xi, "One-dimensional simulation methods for distributed feedback semiconductor lasers," PhD thesis, McMaster University.

[82] M. Yamada and K. Sakuda, "Analysis of almost-periodic distributed feedback slab waveguides via a fundamental matrix approach," *Applied Optics*, vol. 26, pp. 3474-3478, 1987.

[83] S. L. Chuang, *Physics of optoelectronic devices*: Wiley, 1995.

[84] N. Susa, "Feasibility study on the application of the quantum disk to the gain-coupled distributed feedback laser," *IEEE Journal of Quantum Electronics*, vol. 34, pp. 1317-1324, 1998.

[85] S. Ghosh, S. Pradhan, and P. Bhattacharya, "Dynamic characteristics of high-speed InGaAs/GaAs self-organized quantum dot lasers at room temperature," *Applied Physics Letters*, vol. 81, pp. 3055, 2002.

[86] J. Muszalski, J. Houlihan, G. Huyet, and B. Corbett, "Measurement of linewidth enhancement factor in self-assembled quantum dot semiconductor lasers emitting at 1310 nm," *Electronics Letters*, vol. 40, pp. 428, 2004.

[87] S. Melnik, G. Huyet, and A. Uskov, "The linewidth enhancement factor α of quantum dot semiconductor lasers," *Optics Express*, vol. 14, pp. 2950-2955, 2006.

[88] J. C. Hulteen and D. R. Van, "Nanosphere lithography: A materials general fabrication process for periodic particle array surfaces," *Journal of Vacuum Science & Technology A: Vacuum, Surfaces, and Films*, vol. 13, pp. 1553-1558, 1995.

[89] Y. Xia and N. J. Halas, "Shape-controlled synthesis and surface plasmonic properties of metallic nanostructures," *MRS Bulletin*, vol. 30, pp. 338-348, 2005.

[90] C. W. Kuo, J. Y. Shiu, Y. H. Cho, and P. Chen, "Fabrication of large area periodic nanopillar arrays for nanoimprint lithography using polymer colloid masks," *Advanced Materials*, vol. 15, pp. 1065-1068, 2003.

[91] D. S. dos Santos, R. A. Alvarez-Puebla, O. N. Oliveira, and R. F. Aroca, "Controlling the size and shape of gold nanoparticles in fulvic acid colloidal solutions and their optical characterization using SERS," *Journal of Materials Chemistry*, vol. 15, pp. 3045-3049, 2005.

[92] S. A. Maier, P. G. Kik, H. A. Atwater, S. Meltzer, E. Harel, B. E. Koel, and A. A. Requicha, "Local detection of electromagnetic energy transport below the diffraction limit in metal nanoparticle plasmon waveguides," *Nature materials*, vol. 2, pp. 229-232, 2003.

[93] J. Wang, D. Xu, A. N. Kawde, and R. Polsky, "Metal nanoparticle-based electrochemical stripping potentiometric detection of DNA hybridization," *Analytical chemistry*, vol. 73, pp. 5576-5581, 2001.

[94] Y. Kim, R. C. Johnson, and J. T. Hupp, "Gold nanoparticle-based sensing of 'spectroscopically silent' heavy metal ions," *Nano Letters*, vol. 1, pp. 165-167, 2001.

[95] J. Yguerabide and E. E. Yguerabide, "Resonance light scattering particles as ultrasensitive labels for detection of analytes in a wide range of applications," *Journal of Cellular Biochemistry*, vol. 84, pp. 71-81, 2001.

[96] J. Nelayah, M. Kociak, O. Stephan, A. F. de, M. Tence, L. Henrard, D. Taverna, I. Pastoriza-Santos, L. M. Liz-Marzan, and C. Colliex, "Mapping surface plasmons on a single metallic nanoparticle," *Nature Physics*, vol. 3, pp. 348-353, 2007.

[97] G. H. Chan, J. Zhao, G. C. Schatz, and R. P. Duyne, "Localized surface plasmon resonance spectroscopy of triangular aluminum nanoparticles," *The Journal of Physical Chemistry C*, vol. 112, pp. 13958-13963, 2008.

[98] S. Vajda, G. P. Wiederrecht, A. Bouhelier, G. Y. Tikhonov, N. Tomczyk, B. Lee, S. Seifert, and R. E. Winans, "Optical properties of gold nanoparticles produced by the assembly of size-selected clusters: Covering the full visible wavelength range in the smallest particle size regime," *Collection of Czechoslovak Chemical Communications*, vol. 72, pp. 121-128, 2007.

[99] K. L. Kelly, A. A. Lazarides, and G. C. Schatz, "Computational electromagnetics of metal nanoparticles and their aggregates," *Computing in Science and Engineering*, vol. 3, pp. 67-73, 2001.

[100] P. Stoller, V. Jacobsen, and V. Sandoghdar, "Measurement of the complex dielectric constant of a single gold nanoparticle," *Optics Letters*, vol. 31, pp. 2474-2476, 2006.

[101] L. B. Scaffardi and J. O. Tocho, "Size dependence of refractive index of gold nanoparticles," *Nanotechnology*, vol. 17, pp. 1309-1315, 2006.

[102] H. H. van, "Light Scattering by Small Particles," *Light Scattering by Small Particles, New York: John Wiley & Sons, 1957*, 1957.

[103] C. F. Bohren and D. R. Huffman, *Absorption and scattering of light by small particles*: Wiley New York, 1983.

[104] P. W. Barber and S. C. Hill, *Light Scattering by Particles: Computational Methods*: World Scientific, 1990.

[105] M. I. Mishchenko, L. D. Travis, and A. A. Lacis, *Scattering, absorption, and emission of light by small particles*. Cambridge, UK: Cambridge University Press, 2002.

[106] M. I. Mishchenko, L. D. Travis, and J. W. Hovenier, *Light Scattering by Nonspherical Particles: Theory, Measurements, and Applications*: Academic Press, 2000.

[107] E. Cottancin, G. Celep, J. Lerme, M. Pellarin, J. R. Huntzinger, J. L. Vialle, and M. Broyer, "Optical properties of noble metal clusters as a function of the size: Comparison between experiments and a semi-quantal theory," *Theoretical Chemistry Accounts*, vol. 116, pp. 514-523, 2006.

[108] U. Kreibig and M. Vollmer, *Optical properties of metal clusters*. Berlin, Heidelberg, New York: Springer, 1995.

[109] O. Muskens, D. Christofilos, F. N. Del, and F. Vallee, "Optical response of a single noble metal nanoparticle," *Journal of Optics A-Pure and Applied Optics*, vol. 8, pp. S264-S272, 2006.

[110] O. L. Muskens, F. N. Del, F. Vallee, J. R. Huntzinger, P. Billaud, and M. Broyer, "Single metal nanoparticle absorption spectroscopy and optical characterization," *Applied Physics Letters*, vol. 88, pp. -, 2006.

[111] S. Berciaud, L. Cognet, P. Tamarat, and B. Lounis, "Observation of intrinsic size effects in the optical response of individual gold nanoparticles," *Nano Letters*, vol. 5, pp. 515-518, 2005.

[112] A. Arbouet, D. Christofilos, F. N. Del, F. Vallee, J. R. Huntzinger, L. Arnaud, P. Billaud, and M. Broyer, "Direct measurement of the single-metal-cluster optical absorption," *Physical Review Letters*, vol. 93, 2004.

[113] J. Wang, W. M. Lau, and Q. Li, "Effects of particle size and spacing on the optical properties of gold nanocrystals in alumina," *Journal of Applied Physics*, vol. 97, 2005.

[114] G. Celep, E. Cottancin, J. Lerme, M. Pellarin, L. Arnaud, J. R. Huntzinger, J. L. Vialle, M. Broyer, B. Palpant, O. Boisron, and P. Melinon, "Optical properties of copper clusters embedded in alumina: An experimental and theoretical study of size dependence," *Physical Review B*, vol. 70, 2004.

[115] M. Gaudry, E. Cottancin, M. Pellarin, J. Lerme, L. Arnaud, J. R. Huntzinger, J. L. Vialle, M. Broyer, J. L. Rousset, M. Treilleux, and P. Melinon, "Size and composition dependence in the optical properties of mixed (transition metal/noble metal) embedded clusters," *Physical Review B*, vol. 67, 2003.

[116] B. Palpant, B. Prevel, J. Lerme, E. Cottancin, M. Pellarin, M. Treilleux, A. Perez, J. L. Vialle, and M. Broyer, "Optical properties of gold clusters in the size range 2-4 nm," *Physical Review B*, vol. 57, pp. 1963-1970, 1998.

[117] J. Lerme, B. Palpant, B. Prevel, M. Pellarin, M. Treilleux, J. L. Vialle, A. Perez, and M. Broyer, "Quenching of the size effects in free and matrix-embedded silver clusters," *Physical Review Letters*, vol. 80, pp. 5105-5108, 1998.

[118] J. Lerme, "Introduction of quantum finite-size effects in the Mie's theory for a multilayered metal sphere in the dipolar approximation: Application to free and matrix-embedded noble metal clusters," *European Physical Journal D*, vol. 10, pp. 265-277, 2000.

[119] E. Cottancin, J. Lerme, M. Gaudry, M. Pellarin, J. L. Vialle, M. Broyer, B. Prevel, M. Treilleux, and P. Melinon, "Size effects in the optical properties of Au_nAg_n embedded clusters," *Physical Review B*, vol. 62, pp. 5179-5185, 2000.

[120] B. Prevel, B. Palpant, J. Lerme, M. Pellarin, M. Treilleux, L. Saviot, E. Duval, A. Perez, and M. Broyer, "Comparative analysis of optical properties of gold and silver clusters embedded in an alumina matrix," *Nanostructured Materials*, vol. 12, pp. 307-310, 1999.

[121] J. Lerme, B. Palpant, E. Cottancin, M. Pellarin, B. Prevel, J. L. Vialle, and M. Broyer, "Quantum extension of Mie's theory in the dipolar approximation," *Physical Review B*, vol. 60, pp. 16151-16156, 1999.

[122] J. Lerme, B. Palpant, B. Prevel, E. Cottancin, M. Pellarin, M. Treilleux, J. L. Vialle, A. Perez, and M. Broyer, "Optical properties of gold metal clusters: A time-dependent local-density-approximation investigation," *European Physical Journal D*, vol. 4, pp. 95-108, 1998.

[123] C. Salzemann, J. Lerme, J. Urban, and I. Lisiecki, "Is it possible to correlate a collection of copper nanocrystals with their optical response?" *Chemistry of Materials*, vol. 17, pp. 1279, 2005.

[124] J. Lerme, G. Celep, M. Broyer, E. Cottancin, M. Pellarin, A. Arbouet, D. Christofilos, C. Guillon, P. Langot, F. N. Del, and F. Vallee, "Effects of confinement on the electron and lattice dynamics in metal nanoparticles," *European Physical Journal D*, vol. 34, pp. 199-204, 2005.

[125] S. L. Chuang, *Physics of photonic devices*: Wiley, 2009.

[126] Y. P. Chiou, Y. C. Chiang, and H. C. Chang, "Improved three-point formulas considering the interface conditions in the finite-difference analysis of step-index optical devices," *Journal of Lightwave Technology*, vol. 18, pp. 243-251, 2000.

[127] J. P. Berenger, "A perfectly matched layer for the absorption of electromagnetic waves," *Journal of Computational Physics*, vol. 114, pp. 185-200, 1994.

[128] P. Y. Amnon Yariv, *Photonics: optical electronics in modern communications*: Oxford University Press, 1997.

[129] L. V. Nguyen, "Mode-partition noise in semiconductor lasers," Electronic Warfare and Radar Division Systems Sciences Laboratory, Australia, 2002.

[130] S. Ogita, A. J. Lowery, and R. S. Tucker, "Influence of asymmetric nonlinear gain on the transient intensities of longitudinal modes in long wavelength Fabry-Perot laser diodes," *IEEE Journal of Quantum Electronics*, vol. 33, pp. 198-210, 1997.

[131] D. Marcuse, "Computer simulation of laser photon fluctuations: Theory of single-cavity laser," *IEEE Journal of Quantum Electronics*, vol. 20, pp. 1139-1148, 1984.

[132] D. Marcuse, "Computer simulation of laser photon fluctuations: single-cavity laser results," *IEEE Journal of Quantum Electronics*, vol. 20, pp. 1148-1155, 1984.

[133] D. Marcuse, "Computer simulation of laser photon fluctuations: coupled-cavity lasers," *IEEE Journal of Quantum Electronics*, vol. 21, pp. 154-161, 1985.

[134] D. Marcuse, "Computer simulation of laser photon fluctuations: DFB lasers," *IEEE Journal of Quantum Electronics*, vol. 21, pp. 161- 167, 1985.

[135] A. Taflove and S. C. Hagness, *Computational electrodynamics*: Artech house Boston, 1995.

[136] H. Derudder, F. Olyslager, Z. D. De, and B. S. Van, "Efficient mode-matching analysis of discontinuities in finite planar substrates using perfectly matched layers," *IEEE Transactions on Antennas and Propagation*, vol. 49, pp. 185-195, 2001.

[137] J. Mu and W. Huang, "Simulation of three-dimensional waveguide discontinuities by a full-vector mode-matching method based on finite-difference schemes," *Optics Express*, vol. 16, pp. 18152-18163, 2008.

[138] J. Mu, H. Zhang, and W. Huang, "Investigation of long-range surface plasmon polaritons gratings by complex mode matching method," *Proceedings of SPIE*, pp. 664213.1-664213.8, 2007.